Turbulent dissipation from AMAZOMIX off the Amazon shelf along internal tides paths

Fabius Kouogang[1,4], Ariane Koch-Larrouy[1], Jorge Magalhaes[2], Alex Costa da Silva[4], Daphne Kerhervé[1], Arnaud Bertrand[5], Evan Cervelli[3], Fernand Assene1, Jean-François Ternon[5], Pierre Rousselot[6], James Lee[7], Marcelo Rollnic[7], Moacyr Araujo[4]

[1]LEGOS, Université de Toulouse, CNRS, OMP, IRD, Toulouse, France

[2]Department of Geoscience, Environment and Spatial Planning (DGAOT), Faculty of Sciences, University of Porto, Porto, Portugal

[3]Rockland Scientific Inc, Lunenburg, Nova Escócia, Canadá

[4]Departamento de Oceanografia, Universidade Federal de Pernambuco, DOCEAN/UFPE, Recife, Brazil

[5]MARBEC, Université de Montpellier, CNRS, Ifremer, IRD, Sète, France

[6]IMAGO, Université de Bretagne Occidentale, CNRS, Ifremer, IRD, Brest, France

[7]Departamento de Oceanografia, Universidade Federal do Pará, UFPA, Belém, Brazil

Correspondence to: Fabius Kouogang (fabius.cedric@yahoo.fr)

Abstract.

The Amazon shelf break is a key oceanic region where strong internal tides (ITs) are generated, playing a significant role in climate processes and ecosystems through vertical mixing. During the AMAZOMIX survey (2021), currents, hydrography, and turbulence were measured over M2 tidal period (12.42 h) at numerous sites near the Amazon outflow, where ITs are also generated along the slope. This dataset offers an opportunity to explore the influence of ITs on vertical mixing off the Amazon shelf, as well as to quantify the extent and locations of this impact.

Microstructure analyses, integrated with hydrographic data, highlighted contrasting dissipation rates. The highest dissipation rates occurred at IT generation sites and along IT pathways, while the lowest values were observed in non-tidal areas. Near generation sites, mixing rates were elevated, between [10^{-6}, 10^{-5}] W kg^{-1}, with IT shear contributing ~65 %, compared to mean baroclinic current (BC) shear. Along IT pathways and in far-field IT regions, mixing decreased to [10^{-8}, 10^{-7}] W kg^{-1} but remained substantial, driven by nearly equal contributions from IT and BC shear.

A key finding was the relative increase in mixing ([10^{-7}, 10^{-6}] W kg^{-1}) ~ 230 km from two distinct IT generation sites at the shelf break. This region of increased mixing coincided with the constructive interference of IT rays from different generation sites. It also aligned with the presence of large-amplitude internal solitary waves (ISWs) observed in satellite imagery, suggesting that constructive IT ray interference may generate non-linear ISWs, leading to intensified mixing.

These findings provide valuable insights for developing parameterizations of tidal and mean shear mixing for ocean or coupled models, with significant implications for regional biogeochemistry and the climate system.~~The Amazon shelf-break is a key region of the ocean where strong internal tides (ITs) are generated, which may have a key role to play on both Climate and Ecosystem, via its vertical mixing. AMAZOMIX survey (2021) collected microstructure and hydrographic (ADCP/CTD-O_2) profiles to quantify mixing, associated processes and their impact on marine ecosystems. Measurements are obtained over M2 tidal period (12h) inside and outside of both the ITs generation sites and propagation beams, respectively at mode-1 distances (90km and 210km) from the shelf-break to evaluate the IT impact on mixing.~~

~~Hydrography analysis showed strong step-like characteristics (~20-40 m thick) and vertical displacements (20-60 m) triggered by ITs, as well as the signatures of high modes up to 5-6 on generation sites and IT pathways.~~

~~The results of the microstructure analysis coupled with those of the hydrography revealed important mixing associated with a competition of processes between the semidiurnal shear of ITs and the baroclinic shear of the mean current (BC). Closer to the generation sites, mixing is stronger within $[10^{-6},10^{-4}]$ W.kg^{-1}, with a greater contribution (~65 %) from ITs shear than BC shear. It is reduced but nevertheless considerable between $[10^{-8}, 10^{-6}]$ W.kg^{-1} along the IT pathways, owing to equal contributions from ITs and BC shear. At a distance of ~225 km, mixing was still higher within $[10^{-7},10^{-6}]$ W.kg^{-1} because of the increased contribution (~65 %) of ITs shear, where IT beams may intersect and interact with background circulation. Mixing in no-tidal fields was fairly minimal ($[10^{-8},10^{-7}]$ W.kg^{-1}), owing to a minor contribution (~50.4 %) of BC shear from the North Brazil Current.~~

~~Finally, the nutrient flux estimations showed that ITs mixing could reach the surface (by a large tidal diffusivity of $[10^{-4},10^{-1}]$ m^{-2}.s^{-1}). This resulted in high vertical fluxes of nitrate ($[10^{-2}, 10^{-0}]$ mmol N m^{-2}.s^{-1}) and phosphate ($[10^{-3}, 10^{-1}]$ mmol P m^{-2}.s^{-1}), which can stimulate chlorophyll production, biodiversity and cool surface water, so influencing the whole ecosystem and climate in this river-ocean continuum region. This study provides a guide for the mixing parameterization in future numerical simulation (e.g., in physical-biogeochemical coupled models) in the Amazon region in order to include the impact of the IT turbulence on the whole ecosystem (i.e., from physics to biological production).~~

1 Introduction

Turbulent mixing in the ocean plays an important role in sustaining the thermohaline and meridional overturning circulation and in closing the global ocean energy budget (Kunze, 2017). These processes have strong implications for the climate, influencing~~through the influence on~~ heat and carbon transport, as well as~~and~~ nutrients supply for photosynthesis (Huthnance, 1995; Munk and Wunsch, 1998). Mixing processes can result from wind in the surface waters layer~~surface layer of the ocean~~, internal waves and shear instability in the ocean interior, and bottom friction near ~~close to~~ the bottom layer (Miles, 1961; Thorpe, 2018; Ivey et al., 2020; Inall et al., 2021). Barotropic tides interacting with steep shelf-break topography trigger internal waves at tidal frequencies~~y~~ and harmonics, known as~~called~~ internal tides (ITs), which can~~ that may~~ propagate and produce~~generate~~ mixing. These ITs can be expressed by~~induce~~ large vertical displacements (up to tens of meters) of water masses~~ up to tens of meters~~(Garrett and Kunze, 2007). After their generation on the~~at~~ shelf-break, the (more unstable) higher modes of ITs may~~ITs higher-modes (more unstable) can~~ dissipate locally, while the lower modes can propagate far away (Zhao et al., 2016)~~whereas ITs lower-modes may propagate far from generation sites~~. IT beams (generated where the slope of the ITs and the topography match together on the shelf-break) can propagate vertically, resulting in reflection, scattering and dissipation of ITs at the bottom, surface waters, or thermocline levels (New and Da Silva, 2002; Gerkema and Zimmerman, 2008; Bordois, 2015; Zhao et al. 2016)~~They can dissipate where the energy beam reflects at the bottom, at the surface or at the thermocline levels (Bordois, 2015; Zhao et al. 2016) or where energy flux interferes with each other (Zhao et al. 2012)~~. They~~ITs~~ can also dissipate when energy fluxes interfere (Zhao et al., 2012) or interact with strong baroclinic eddies or currents (Rainville and Pinkel, 2006; Whalen et al., 2012)~~they interact with strong baroclinic eddies or currents (Rainville and Pinkel, 2006; Whalen et al., 2012)~~. Furthermore, ITs may disintegrate into~~in~~ packets of higher-mode nonlinear internal solitary waves (ISWs), which~~ that~~ can propagate and dissipate offshore (Jackson et al., 2012).

Previous and recent studies have shown that ITs-induced turbulent mixing can affect the surface, such as sea surface temperature (Ray and Susanto, 2016; Nugroho et al., 2018; Assene et al., 2024), chlorophyll content (Muacho et al., 2014; M'Hamdi et al., 2024; in preparation), marine ecosystems (Wang et al., 2007; Zaron et al., 2023), ~~can have impacts on the surface, such as on sea surface temperature (Ray and Susanto, 2016; Nugroho et al. 2018; Assene et al., 2024), chlorophyll content (M'Hamdi et al., 2024; in preparation) and marine ecosystems (Wang et al. 2007; Muacho et al., 2014; Zaron et al. 2023),~~ and~~as well as on the~~ atmospheric convection and the rainfall structure (Koch-Larrouy et al., 2010, Sprintall et al. 2014).

In the western tropical Atlantic, the Amazon River-Ocean Continuum (AROC) constitutes a key region of the global oceanic and climate system (Araujo et al., 2017; Varona et al., 2018). This region (Fig. 1a) is characterized~~characterised~~ by a system~~the presence of a system~~ of western boundary currents, including North Brazil Current (NBC). NBC, which flows~~flowing~~ northwestward, has its core velocities (~~=~~$\sim$ 1.2 m ~~.~~s^{-1}) that remain stable~~stable~~ from the surface to a depth of 100 m (Johns et al., 1998; Bourlès et al., 1999; Barnier et al., 2001; Neto and Silva, 2014). ~~Additionally,There is also a system of Amazonian Lenses of water (AWL), influencedinduced by continental inputs, can affect which can influence both the boundary layer and mixed layer patterns (Silva et al., 2005; Prestes et al., 2018).~~ This region also experiences highly variable dynamics due to the Amazon River Plume. During the rainy season (May-July), peak discharge can extend the plume over 1500 km offshore, northwest along the NBC. In the dry season (September-November), reduced discharge and stronger saline intrusion may confine the plume to less than 500 km offshore, near the Amazon Shelf, with some eastward dispersion (Coles et al., 2013).

The Amazon plume can generate vertical shear in underlying currents, enhancing mixing. Additionally, a system of Amazonian Lenses of water (AWL), influenced by continental inputs, may affect both the boundary layer and mixed layer patterns (Silva et al., 2005; Prestes et al., 2018).

In the AROC region, the Amazon shelf-break is a hotspot for the generation, propagation and dissipation of ITs and ISWs as a result of non-linear processes (Geyer, 1995; Brandt et al., 2002; Magalhães et al., 2016; Ruault et al., 2020; Tchilibou et al., 2022; Fig 1). Previous studies using Synthetic Aperture Radar (SAR) satellite images~~Using SAR images, previous studies~~ (Magalhaes et al., 2016) identified ISWs along the path of ITs propagating from two sites (i.e., sites Aa and Ab; Fig. 1a). Conversely, other sites showed no~~did not have any~~ ISWs propagation (i.e., sites E~~F~~ and D; Fig. 1a, 1b and 1c) (see Magalhaes et al., 2016 for definition). Using numerical modeling, Tchilibou et al. (2022) showed that about 30 % of the M2 (dominant tidal component;~~,~~ Le Bars et al. 2010) ITs energy is dissipated locally (for higher-modes ITs) at sites E~~F~~, Aa, Ab and D (Fig. 1a), while the remaining~~and that the remaining~~ lower-modes ITs energy can be dissipated remotely. Dissipation away from the generation sites (E~~F~~, Aa, Ab and D; Fig. 1a) can result from the shear instabilities caused by ~~that are due to processes of~~ ITs-ITs and/or ITseddy/current interactions. Despite the presence of ITs, no direct measurements of dissipation rates have been conducted to our knowledge. ~~Moreover,In addition, the impacts of IT dissipation on vertical nutrient fluxes in the AROC region are still unexplored.~~

The mixing induced by these internal waves in the region was observed during the AMAZOMIX cruise (Bertrand et al., 2021). The cruise was~~It has been~~ designed with~~to have~~ stations/transects inside and outside ITs fields (Fig. 1a and 1c) ~~and~~ to measure ITs dissipation and study their impact on the AROC ecosystem. Direct microstructure measurements of temperature, salinity and velocity were conducted at the different repeated stations/transects over a~~one~~ M2 tidal cycle (~ 12.42 h). These cruise measurements offer an opportunity to explore whether ITs play a role in mixing within the AROC region. In this study, we will quantify mixing and~~,~~ identify the associated processes~~, and investigate their impact on nutrient fluxes~~ off the Amazon shelf. We will calculate turbulent kinetic energy (TKE) dissipation rates, vertical displacements of isopycnal surfaces ~~and~~ and vertical eddy diffusivities using in situ microstructure and hydrography data. Finally, t~~T~~he baroclinic shear of currents and their contributions to mixing will ~~then~~ be calculated from current data collected between stations and transects. ~~Finally, we will use vertical diffusivities estimations to determine vertical nutrient fluxes at the base of the mixed layer.~~

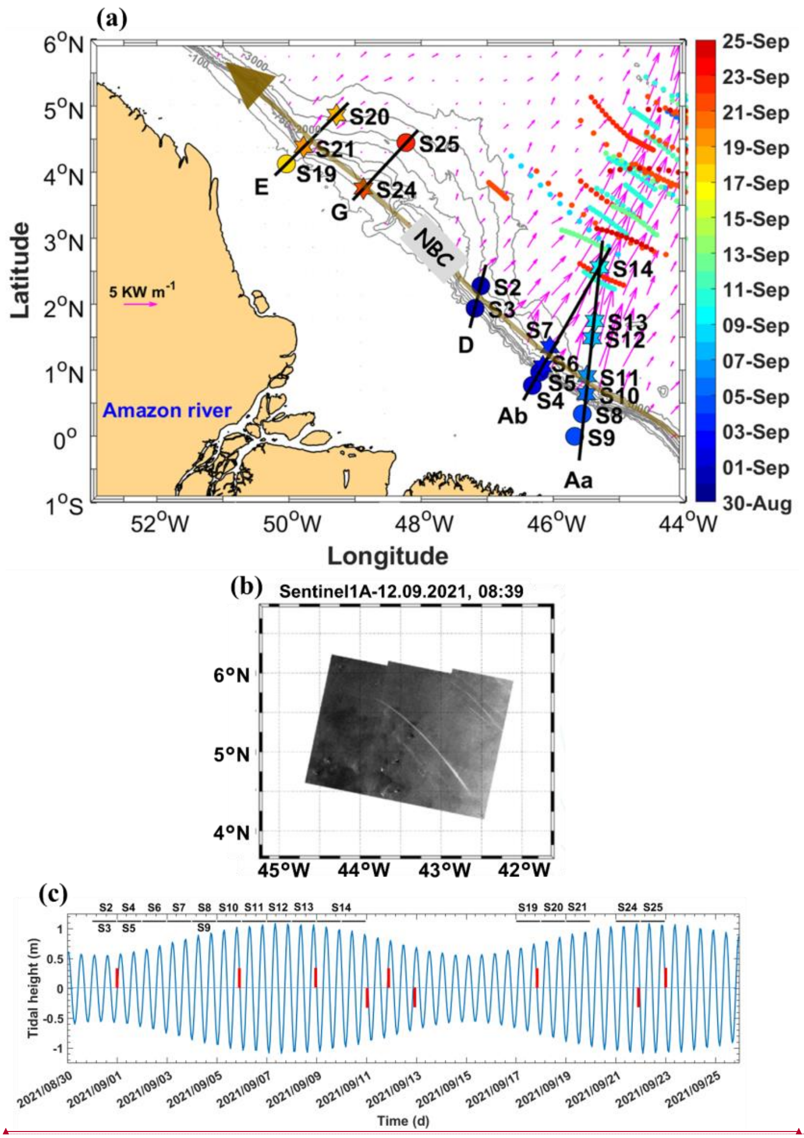

Formatted: Font: 11 pt

Formatted: Left, Indent: Left: 0 cm, Line spacing: Multiple 1,15 li

Formatted: Font: 11 pt

Figure 1: a) Map of a part of the AMAZOMIX 2021 cruise off the Amazon shelf, showing bathymetric contours (100 m, 750 m, 2000 m, and 3000 m isobaths) in gray. Colored circles and stars indicate short and long CTD-O2/L-S-ADCP stations, respectively, with the corresponding sampling dates represented by the color bar. Solid black lines depict SADCP transects (for Aa, Ab, D, G, and E). Magenta arrows show the 25-hour mean depth-integrated baroclinic IT energy flux (September 2015, from the NEMO model) originating from IT generation sites (Aa, Ab, D, and E) along the shelf break. The solid brown line represents the NBC pathways illustrating background circulation. Shattered colored lines highlight ISW signatures. b) 1A Sentinel image acquired on 12th September 2021, showing ISW signatures. c) Tidal range at AMAZOMIX stations, with ISW signature dates marked by red bars.

Formatted: Font: 11 pt, Italic

Formatted: Font: 11 pt, Italic

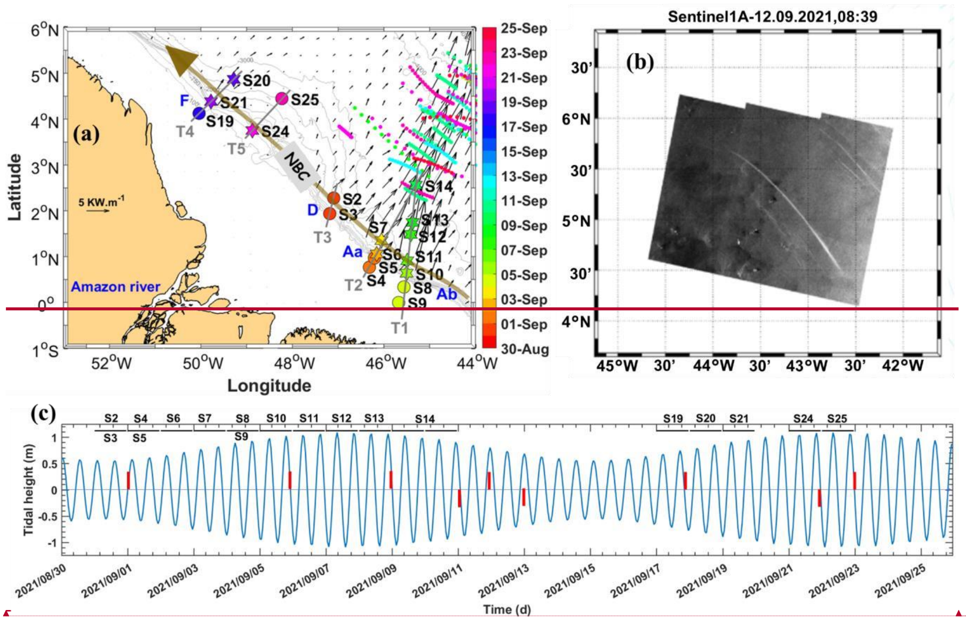

~~Figure 1: a) Map of part of the AMAZOMIX 2021 cruise with bathymetric grey lines (100 m, 750 m, 2000 m, and, 3000 m and 4000 m isobaths) off the Amazon shelf. Colored circles and stars represent short and long CTD-O$_2$/L-S-ADCP stations casts, respectively. Colored bar represents the time. Solid blackgrey lines represent SADCP transects (Aa, Ab, D, G, and ET1 to T5). MagentaBlack arrows represent 25h-mean depth-integrated baroclinic ITs energy flux (on September 2015 from NEMO model) from ITs generation sites (Aa, Ab, D and F) on along the critical slope (grey contours) of the shelf break. Solid brown line indicates the background circulation with NBC pathways. Shattered colored lines show ISW signatures. T1 to T4 and T5 represent the inside-ITs and outside-ITs transects, respectively. b) 1A Sentinel image acquired 12th September 2021 showing ISW signatures. c) Tidal range at AMAZOMIX stations with ISW signatures dates indicated in red bars.~~

Formatted: Font: 11 pt

Formatted: Font: 11 pt

2 Data and Methods

2.1 Data collection

The AMAZOMIX cruise (Bertrand et al., 2021) was performed over~~on~~ the shelf/slope areas off the AROC during August-October 2021~~, on~~ aboard~~board~~ the IRD vessel RV *ANTEA*. At each designated site, 12-hour stations were set up,~~12h-long stations were conducted~~ with repeated casts (4-5 casts per site)~~(between 4 and 5 for each site) casts~~ of Conductivity-Temperature-Depth-Oxygen (CTD-O_2)/Lowered Acoustic Doppler Current Profiler (LADCP) and Velocity Microstructure Profiler (VMP) ~~in previously defined sites~~ to measure the TKE dissipation rates over a~~one~~ complete tidal (M2) cycle, ~~and~~ allowing the separation of the tidal component from the total current~~extract the tidal (M2) contribution from the total current~~. A high-resolution (1/36°) NEMO~~v3.6~~ (Nucleus for European Modeling of the Ocean) model (Madec et al., 2019) was used to determine station locations based on realistic IT generation and propagation maps (Tchilibou et al., 2022; Assene et al., 2024) and to ~~NEMOv3.6 model (1/36°) (Nucleus for European Modeling of the Ocean; Madec et al., 2019) that provides realistic maps of ITs generation and propagation (Fig. 1a; Tchilibou et al., 2022; Assene et al., 2024) was used to estimate the position of 12h stations and~~ estimate the mean background stratification~~ at these stations~~.

Stations (Fig. 1a and 1c) were located inside the ITs fields, named “IN-ITs” (sites Aa, Ab and D: S2 to S14; site E~~F~~: S19 to S21), and outside the ITs fields (S24 and S25), named “OUT-ITs”, on the shelf-break generation (sites Aa, Ab, D and F) and propagation along 5 transects (Aa, Ab, D, G, and E ~~T1 to T5,~~; Fig. 1)~~ including stations~~.

CTD-O_2 measurements were obtained using a Seabird 911 Plus with dual sensors mounted in the rosette~~ equipped with 11 Niskin bottles used to sample water down to 1000 m depthto a depth of 1000 m. Concentrations of nutrients (nitrate and phosphate), including nitrate and phosphate, were determined from nutrient samples taken in 30 ml Nalgene bottles and stabilizedstabilised in an oven at 80 °C for 2h30~~. The 24 Hz CTD-O_2 sensors were calibrated before and after the cruise. The standard deviation of temperature (salinity; oxygen) was 0.003 °C (0.003 PSU; 0.05 ml ~~.~~l^{-1}) according to adjusted data. CTD-O_2 data were averaged over 1-m bins to filter out spikes and missing points, and aligned in time to correct the lag effects.

Two 300 kHz RDI LADCPs~~LADCPs RDI 300 kHz~~ were mounted on the rosette to provide vertical current profiles with 8 m resolution, supplemented by 75 kHz shipboard ADCP (SADCP) profiles recorded continuously during the cruise~~, one looking down and other one looking up, to provide vertical currents profiles with a 8 m resolution.~~. Vertical resolution of SADCP was adjusted according to bottom depth, e.g., 8 m for depths >150 m (at S6, S7, S10-S14, S20, S21, and S24) and 4 m for other depths. ~~In addition, 75 kHz ship-ADCP (SADCP) profiles (with vertical resolution adjusted to the bottom depth: 8 m at S6, S7, S10-S14, S20, S21 and S24, for bottom depth > 150 m; and 4 m at the rest) were continuously recorded during the cruise~~. Data processing and quality control followed GO-SHIP Repeat Hydrography Manual protocols~~All measured data were processed and quality controlled according to the standard protocols of the GO-SHIP Repeat Hydrography Manual~~. In total, 71 CTD-O2/LADCP profiles were collected during the AMAZOMIX cruise.~~A total number of 71 CTD-O$_2$/LADCP profiles were acquired during the AMAZOMIX cruise.~~

To characterize mixing, the TKE microstructure profiles were obtained from high-frequency (~ 2 mm resolution)~~high frequency (resolution: ~2 mm)~~ measurements of temperature and velocity shear using a VMP-250 profiler (Rockland Scientific International, Inc.) capable of reaching depths up to 1000 m~~operating at depth range of 1000 m~~. The VMP-250 features~~The instrument has~~ two high-resolution thermistors (FP07) and two high-resolution velocity shear probes (probe 1 and 2;~~,~~ with 5% signal accuracy~~with accuracy of 5 % of the total signal~~), with a sampling rate~~their sampling frequency~~ of 1024 Hz. The ~~VMP-250~~ profiler was deployed and retrieved via~~and recovered with use of~~ an electric winch and rope tether, with alternating deployments~~. The VMP was alternatively deployed~~ between the CTD-O$_2$/LADCP profiles at 33 stations,~~ for~~ yielding a total of 202 profiles. For this study, data from 18 stations (S2-S14, S19-S21, S24, and S25) comprising SADCP data, 109 VMP profiles and 54 CTD-O2/LADCP profiles will be analyzed~~Only 18 stations (S2 to S14, S19 to S21, S24 and S25) for a total of 109 VMP profiles and 54 CTD-O$_2$/LADCP profiles will be processed and used in this study~~.

2.2 Methods

TKE dissipation rates

The VMP data are~~were~~ processed using ODAS Matlab library (developed by Rockland Scientific International, Inc) to infer the~~in order to determine~~ TKE dissipation rate (ε). The processing methods for the VMP data~~VMP processing methods~~ are briefly described here and adhere to~~explained here, and conform to~~ the recommendations of ATOMIX (Analyzing ocean turbulence observations to quantify mixing), as reported by Lueck et al. (2024), and have been validated against~~ group (reported in Lueck et al., 2024) and tested against~~ the benchmark estimates (presented in Fer et al., 2024).

First, the VMP data are converted into physical shear units, and the~~. The~~ time series are prepared.~~,~~ Continuous sections of the time series are selected~~and sections (continuous parts of the time series) within VMP data are chosen~~ for dissipation estimation. Before spectral estimation, the aberrant shear signals caused by vessel wake contamination are removed~~is eliminated from the timeseries~~. Collisions of the shear probe with plankton and other particles are removed~~Shear probe collisions (with plankton and other matter) are removed from the shear signals~~ using the de-spiking routine. The records from each section are then~~is~~ high-pass filtered (e.g., at station S6 and S10; Fig. 2a, and Fig. A1, Appendix).

Shear spectra are estimated using record lengths (L~~diss_length~~) and Fast Fourier Transform segments ~~(fft_length)~~ of 2 s, which~~that~~ are cosine windowed and overlapped ~~(overlap_sec)~~ by 50% (e.g., at station S6 and S10; Fig. 2b, and Fig. A1, Appendix). Additionally, v~~V~~ibration-~~-~~coherent noise is removed. Different L~~diss_length~~ and overlap (O)~~overlap_sec~~ settings were selected and tested based on the environment (e.g., deep vs. shallow water),~~were chosen and tested based on the~~

~~environment (deep and shallow water)~~ following Fer et al. (2024). For shallow stations, L (O)~~After testing, the diss_length (overlap_sec)~~ was shortened to 5~~4~~s (2.5s), in contrast to the~~ for shallow stations rather than~~ 8 s (4 s) used for deeper stations, due to evidence of overturns observed in AMAZOMIX acoustic measurements at deeper stations~~for deep stations, because of the evidence of the presence of overturns from AMAZOMIX acoustic measurements in deep water stations~~ (Koch-Larrouy et al., 2024; in preparation). This adjustment helped to~~and to~~ optimize the spatial resolution of dissipation estimates in shallow water stations.

Finally, ε is determined using the spectral integration method and by comparison with the Nasmyth empirical spectrum (Nasmyth, 1970). Quality assurance tests are carried out in accordance with ATOMIX's recommendations (Lueck et al., 2024). A figure of merit < 1.4 is used to exclude bad data (e.g., at station S6 and S10; Fig. 2b, and Fig. A1, Appendix), and the fraction of data affected by de-spiking is < 0.05.

~~The estimation of ε used high pass filtered data. Fig. 2 illustrate sshows an example of the high- pass filtered shear probes data at station S6 (Fig. 2a). These shearThe shear data are qualitatively supported by both the observed profiles (Fig. 2c) and the low-pass filtered, along-path temperature, gradients along path (Fig. 2b). In regions of high turbulence, the variance in temperature gradients is notably enhanced and exhibits a bipolar structure, while temperature inversions occur due to overturns. In contrast, in regions with low turbulence, temperature gradient variance is inverted, and the background temperature generally decreases with depth.In high turbulence regions, the temperature gradient variance is enhanced (bipolar), and the temperature is reversed as a result of the overturns. In low turbulence regions, the temperature gradient variance is inverted and background temperature tends to decrease with depth. Figure A1, S10~~

Commented [1]:

Commented [2]:

Formatted: Font color: Custom Color(RGB(17;17;17)), Not Highlight

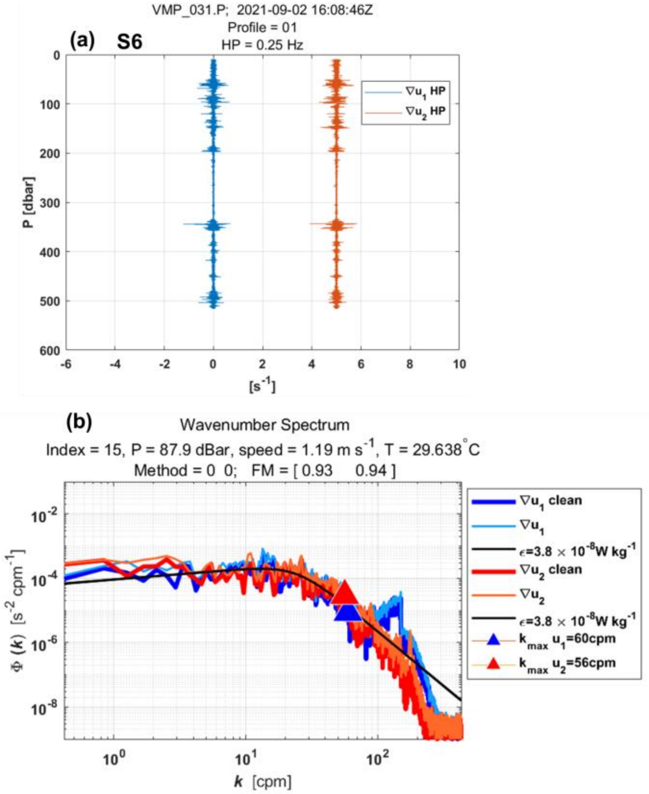

Figure 2: Example of wavenumber spectra from a dissipation structure segment used to determine the dissipation rate at station S6 at a pressure of 87.9 dBar. (a) Cleaned and high-pass filtered signals from shear probe 1 (blue) and shear probe 2 (red, offset by 5 s-1). (b) Wavenumber spectra for shear probes 1 and 2. Thick lines (blue for probe 1, red for probe 2) show shear spectra with coherent noise correction, while thin lines (sky blue for probe 1, orange for probe 2) show spectra without correction. Triangles mark the maximum wavenumber used for dissipation rate estimation. Black lines represent Nasmyth

Formatted: Not Highlight

Formatted: Not Highlight

Formatted: Font: Italic, Not Highlight

Formatted: Space After: 0 pt

Formatted: Font: Italic, Not Superscript/ Subscript *reference spectra for estimated dissipation rate of 3.8 x 10-8 W kg-1 for both shear probes. Dissipation rate estimates for shear probe 1 and shear probe 2 at a pressure of 87.9 dBar yielded a figure of merit of 0.93 and 0.94, respectively.*

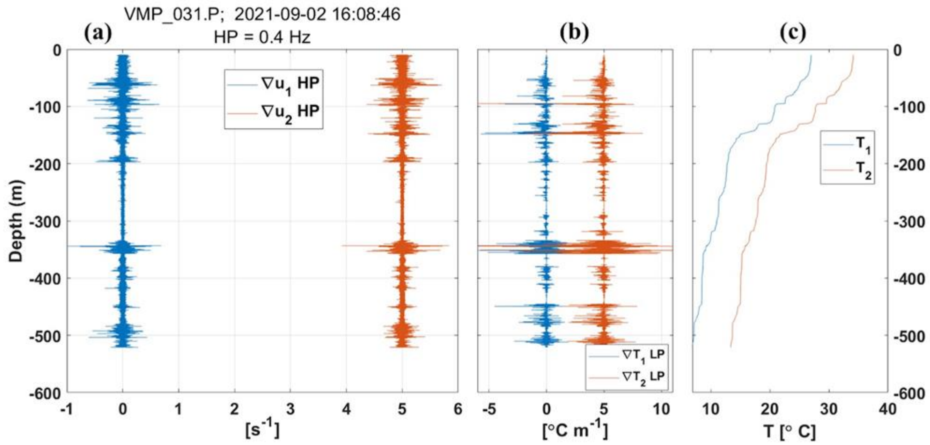

~~Figure 2: Example of the VMP data at station S6. (a) Vertical profiles of data from shear probe 1 (∇u1, blue), and from shear probe 2 (∇u2, red). HP indicates high-pass filtering of the shear probe data. (b) Vertical gradients of temperature from shear probe 1 (∇T1, blue) and probe 2 (∇T2, red). LP indicates low-pass filtering on the along-path gradients. (c) Temperature 145 profiles T1 (blue) and T2 (red) based on nominal calibration coefficients.~~

The vertical eddy diffusivity coefficient

The efficiency of turbulence in redistributing energy is assessed through the calculation of the vertical eddy diffusivity coefficient (Kz). This coefficient is particularly significant in regions such as pycnoclines, where stratification suppresses mixing, making turbulence-driven mixing a key mechanism for vertical energy transport (Thorpe, 2007).

Kz is calculated from ε following the formulation of Osborn (1980), given by Kz= ε Γ N-2. Here, N2 is the buoyancy frequency squared, which is calculated using the sorted potential density profiles (σ_θ) obtained from CTD-O2 data. It is given by N2 = -(g/ρ0) (dσ_θ/dz), where ρ0 is a reference density (1025 kg m-3) and g is the gravitational acceleration. Γ is the mixing efficiency, defined as the ratio between the buoyancy flux and the energy dissipation, and is typically set to 0.2, which corresponds to the critical Richardson number Ri = 0.17 (Osborn, 1980). ε is linearly interpolated into the depths of N2.

Formatted ...
Formatted ...
Formatted ...
Formatted ...
Formatted ...
Formatted ...
Formatted ...
Formatted ...
Formatted ...
Formatted ...
Formatted ...
Formatted ...
Formatted ...
Formatted ...
Formatted ...
Formatted ...
Formatted ...
Formatted ...
Formatted ...
Formatted ...
Formatted ...
Formatted ...
Commented [3]:
Formatted ...
Formatted ...
Formatted ...
Formatted ...
Formatted ...
Formatted ...
Formatted ...
Formatted ...
Formatted ...
Formatted ...
Formatted ...

Turbulence within the pycnocline can reduce stratification and increase vertical eddy diffusivity below the mixing layer (Thorpe, 2007). Subsurface mixing, driven by the breaking of ITs and shear instabilities, plays a particularly important role below the mixed layer, especially in equatorial waters (Gregg et al., 2003).

There are several criteria for defining the Mixed Layer Depth (MLD). In this study, we use the commonly accepted density threshold criterion of 0.03 kg m-³, as defined by de Boyer Montégut et al. (2004) and Sutherland et al. (2014), to estimate the MLD for each CTD-O₂ profile. Notably, comparisons with density thresholds of 0.01 and 0.02 kg m-3 revealed no major differences in MLD across the AMAZOMIX stations and transects (Fig. A2, Appendix).

The miXing Layer Depth (XLD) is defined as the depth at which ε decreases to a background level (Sutherland et al., 2014). Previous studies have applied various thresholds for background dissipation levels, such as such as 10-8 and 10-9 W kg-1 in higher latitudes based on in situ observations (Sutherland et al., 2014; Lozovatsky et al., 2006; Cisewski et al., 2008; Brainerd and Gregg, 1995) and 10-5 m2 s-1 using an ocean general circulation model (Noh and Lee, 2008). In this study, XLD is specified as the depth where ε drops from its first minimum value. This aligns with previous dissipation thresholds and ensures that mixing is captured independently of surface influences. The Upper (UTD) and Lower (LTD/LPD) Thermocline/Pycnocline Depth are delimited as defined by Assunçao et al (2020). UTD corresponded to the depth where the vertical temperature gradient $\partial\theta/\partial z$ = 0.1 °C m-1, while LTD/LPD were the last depth below the UTD at which N2 ≥ 10-4 s-2.

~~For each of the CTD-O2 profiles, the Mixed Layer Depth (MLD) was computed using a density criterion of 0.03 kg.m-3 difference (Montégut et al., 2004) with the surface density (with no major difference from density criterion of 0.01 and 0.02 kg.m-3 by way of comparison) at AMAZOMIX stations/transects. Based in Lozovatsky et al (2006) and Sutherland et al (2014), the miXed Layer Depth (XLD) is determined where ε falls to an assumed background level (first minimum value) in order to capture the dissipation rate away from the influence of sea surface processes. The Upper (UTD) and Lower (LTD/LPD) Thermocline/Pycnocline Depth was delimited as defined by Assunçao et al (2020). UTD corresponded to the depth where the vertical temperature gradient □□/□□ = 0.1 °C.m-1, while LTD/LPD were the last depth below the UTD at which N2 ≥ 10−4 s-2.~~

~~Vertical eddy diffusivity and turbulent flux of nutrients~~

~~The vertical eddy diffusivity coefficient (Kz) is calculated from ε following Osborn (1980) formulation as defined by Kz= ε Γ N−2. Here N2 is the buoyancy frequency squared was calculated using the sorted potential density profiles (σ_θ) from CTD-O2 profiles, via N2 = − (g/ρ0) (dσ_θ/dz) where ρ0 is a reference density (1025 kg.m−3) and g is the gravitational acceleration. Γ is a mixing efficiency defined as the ratio between the buoyancy flux and the energy dissipation, and is set to 0.2 which corresponds to the critical Richardson number Ri = 0.17 based in Osborn (1980). ε was linearly interpolated into the depths of N2.~~

Formatted: Font color: Custom Color(RGB(17;17;17)), Not Highlight

Formatted ...

Formatted: Space After: 0,65 pt

Formatted ...

Formatted ...

Formatted: Font: Not Bold, Font color: Custom Color(RGB(17;17;17))

Formatted ...

Formatted ...

Formatted ...

~~The vertical turbulent flux F (unit: mmol.m−2.s−1) of nutrients (nitrate and phosphate) was estimated from Kz as defined by:~~

~~$F_{(NO_3^-,PO_4^{3-})} = -K_{(NO_3^-,PO_4^{3-})}\left(\frac{\partial C_{(NO_3^-,PO_4^{3-})}}{\partial Z}\right)$, (1)~~

~~where $C_{(NO_3^-)}$ and $C_{(PO_4^{3-})}$ indicates the concentration of nitrate (NO3-) and phosphate (PO43-) (unit: mmol.L-1), respectively, and $K_{(NO_3^-)}$ and $K_{(PO_4^{3-})}$ indicates its vertical diffusivity, respectively. Here we assume $K_{(NO_3^-,PO_4^{3-})}$ is equivalent to Kz. The vertical profiles of nutrient concentrations (obtained from bottle sampling) were linearly interpolated into the depths of Kz.~~

Baroclinic currents

To analyze the processes explaining dissipation and mixing, particularly along internal tidal (IT) paths, we estimate shear instabilities associated with the semi-diurnal (M2) ITs and mean circulation, as well as their contributions to mixing.

The M2 tidal component of the tidal current is derived by calculating the baroclinic (semi-diurnal) tidal velocity $[u'', v'']$ (Fig. A3, Appendix), following these equations:

$$[u', v'] = [u, v] - [u_{bt}, v_{bt}], \quad (1)$$

$$[u_{bt}, v_{bt}] = \frac{1}{H}\int_{-H}^{0}[u, v]\, dz, \quad (2)$$

$$[u'', v''] = [u', v'] - [\overline{u'}, \overline{v'}]. \quad (3)$$

Here, $[u, v]$ represent total horizontal velocities (Fig. A3, Appendix) obtained from SADCP data. The components $[u', v']$ and $[u_{bt}, v_{bt}]$ represent baroclinic and barotropic components of horizontal velocities, respectively (Fig. A3, Appendix). H is water depth. The baroclinic mean velocities $[\overline{u'}, \overline{v'}]$ (Fig. A3, Appendix), calculated to estimate mean circulation along IT paths, are decomposed into along-shore $\overline{u'}_l$ and cross-shore $\overline{u'}_c$ velocities. The overbar denotes the average over a M2 tidal period.

Note that continuously collected SADCP for some stations (e.g., S11) are not sufficiently resolved due to gaps filled by interpolating between time points. The similar processing are applied to the CTD-O2 data collected alternately. SADCP time series data are less than 17 hours at all long stations, except for S14, which spans 42 hours. As a result, the diurnal and semidiurnal period fittings are not formally distinct (except at S14; Figs. A4 and A5, Appendix), and the inertial period (at least 5 days) cannot be resolved in our dataset. This limits our ability to separate currents by frequency and examine the associated dissipation.

The velocity profiles from LADCP are glued into our SADCP time series data below ~ 500 m depth at long stations.

To evaluate shear instabilities associated with ITs and the mean background circulation, we compute the baroclinic tidal vertical shear squared ($S^{2''}$) and mean shear squared ($\overline{S^{2'}}$) (Fig. A3, Appendix), as follows:

$$S^{2''} = (\partial u''/\partial z)2 + (\partial v''/\partial z)2, \quad (4)$$

$$\overline{S^{2'}} = (\partial \overline{u'}/\partial z)^2 + (\partial \overline{v'}/\partial z)^2. \quad (5)$$

Formatted ...

Formatted ...

Formatted ...

Formatted ...

Formatted ...

Formatted ...

Formatted ...

Formatted ...

Formatted ...

Formatted: Font color: Custom Color(RGB(17;17;17))

Formatted ...

Formatted: Font color: Custom Color(RGB(17;17;17))

Formatted: Font color: Custom Color(RGB(17;17;17))

Formatted: Font color: Custom Color(RGB(17;17;17))

Formatted ...

Formatted ...

Formatted ...

Formatted: Font color: Custom Color(RGB(17;17;17))

To evaluate the impact of bottom friction on mixing, we calculate kinetic energy $\varepsilon_f = \frac{1}{2}\rho_s(u_f^2)$ near the bottom boundary layer at shallow stations using friction velocity $u_f = u_b\sqrt{C_d}$, where C_d=2.5 x 10-3 is a drag coefficient obtained from the NEMO model. Huang et al. (2019) showed that the bottom boundary layer thickness spatially varies between 15-123 m in the Atlantic Ocean, with a median of ~ 30-40 m in the North Atlantic. We define bottom layer thicknesses in our study area based on measured bathymetry from CTD-O2 and near-bottom currents from ADCP. Here, ub is the total velocity averaged over a thickness of 20 m above the seabed for shallow stations and 40 m for deep stations.

The individual contributions of semi-diurnal ITs and mean circulation are then expressed as follows: $E^{''}/(\overline{E'} + E^{''})$ for tidal contribution and $\overline{E'}/(\overline{E'} + E^{''})$ for mean circulation contribution. Here, E = N*S. N is the buoyancy frequency and S is vertical shear. S can be substituted by $S^{2''}$ and $\overline{S^{2'}}$.

~~Baroclinic currents and energy~~

~~To evaluate the processes that can explain the mixing measured, the baroclinic (u', v') components of horizontal velocity was calculated $(u' = u - u_{bt}, v' = v - v_{bt})$ removing the barotropic (u_{bt}, v_{bt}) components of total horizontal current (u, v) provided by SADCP time series with LADCP profiles glued below ~ 500 m of depth, as shown by the equations below.~~

~~$[u', v'] = [u, v] - [u_{bt}, v_{bt}]$, (2)~~

~~$[u_{bt}, v_{bt}] = \frac{1}{H}\int_{-H}^{0} [u, v]dz$ (3)~~

~~The M2 tidal component of baroclinic currents is evidenced by baroclinic (semi-diurnal) tidal velocity (u'', v'') by removing ($[u'', v''] = [u', v'] - [\underline{u'}, \underline{v'}]$, with overbar the average over a tidal period) the baroclinic mean current $(\underline{u'}, \underline{v'})$ profile, and highlighted by baroclinic (semi-diurnal) tidal shear squared $S^{2''}$ ($S^{2''}$ = (∂u''/∂z)2 + (∂v''/∂z)2) compared at the baroclinic mean vertical shear squared $\underline{S}^{2'}$ ($\underline{S}^{2'}$ = (∂$\underline{u'}$/∂z)2 + (∂$\underline{v'}$/∂z)2).~~

~~The vertically sheared total baroclinic current can be converted to total baroclinic energy following internal waves parameterization of dissipation rates (εMG) by Mackinnon and Gregg (2003) and validated by Xie et al. (2013), as defined by:~~

~~εMG = ε0 (N/N0) (S/S0), (74)~~

~~with N the buoyancy frequency from CTD-O2 profiles and S the vertical shear from baroclinic currents. N0=S0=0.0052 s-1 and ε0=2.2 10-9 W.kg-1 (adjustable constant).~~

~~By simple substitution in this formulation, we computed the baroclinic tidal energy (ε''MG) and baroclinic energy of mean circulation (ε'MG) in order to obtain the individual contribution (ε'MG/(ε'MG + ε''MG) for mean baroclinic energy and ε''MG/(ε'MG + ε''MG) for M2 semi-diurnal baroclinic energy) to the total baroclinic energy (ε'MG + ε''MG).~~

~~To evaluate the bottom friction effect, the kinetic energy $\varepsilon_f = \frac{1}{2}\rho_s\langle u_f^2\rangle$ close to the bottom boundary layer was computed using friction velocity $u_f = u_b\sqrt{C_d}$. C_d=2.5 10-3 is the drag coefficient from a high-resolution NEMOv3.6 model (1/36°) (Nucleus for European Modeling of the Ocean; Madec et al., 2019). Previous study of Huang et al. (2019) shown that the bottom boundary thickness spatially varies between 15-123 m in Ocean Atlantic with a medianwith median of about 30-40 m in the North Atlantic. Bottom layer thicknesses were defined in our study area depending on the measured bathymetry from CTD-O2 and near-bottom currents from ADCP. u_b is the total velocity over 15 m (40 m) thick above the seabed for shallow (deep) stations.~~

Ray tracing calculation

Analyzing both the mean~~vertical profiles of the average~~ currents and the spatial dimension along the IT pathways offers~~is~~ another insight~~way~~ into the mechanisms responsible for observed mixing (Rainville and Pinkel, 2006)~~to better understand the mechanisms related to the measured mixing~~. IT energy rays are generated in regions with steep topography, such as the shelf break, where IT slope matches with the bottom slope (i.e., critical slopes) before propagating within the ocean interior.~~The rays of ITs energy are generated at steep topography regions (e.g., shelf-break) where ITs beams and the bottom slope match together (i.e. critical slopes) and then propagate within the ocean interior~~. These rays, moving both downward and upward, encounter the seasonal pycnocline, resulting in beam scattering and the formation of large IT oscillations. As these oscillations steepen, they disintegrate into nonlinear ISWs, a process known as "local generation" of ISWs~~After seafloor reflection, these IT beams propagate upward and impinge on the seasonal pycnocline from below (resulting in beam scattering) and create large ITs oscillations, which after steepening have been documented to disintegrate into nonlinear ISWs – known as a "local generation" for the ISWs~~ (New and Pingree, 1992). To explore IT paths, ray-tracing techniques are employed, as previously used by New and Da Silva (2002) and Muacho et al. (2014)~~Theoretical analysis of IT paths was computed using IT ray-tracing techniques previously used (New and Da Silva, 2002; Muacho et al., 2014)~~, to investigate the effectiveness and expected pathways of the IT beams off the Amazon shelf. One main assumption in our linear-theory-based hypothesis is that stratification remains horizontally uniform along the IT propagation path, although in reality, it may vary ~~One main hypothesis we made using linear theory is to consider that the stratification is constant horizontally along the IT propagation path. Whereas in reality it may vary,~~ due to submesoscale and mesoscale variability. This limitation makes the ray tracing approach less realistic but still useful as a first-order estimate of energy distribution. The IT ray-~~–~~tracing calculation assumes that in a continuously stratified fluid, ITs energy can be described by characteristic pathways of beams (or rays) with a slope c to the horizontal~~ following~~:

$$c = \pm\left(\frac{\sigma^2 - f^2}{N^2 - \sigma^2}\right)^{1/2}, \qquad (6\cancel{8})$$

Formatted ...

Formatted ...

Formatted ...

Formatted ...

Formatted ...

Formatted ...

where σ is the M2 tidal frequency (1.4052x10-4 rad ~~.~~s-1), and f is the Coriolis parameter. N2 are obtained from time-averaged AMAZOMIX CTD-O2, glued with monthly N2 profiles from Amazon36 (NEMO model outputs, 2012-2016) below 1000 m depth. Amazon36 is a NEMO configuration, specifically designed to cover the western tropical Atlantic from the mouth of the Amazon River to the open sea (see Tchilibou et al., 2022; Assene et al., 2024; for configuration details and model description)~~The N2 from CTD-O2 AMAZOMIX 207 data were first time-averaged to obtain the mean stratification at stations. Then, the monthly Amazon36 (2012-2016) N2 208 obtained from NEMO model outputs (see Tchilibou et al., 2022; Assene et al., 2024, for model description) were smoothed and stitched to the AMAZOMIX N2 profiles below 1000m depth~~. IT ray-tracing diagrams are performed~~were obtained~~ along ~~the 5~~ the transects ~~(T1 to T5;, Fig. 1a)~~. Seasonal sensitivity tests of rays (August, September, October, and April) are conducted by varying the critical slope positions and N2 to explore its influence and generate a set of ray paths consistent with characteristics of IT pathways (Figs. A6 and A7, Appendix)~~Sensibility tests of IT rays with different seasons (August, September, October and April) were performed varying the position of critical topography in order to get an envelope of ray paths consistent with characteristics of IT pathways~~.

3 Results

3.1 Mixing

3.1.1 Thermohaline and IT features

~~In this section we analyze density profiles to gain information on the mixing and/or on waves propagation. First we observe step-like features in the density profiles (Fig. 3b and 3c). During the M2 tidal period, step-like structures of ~20-40 m thick are found at depths ranging from 80-160 m at S10, S12, S13, and S14 (Fig. 3b). They are thicker along the IN-ITs transect T1 than along other transects (T2–T4) (Fig. A1.a and A1.b, Appendix). Then, between 60 and 170 m depth, large vertical displacements of 20 to 60 m are detected along T1-T2 and T4 (e.g., 40 m at S10, 48 m at S6, 52 m at S13, and 32 m at S14) (Fig. 3b and 3c). The smallest displacements (e.g., ~8 m at S25) are observed along OUT-ITs transect T5 (Fig. A1.b, Appendix). Finally, the vertical displacement of the IT wave may also be detected in the variability of the mixed layer depth (MLD), which ranges from 18 to 84 m over a semi-diurnal cycle (see Fig. 6.e). As a preliminary conclusion, both step-like structures and isopycnal displacements support the hypothesis of propagating ITs, that can have stronger energy along transects T1 and T2, weaker on T3, T4, and almost absent on T5 (Fig. 1a).~~

In this subsection, we analyze the density profiles to gain insight into mixing processes and/or wave propagation. Step-like features are observed in the density profiles (Figs. 3a and 3b). During the M2 tidal period, step-like structures ~20-40 m in length occur at depths ranging from 80 to 160 m at stations S10, S12, S13, and S14 (Fig. 3a). These features are more

Formatted: Font color: Custom Color(RGB(17;17;17)), Not Superscript/ Subscript

Formatted: Font color: Custom Color(RGB(17;17;17))

Formatted: Font color: Custom Color(RGB(17;17;17)), Not Superscript/ Subscript

Formatted: Font color: Custom Color(RGB(17;17;17))

Formatted: Font color: Custom Color(RGB(17;17;17)), Not Superscript/ Subscript

Formatted: Font color: Custom Color(RGB(17;17;17))

Formatted: Font color: Custom Color(RGB(17;17;17)), Not Superscript/ Subscript

Formatted: Font color: Custom Color(RGB(17;17;17))

Formatted: Font color: Custom Color(RGB(17;17;17)), Not Superscript/ Subscript

Formatted: Font color: Custom Color(RGB(17;17;17))

Formatted: Font color: Custom Color(RGB(17;17;17)), Not Superscript/ Subscript

Formatted: Font color: Custom Color(RGB(17;17;17))

Formatted: Font color: Custom Color(RGB(17;17;17)), Not Highlight

Formatted: Font color: Custom Color(RGB(17;17;17)) pronounced along the IN-ITs transect Aa and Ab compared to the other transects (e.g., E and G; Figs. A8.a and A8.b, Appendix).

In this layer (between 60 and 170 m depth), significant vertical displacements, ranging from 20 to 60 m, are detected along transects Aa, Ab, and E (e.g., 40 m at S10, 48 m at S6, 52 m at S13, and 32 m at S14; Figs. 3a and 3b). The smallest displacements (~8 m at S25) are observed along the OUT-ITs transect G (Fig. A8.b, Appendix). These vertical displacements are also evident in the variability of the mixed layer depth (MLD), which fluctuates between 18 and 84 m over a semi-diurnal cycle (figure not shown).

In conclusion, the presence of step-like structures and isopycnal displacements suggests strong mixing in the water column, and supports the hypothesis of ITs propagating, with stronger energy along transects Aa and Ab, weaker energy along D and E, and almost absent along G (Fig. 1a).

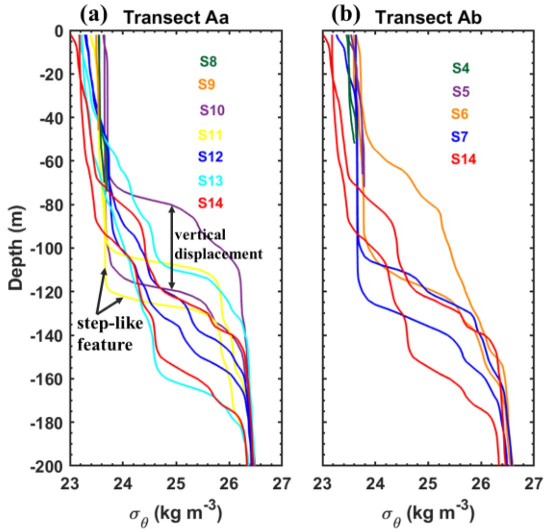

Figure 3: Density profiles (σ_θ, kg m-3) obtained from CTD-O2 measurements during the AMAZOMIX 2021 cruise for stations S4 to S14 along transects (a) Aa and (b) Ab, located within IT fields. For long stations (S6, S7, and S10-S14), two

Formatted: Indent: Left: -0,01 cm, Right: 0,09 cm, Space Before: 0 pt, After: 0,25 pt, Line spacing: Multiple 1,54 li density profiles are shown to highlight step-like structures and isopycnal vertical displacements (illustrated by black arrows) along the transects. Distinct colors are used to represent each station within each transect. The density values for stations S4, S5, S8, and S9 range between 23.4 and 23.8 kg m-3.

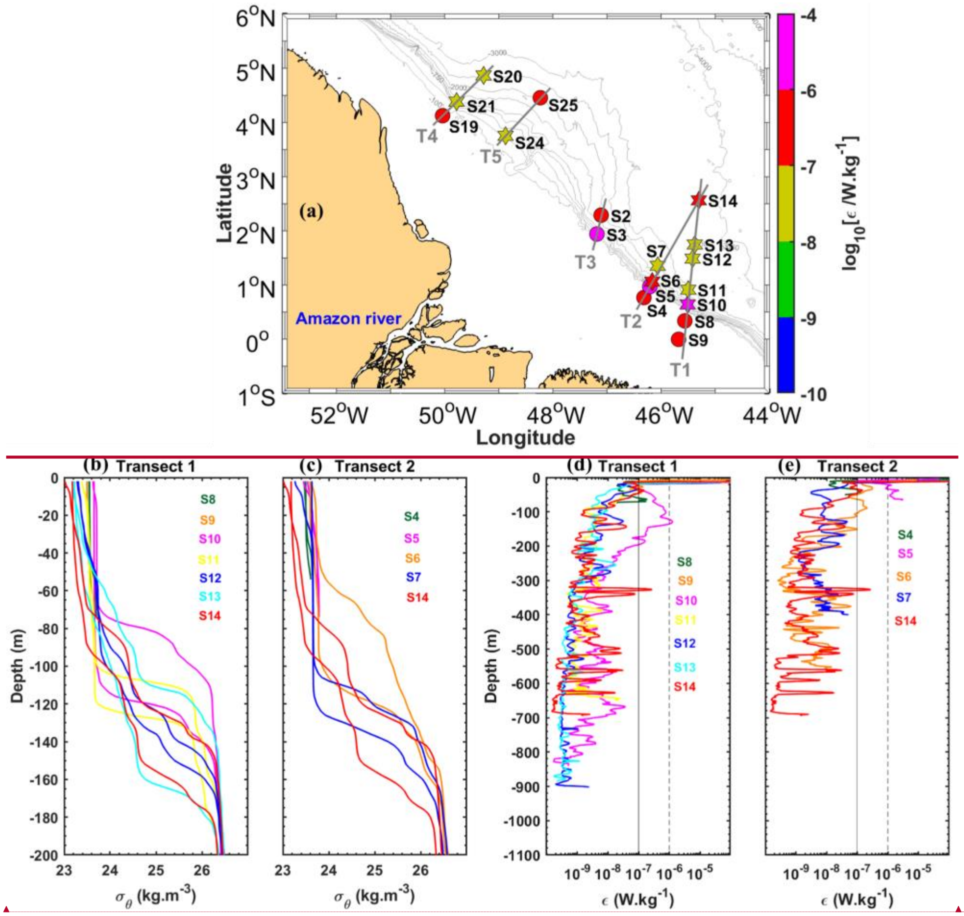

Formatted: Font: 10 pt

Formatted: Font: 10 pt

~~Figure 3: (a) Horizontal (maximum) dissipation rates (ε, W.kg^{-1}, on log scale) from VMP during the AMAZOMIX 2021 cruise for all stations/transects T1 to T5. (b) (c) Density profiles (in kg.m^{-3}) from CTD-O$_2$ and (d) (e) vertical dissipation rates (ε in W.kg^{-1}, on log scale) from VMP during the AMAZOMIX 2021 cruise for the transects/stations inside of the IT fields (b) (d) T1 (S8-S14) and (c) (e) T2 (S4-S7 and S14). For long stations (S6, S7 and S10-14), two density profiles are used to illustrate the step-like structures and isopycnal vertical displacements along the transects. Colour is used to distinguish each station in each transect. Dashed and solid back lines (on panels c and d) are for comparison. The density of S4 and S5 vary between 23.4-23.8 kg/m^{-3}.~~

Formatted: Font: Not Italic

Formatted: Font: Not Italic, Not Superscript/ Subscript

Formatted: Font: Not Italic

Formatted: Font: Not Italic, Not Superscript/ Subscript

Formatted: Font: Not Italic

Formatted: Font: Not Italic, Not Superscript/ Subscript

Formatted: Font: Not Italic

Formatted: Font: Not Italic, Not Superscript/ Subscript

Formatted: Font: Not Italic

Formatted: Font: Not Italic, Not Superscript/ Subscript

Formatted: Font: Not Italic

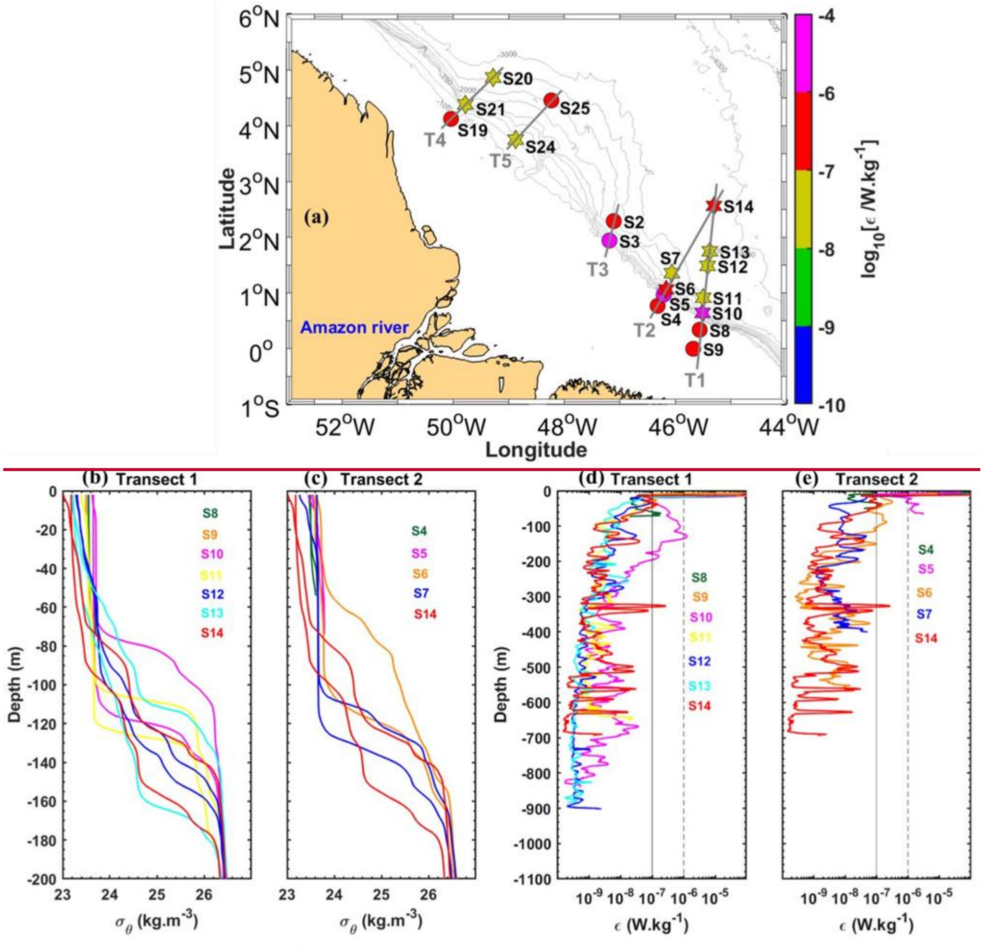

~~Figure 3: (a) Horizontal (maximum) dissipation rates (ε, W.kg-1, on log scale) from VMP during the AMAZOMIX 2021 cruise for all stations/transects T1 to T5. (b)-(c) Density profiles (in kg.m-3) from CTD-O2 and (d)-(e) vertical dissipation rates (ε in W.kg-1, on log scale) from VMP during the AMAZOMIX 2021 cruise for the transects/stations inside of the IT~~

Formatted: Font: Not Italic

Formatted: Font: Not Italic, Not Superscript/ Subscript

Formatted: Font: Not Italic

Formatted: Font: Not Italic, Not Superscript/ Subscript

Formatted: Font: Not Italic

Formatted: Font: Not Italic, Not Superscript/ Subscript

Formatted: Font: Not Italic

Formatted: Font: Not Italic, Not Superscript/ Subscript

Formatted: Font: Not Italic

~~fields (b)-(d) T1 (S8-S14) and (c)-(e) T2 (S4-S7 and S14). For long stations (S6, S7 and S10-14), two density profiles are used to illustrate the step-like structures and isopycnal vertical displacements along the transects. Colour is used to distinguish each station in each transect. Dashed and solid back lines (on panels c and d) are for comparison. The density of S4 and S5 vary between 23.4-23.8 kg/m-3.~~

3.1.2 TKE Dissipation rates and mixing

Along the transects, we analyze the distribution of dissipation rates (ε) and mixing coefficient (Kz) estimated below the XLD (Table A1, Appendix) to characterize the mixing processes occurring off the Amazon shelf. It is important to note that the XLD is typically deeper than the MLD at all stations (except at S8, S10, and S25), which is calculated using a density threshold 0.01, 0.02 or 0.03 kg m-3 (Fig. A2, Appendix).

Our results show that dissipation rates vary between [10-10, 10-5] W kg-1 from the continental shelf to the open sea (Fig. 4). Mapping the maximum value of ε over the water column (Fig. 4a) reveals that the strongest ε at the generation sites, within the range of [10-6, 10-5] W kg-1, occur at the IN-ITs transects except at E (S21), with even higher ε values found at the shelf-break (at stations S3, S5, and S10). Smaller ε values, within the range of [10-8, 10-7] W kg-1, are observed away from the shelf-break (e.g., at S7, S9, S11, S19, S24, and S20), with the exception of some deep-sea stations (e.g., at S14 and S25) where ε are still high.

The vertical profile of ε (Figs. 4b and 4c, and Figs. A8c and A8d, Appendix) shows stronger dissipation (10-7-10-6 W kg-1), between 24-160 m depth, in the thermocline layers at stations on the shelf-break (S6 and S10) and in the open ocean (e.g., at S14, and S25). Hotspots of mixing, within the range of [10-8, 10-7] W kg-1, are observed at various depths (e.g., 271 m and 375 m) at station S6, (e.g., 562 m, and 668 m) at S10, (e.g., 127 m, and 192 m) at S7 and (e.g., 138 m and 186 m) S24. For shelf/shallow stations within the ITs regions (S3 and S5; Fig. 4c, and Fig. A8.c, Appendix), mixing is more pronounced, between [10-6, 10-5] W kg-1, near the bottom layer.

Similar to the dissipation patterns, higher Kz values are observed at IN-ITs stations (Figs. 4d and 4e, and Figs. A8e and A8f, Appendix), ranging from 10-3 to 10-1 m2 s-1, particularly in the upper layer (0-120 m) (e.g., at S6, S7, and S10), and also near the bottom layer (e.g., at S5, S8, and S9). Below 100 m depth, Kz decreases but remains significant, with values between [10-4, 10-3] m2 s-1 (e.g., at S2, S10 S11, and S20). At OUT-ITs stations along transect G (Fig. A8f, Appendix), Kz reaches higher values (exceeding 10-4 m2 s-1) in the mixed layer (0-35 m) and below 200 m depth (at S25). Notably, the shallow station S3 exhibits the strongest mixing coefficient in this region, exceeding 10-0 m2 s-1.

Formatted: Font: Not Italic, Not Superscript/ Subscript

Formatted: Font: Not Italic

Formatted: Font: Bold

Commented [4]:

Commented [5]:

In conclusion, the dissipation rates vary by 2-3 orders of magnitude over depth, with stronger mixing observed on the Amazon shelf and shelf-break compared to stations located farther from these areas. Additionally, the strongest mixing is observed in regions influenced by ITs. To further understand the heterogeneous distribution of ε, the next section will investigate the processes responsible for this variability, focusing on shear instability driven by the dynamics of the currents observed in this region.

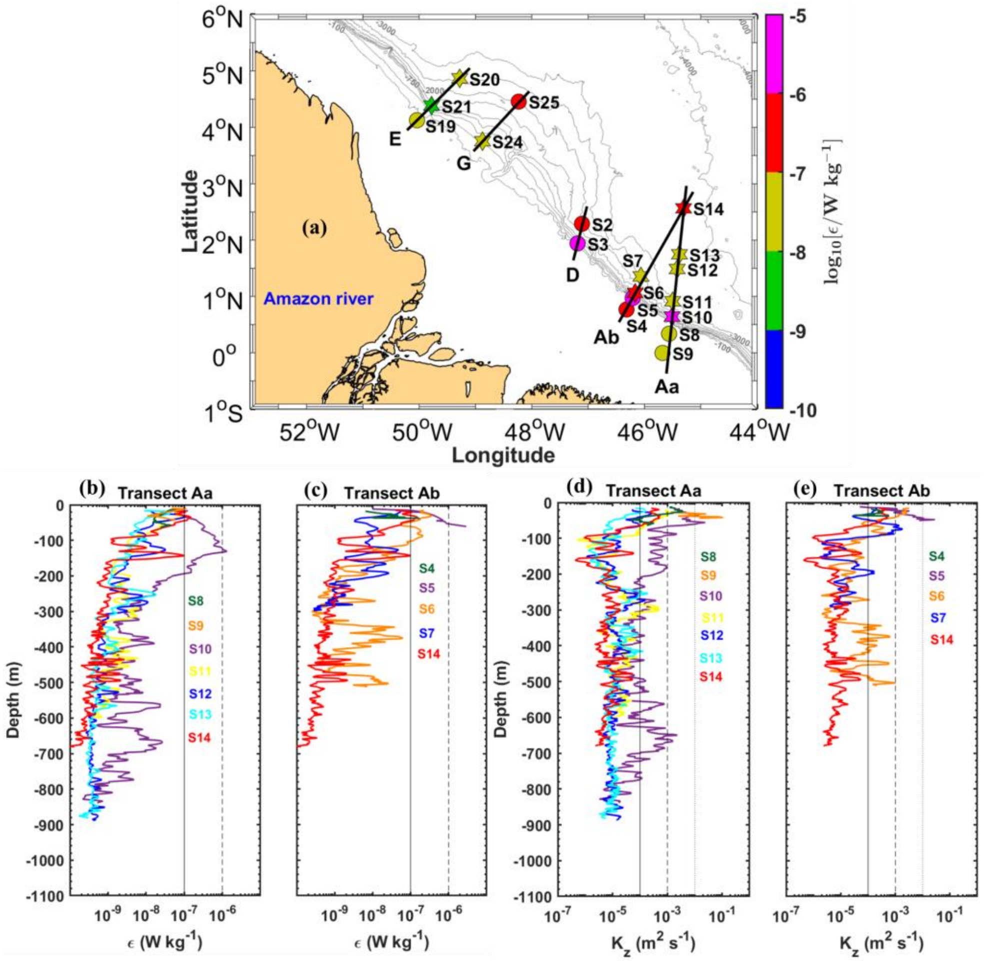

Figure 4: (a) Horizontal maximum dissipation rates (ε, in W kg-1, on a logarithmic scale) measured with the VMP below the XLD during the AMAZOMIX 2021 cruise for all stations along transects Aa, Ab, D, E, and G. (b)-(c) Vertical dissipation

profiles and (d)-(e) vertical diffusivity profiles (Kz, in m2 s-1, on a logarithmic scale) for stations along transects Aa and Ab, respectively. Distinct colors are used to represent each station within each transect. Dashed and solid black lines in panels (b) to (e) are included for comparison purposes.

~~Now, we analyze the distribution of dissipation rates (ε) estimated below the mixing layer depth (hereinafter XLD), in order to characterize the mixing produced off the Amazon shelf. Note that the XLD (Table A1, Appendix) is generally deeper than the MLD.~~

~~Results show that from the continental shelf to the open sea ε vary within the range of [10-10,10-4] W.kg-1. Mapping the maximum value of ε over the water column (Fig. 3a, 3d and 3e) reveals that the strongest ε within [10-6,10-4] W.kg-1 are observed on IN-ITs transects (T1-T3), and even larger ε are found on the shelf-break at generation site of ITs (S3, S6 and S10). Smaller ε values (between [10-8,10-7] W.kg-1) are found away from the shelf-break (e.g., at S7, S11, S24 and S20), except at some deep-sea stations (e.g., at S14 and S25).~~

~~The vertical profile of ε (Fig. 3d and 3e, and Fig. A1.c and A1.d, Appendix), show stronger ε (10-7-10-6 W.kg-1) in the thermocline layers (~120 m) for the stations close to the shelf-break and in the ITs influence (S6 and S10). Hotspots of mixing are found almost anywhere at S14 in the water column, for example, at 150, 300, 350, 500, 600 and 700 m depth. Finally for shelf stations in the ITs regions, S3 and S5, mixing increases close to the bottom.~~

~~As another preliminary conclusion, the distribution of ε ranges by 2-3 orders of magnitude over depth, and indicates stronger mixing on the Amazon shelf and shelf-break compared with those located far from these areas, and even stronger in the regions of occurrences of ITs. In order to investigate the precise reasons for such heterogeneous distribution of ε the aim of the next section will be to try to identify the different processes responsible for it, by looking at shear instability driven by the current measurements.~~

Formatted: Not Superscript/ Subscript

Formatted: Not Superscript/ Subscript

Formatted: Not Superscript/ Subscript

Formatted: Not Superscript/ Subscript

Formatted: Not Superscript/ Subscript

Formatted: Not Superscript/ Subscript

Formatted: Not Superscript/ Subscript

Formatted: Not Superscript/ Subscript

Formatted: Not Superscript/ Subscript

Formatted: Not Superscript/ Subscript

Formatted: Not Superscript/ Subscript

Formatted: Not Superscript/ Subscript

Formatted: Font: Not Italic

3.2 Processes contributing to mixing

In this section, we explore which processes among tides, general circulation, and friction are responsible for the high mixing activity observed off the Amazon shelf.

3.2.1 Baroclinic tidal current

The contribution of ITs to the baroclinic velocity structure is analyzed using the time series of baroclinic tidal currents (Figs. 5a, 5c, and 5e, and Figs. A9 to A15, Appendix). The semi-diurnal (M2) component of the tidal current, characterized by alternating positive (red) and negative (blue) velocities, is distinctly observed along transects Aa and Ab, particularly within (24-26 kg m-3 isopycnals; 70-180 m depth) and below the pycnocline. The tidal signal is strongest between 80-350 m depth, along transects Aa (e.g., at S10, S11, and S14) and Ab (e.g., at S6), while along transect E (e.g., at S21), it is more prominent in the upper layer (0-120 m). In contrast, along transect G, the signal becomes noisier but remains stronger near the bottom layer, particularly at the OUT-ITs station S24.

The baroclinic tidal velocities reveal a superposition of 3-5 tidal modes at IN-ITs stations (Figs. 5a, 5c, and 5e, and Figs. A9 to A15, Appendix). A greater number of modes is observed near the shelf-break (e.g., 4 modes at S6 and 5 modes at S10), while fewer modes are detected far from (e.g., 3 modes at S7, S12 and S14). Higher tidal velocities ranging from 25-50 cm s-1 are found between 80-350 m along transects Aa and Ab (e.g., at S6, and S10). In contrast, lower tidal velocities, typically below 25 cm s-1, are more pronounced along transect E (e.g., at S20, and S21) to OUT-ITs stations along transect G (e.g., at S24).

Consistent with the tidal signal patterns, the strongest vertical tidal shear, reaching up to 10-3 s-2 is observed at IN-ITs stations where the large vertical displacements in N2 maxima are detected (e.g., S6, S10, and S14), except at S7, S11, S20, and S21 (Figs. 6a, 6c, and 6e, and Figs. A16 to A18, Appendix). These latter stations, and the OUT-ITs station S24, exhibit lower but still notable shear, reaching to 10-4 s-2. Dissipation rates, previously presented in subsection 3.1.2 and shown in Fig. 4, are found to be 2-3 orders of magnitude higher in the pycnocline compared at greater depths.

The analysis of baroclinic tidal currents reveals significant contributions from ITs, particularly in the pycnocline, with strong vertical shears observed near the shelf-break. Dissipation rates are notably higher in the pycnocline than at greater depths, especially in regions influenced by ITs. These findings underscore the role of internal tides in driving mixing processes in the Amazon shelf area.

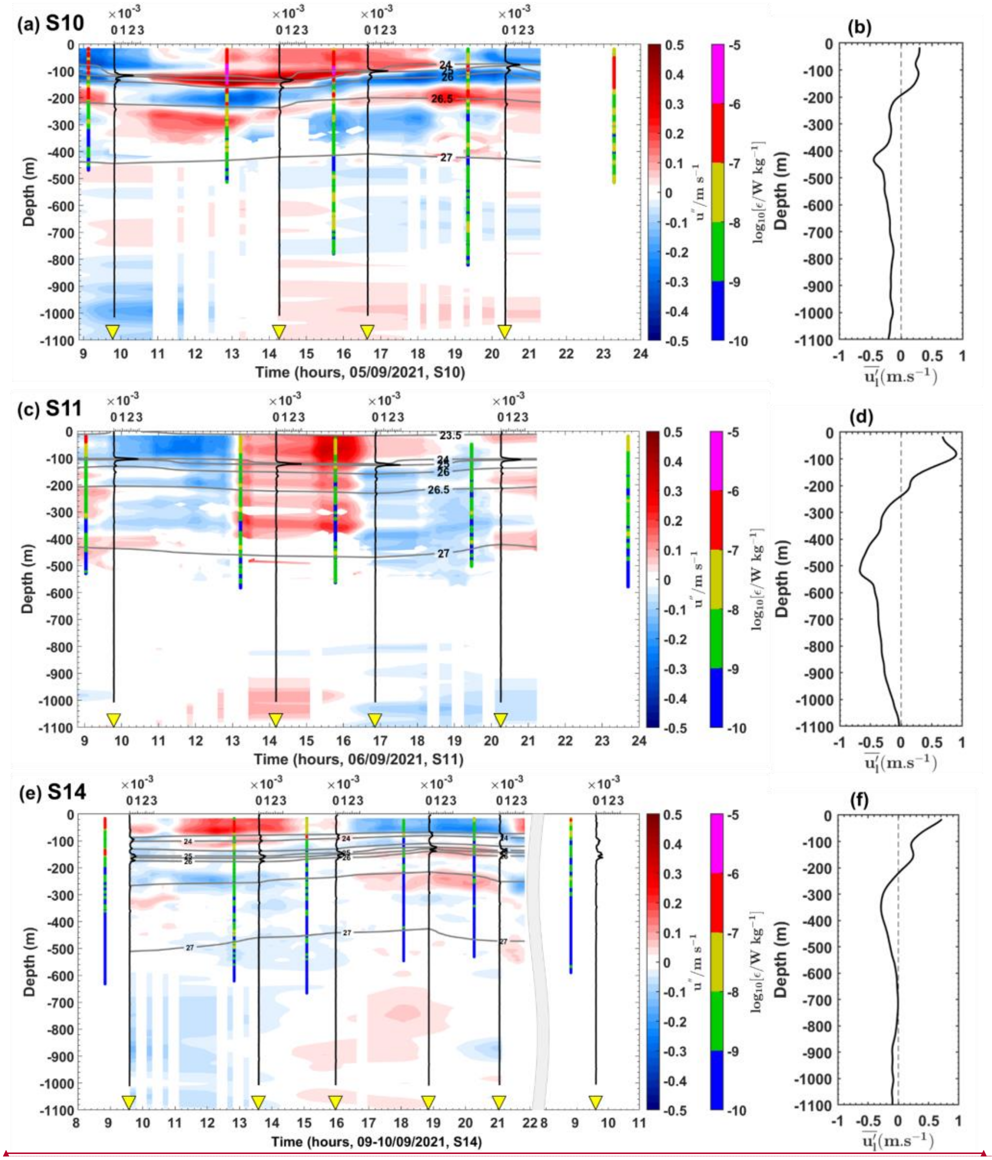

Formatted: Font: 12 pt

Formatted: Font: 12 pt

Figure 5: Semi-diurnal baroclinic zonal currents (u'', in m s-1) from the ADCP for stations (a) S10, (c) S11, and (e) S14. Panels (a), (c), and (e) also display the buoyancy frequency squared (N2, in s-2) represented by vertical black lines, potential density represented by grey contours, and dissipation rate profiles (ε, in W kg-1, on a logarithmic scale) represented by vertical colored bars. Along-shore mean baroclinic currents ($\overline{u'}_l$, in m s-1) from the ADCP for stations (b) S10, (d) S11, and (f) S14.

Formatted: Font: 12 pt

Formatted: Font: 12 pt

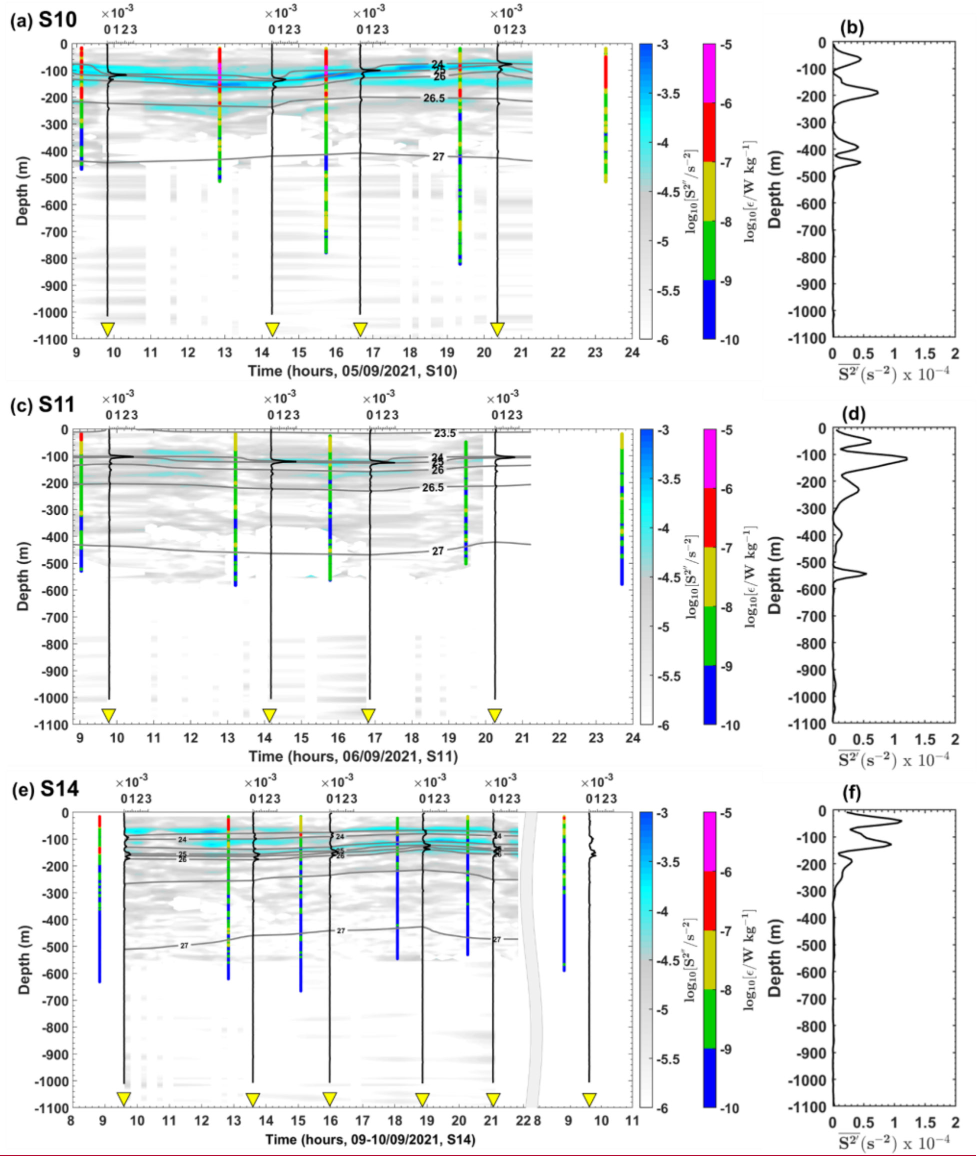
(a) S10
(b)
(c) S11
(d)
(e) S14
(f)
×10⁻³
0 1 2 3
Depth (m)
Time (hours, 05/09/2021, S10)
Time (hours, 06/09/2021, S11)
Time (hours, 09-10/09/2021, S14)
log10[S2'/s-2]
log10[ε/W kg-1]
S2' (s-2) x 10-4
23.5
24
25
26
26.5
27

Figure 6: Semi-diurnal baroclinic vertical shear squared ($S^{2''}$, in m s-1, on a logarithmic scale) for stations (a) S10, (c) S11, and (e) S14. Panels (a), (c), and (e) also display the buoyancy frequency squared (N2, in s-2) represented by vertical black lines, potential density represented by grey contours, and dissipation rate profiles (ε, in W kg-1, on a logarithmic scale) represented by vertical colored bars. Mean baroclinic vertical shear squared ($\overline{S^{2'}}$, in m s-1) for stations (b) S10, (d) S11, and (f) S14.

Formatted: Font: Not Italic

~~The contribution of the ITs to the total baroclinic velocity structure is shown (Fig. 4a.1 to 4c.1, and Fig. A2.a.1 to A2.g.1, Appendix) by the temporal evolution of the baroclinic tidal current. The semi-diurnal M2 component of the baroclinic current is easily identified by alternating positive (red bands) and negative (blue bands) velocities along T1-T4. For the IN-ITs stations (Fig. 4a.1 to 4c.1, and Fig. A2.a.1 to A2.f.1, Appendix), M2 component signal is strong between depths of 100-300 m (e.g., at S10-S14) and 100-400 m (e.g., at S6) and 200-450 m (e.g., at S21). Whereas the signal is noisier at depth for OUT-ITs stations (e.g., at S24) along T5 (Fig. A2.g.1, Appendix). The baroclinic tidal velocity shows a superposition of several (03-05) tidal modes. A high number of modes are observed on the shelf-break (e.g., 04 modes at S6 and 05 modes at S10). While a low number of modes away from the shelf-break (e.g., 03 modes at S7, S12 and S14). The highest baroclinic tidal current velocities were observed (between 25-48 cm.s^{-1}) at sites Aa and Ab along T1-T2. Whereas lower tidal velocities (< 25 cm.s^{-1}) are found in site F along T4 (e.g., at S20 and S21) compared to OUT-ITs stations (e.g., at S24). The strong vertical shears (> 10^{-3} s^{-2}) of the baroclinic tidal velocities are clearly localized in the pycnocline (between 80-180 m depth) for the IN-ITs stations (e.g., at S6, S10 and S12). While weak vertical tidal shears (< 10^{-3} s^{-2}) are observed at greater depths. At these stations (e.g., S6, S10 and S14), the large vertical displacements of maximum N^2 were also encountered in pycnocline over tidal period. The dissipation rates (ε) already presented in section 3.1.2, is also reported on Fig. 3. ε shown over the tidal period at long stations (e.g., at S6, S10 and S14) are found 2-3 orders of magnitude stronger in the pycnocline than at depth.~~

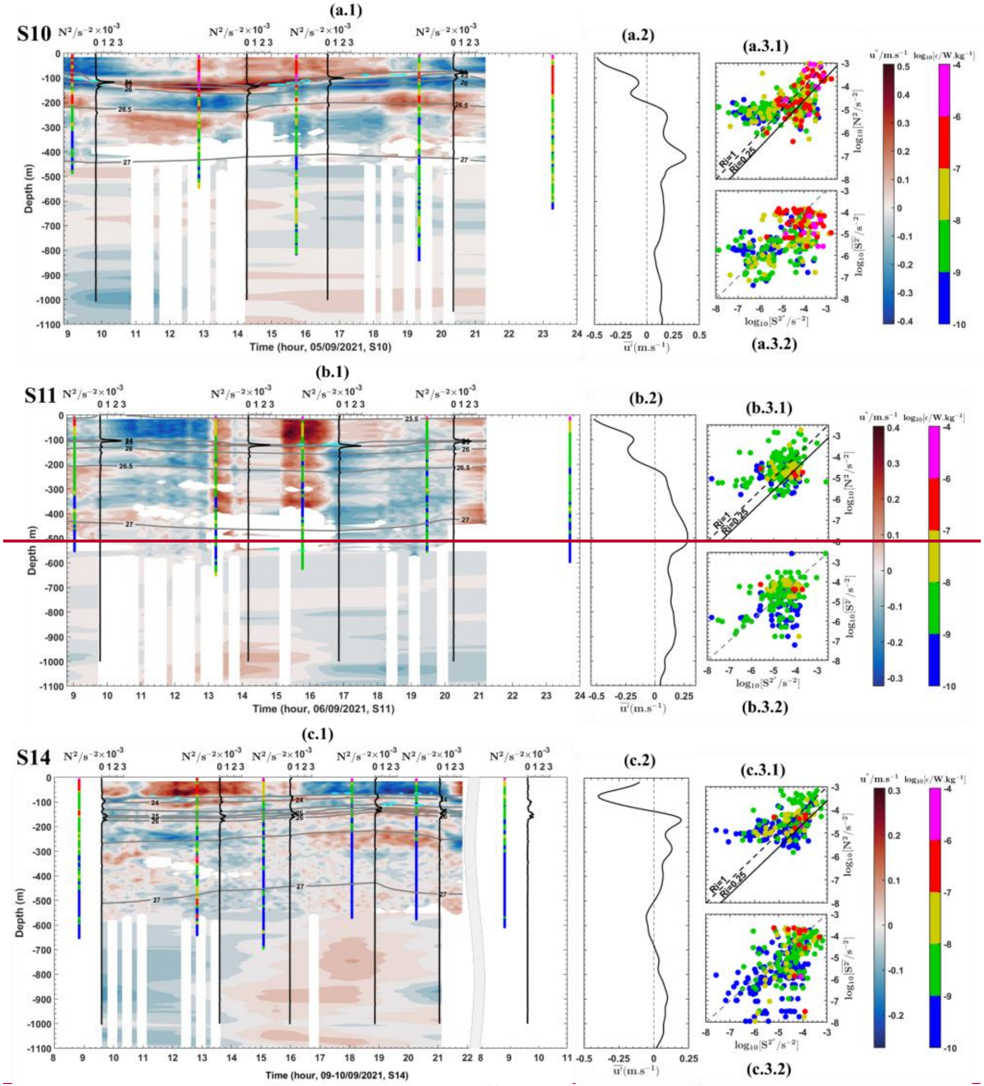
(a.1)
S10
N²/s⁻²×10⁻³
0 1 2 3
Depth (m)
Time (hour, 05/09/2021, S10)
(a.2)
u'(m.s⁻¹)
(a.3.1)
(a.3.2)
Ri=1
Ri=0.25
log₁₀[N²/s⁻²]
log₁₀[S²/s⁻²]
u'/m.s⁻¹
log₁₀[ε/W.kg⁻¹]
(b.1)
S11
Time (hour, 06/09/2021, S11)
(b.2)
(b.3.1)
(b.3.2)
(c.1)
S14
Time (hour, 09-10/09/2021, S14)
(c.2)
(c.3.1)
(c.3.2)

525

~~*Figure 4: (1st column: a.1 to c.1) Semi-diurnal (u'' in m.s^{-1}) baroclinic zonal currents from ADCP overlaid the semi-diurnal vertical shear squared ($S^{2''}$in s^{-2} x10^{-3} with the following contours values: 1.2 at S10, 0.6 at S11 and 0.8 at S14, in cyan contours) from ADCP, the buoyancy frequency squared (N^2 in s^{-2}, in vertical black lines) and potential density (in grey contours background shift) from CTD-O_2 and dissipation rates (ε in W.kg^{-1} on log scale, in coloured bars) profiles from VMP. (2nd column: a.2 to c.2) Mean baroclinic (alongshore current) velocity ($\bar{u}'$ in m.s^{-1}) from ADCP. (3rd column: a.3.1 to c.3.1) ε as a function of $S^{2''}$ and N^2 overlaid Richardson number (with critical value Ri=0.25 in solid black line and Ri=1 in dashed black line). (3rd column: a.3.2 to c.3.2) ε as function of mean vertical shear squared ($\bar{S}^{2'}$ in s^{-2}) and $S^{2''}$ overlaid dashed grey line for comparison. (first line, panels a) for S10, (second line, panels b) for S11 and (third line, panels c) for S14. N^2 was linearly interpolated into the depths of $S^{2''}$ to have same vertical scales.*~~

3.2.2 Mean baroclinic current

The contribution of the mean baroclinic current is diagnosed through the across- and along-shore components of mean baroclinic velocities, defined parallel and perpendicular to the 200 m depth isobath, respectively, as proxies for the main circulation patterns in the region. Along-shelf velocities are defined as positive northwestward and negative southeastward, while across-shelf velocities are positive northeastward and negative southwestward (Figs. 5b, 5d, and 5f, and Figs. A9 to A15, Appendix).

A strong surface flow is observed crossing transects Aa and Ab (e.g., at S6, S7, S11-S14), with along-shore northwestward velocities exceeding 68 cm s-1 in the upper layer of 200 m (Fig 5, and Figs. A9, A10, A12, A13, A14, and A19, Appendix). This flow is notably stronger compared to the across-shore velocities and decreases in strength with depth, transitioning towards the subsurface layer. Below 200 m depth along transects Aa and Ab, a southeastward along-shore flow emerges with velocities below 30 cm s-1, but increases up to 50 cm s-1 between 400 and 550 m depth at stations S6, S7, and S11. This southeastward baroclinic flow becomes weakly unstable at IN-ITs stations S13 and S14 below 500 m depth.

Similar dominant along-shore flows are observed along transect G (Figs. A11, A15, and A19, Appendix). At the OUT-ITs station S24, northwestward velocities reach up to 50 cm s-1 above 80 m depth, while southeastward velocities below 80 m remain weaker (< 30 cm s-1).

Above 4°N along transect E, the flow directions reverse throughout the water column, with the along-shore component dominating (Figs. A11, A15, and A19, Appendix). In the upper layer of 120 m, the along-shore flow is stronger (~ 45 cm s-1) and directed northwestward at S20, while at S21, it is weaker and shifts southeastward. Below this layer, between 120–400 m depth, the flows become more unstable and opposing, with the along-shore velocities being stronger (~28 cm s-1) at S21 compared to S20.

The mean baroclinic flows exhibit various peaks of mean shear instability, ranging from 10-5 to 10-3 s-2, in the first 600 m depth along transects (Figs. 6b, 6d, and 6f, and Figs. A16 to A18, Appendix). Vertical shear is more pronounced within the range of [0.5, 1.5] x 10-4 s-2 around the pycnocline, between 40 and 200 m depth along transects Aa, Ab and G (e.g., at S6, S7, S10, S11, S14, and S24). This shear strength increases further along transects E, reaching up to 2.5 x 10-4 s-2 at the base of the pycnocline, around 112 m depth at S20.

~~Now, the contribution of the mean baroclinic current is diagnosed by the alongshore baroclinic velocities (taken parallel to the 200 m depth isobath) as a proxy of the main circulation pattern in the region. A surface alongshore northwestward flow crossing transects T1 and T2 (e.g., at S6, S7, and S10-S14) is observed stronger with mean (negative) velocities exceeding 40 cm.s^{-1} in the upper layer of 120 m (Fig. 4a.2 to 4c.2, and Fig. A2.a.2 to A2.d.2, Appendix). It moves with decreasing velocities towards the subsurface layer. Below 130 m depth on these transects (T1 and T2), a flow with relatively low (positive) velocities (~ 25 cm.s^{-1}) is observed towards the southeast. In this layer, there are extremes of (positive) velocities (e.g., at S10, S11 and S13) and also direction reversals below 300 m (e.g., at S13 and S14). In contrast, a surface flow crossing T4 (Fig. A2.e.2 and A2.f.2, Appendix) is found moving southeastward in the first 100 meters depth. It shows mean (positive) velocities up to 35 cm.s^{-1} (e.g., at S20) before decreasing in the subsurface layer. Below 100 m depth, a flow northwestward is observed on T4 and rapidly becomes unstable (e.g., at S21). In this layer, there is a reversal of direction and low flow velocities (< 15 cm.s^{-1}) towards the depths. For OUT-ITs T5 transect (e.g., at S24), a bidirectional flow is observed moving southeastward at the surface and northwestward in the subsurface layer with low (< 15 cm.s^{-1}) mean velocities (Fig. A2.g.2, Appendix).~~

3.2.3 Competitive processes to generate mixing

Our aim is to distinctly associate each mixing event with either tidal activity or time-averaged currents. To achieve this, we compare the vertical shear induced by the baroclinic tidal current ($S^{2''}$)with that induced by the baroclinic mean current ($\overline{S^{2'}}$). Practically, each estimated dissipation rate ε is analyzed in the context of (N2, $S^{2''}$) and ($\overline{S^{2'}}$, $S^{2''}$) spaces. The mixing hotspots are observed where vertical shear instability is prominent (Fig. 7, and Figs. A20 and A21, Appendix).

Along the transects (Fig. 7, and Figs. A20 and A21, Appendix), stronger mixing, with ε ranging between [10-7, 10-5] W kg-1, occurs at stations S6 and S10. At these locations, there is significant stratification (N^2 exceeding [10-5, 10-3] s-2), strong tidal shear ($S^{2''}$within [10-4, 10-3] s-2), and low gradient Richardson number (Ri < 0.25).

In contrast, at stations S7, S11, S13, and S14, mixing events with similar ε values are observed under comparable stratification conditions but with relatively weaker tidal shear and higher Ri (ranging from 0.25 to 1). Stations S12, S20, S21, and S24 show lower dissipation rates, reaching up to [10-8] W kg-1. These values are found in regions with significant stratification (N^2 exceeding 10-4 s-2) and Ri > 1.

This analysis reveals that vertical tidal shear is sufficiently strong at stations S6 and S10 to overcome stratification and generate hotspots of mixing. At stations S7, S11, S13, and S14, the tidal shear is comparatively weaker, and it is even less pronounced at S12, S20, S21, and S24, limiting its ability to cross stratification and generate mixing.

When comparing the influence of mean shear $\overline{S^{2'}}$ with mixing events, we observe that stronger $\overline{S^{2'}}$, within the range [10-5, 10-3] s-2, aligns with mixing hotspots characterized by dissipation rates between [10-8, 10-5] W kg-1 along the transects (e.g., at S7, S11, and S14). This suggests that the baroclinic mean shear also plays a significant role in driving mixing in the water column.

To better clarify which of the tidal vs mean vertical shear is dominating to explain the hotspots of mixing, we compare the contribution of $S^{2''}$ and $\overline{S^{2'}}$ to the total vertical shear (Table A1, Appendix).

Along transects Aa and Ab, tidal shear exhibits a stronger contribution relative to mean shear ($S^{2''}/\overline{S^{2'}}$) at specific shelf-break locations: (61.4/38.6 %) at S6, (65.8/34.2 %) at S10, and (58.5/41.5 %) at S21. This contribution decreases a few kilometers from these locations, with minimums observed at S7 (47.6 %) and S11 (48.2 %). Interestingly, along transect Aa, tidal shear contribution rises from 48.2 % at S11 to 58.5 % at S14 in the open ocean. Conversely, along transect E, it decreases from 58.5 % at S21 to 52.1 % at S20. Overall, tidal and mean shear contributions are nearly equal (~ 50/50 %) away from the shelf-break and along the OUT-ITs transect G (e.g., at S24), except at S14, where tidal shear remains dominant.

These contributions to the total shear instability support the hypothesis that mixing is dominated by ITs on the shelf-break, by both the mean circulation and ITs away from the shelf-break and far IT fields.

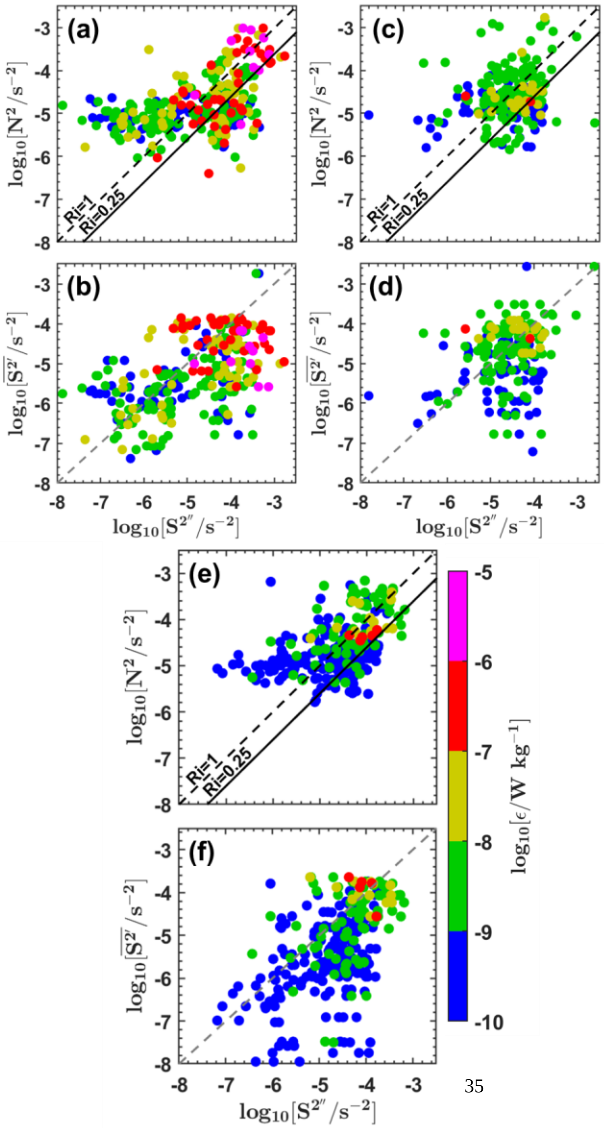

Formatted: Not Highlight

Formatted: Not Highlight

Figure 7: Dissipation rates (ε, in W kg-1, on a logarithmic scale) below the XLD as a function of the buoyancy frequency squared (N2, in s-2, on a logarithmic scale) and semi-diurnal baroclinic vertical shear squared ($S^{2''}$, in m s-1, on a logarithmic scale) for stations (a) S10, (c) S11, and (e) S14. Dissipation rates (ε, in W kg-1, on a logarithmic scale) below the XLD as a function of mean baroclinic vertical shear squared ($\overline{S^{2'}}$, in m s-1, on a logarithmic scale) and semi-diurnal baroclinic vertical shear squared ($S^{2''}$, in m s-1, on a logarithmic scale) for stations (b) S10, (d) S11, and (f) S14. N2 was linearly interpolated into the depths of □2” to have same vertical scales. Panels (a), (c), and (e) also display two solid black lines corresponding to Richardson number Ri = 0.25 and Ri = 1, respectively. Dashed grey lines in panels (b), (d), and (f) are included for comparison purposes.

~~Our intention is now to clearly associate each mixing event to either tides or mean currents. For that purpose we will compare for each mixing event the vertical shear induced by the baroclinic tidal current ($S^{2''}$) to those induced by the baroclinic mean current ($\overline{S^{2'}}$). Practically, each ε was analyzed in (N^2, $S^{2''}$) and ($\overline{S^{2'}}$, $S^{2''}$) space. The hotspots of ε are observed where there is important vertical shear instability. Indeed, along T1-T2 and T4 (Fig. 4a.3.2 to 4c.3.2, and Fig. A2.a.3.2 to A2.g.3.2, Appendix), strong mixing between [10^{-8},10^{-5}] W.kg-1 on the IN-ITs transects (e.g., at S6, S10, S14 and S21) are found where $S^{2''}$ is stronger (e.g., up to 1.4x 10^{-3} s^{-2} at S6, 1.2x 10^{-3} s^{-2} at S10 and 0.8x 10^{-3} s^{-2} at S14) than $\overline{S^{2'}}$. Tidal vertical shear was large enough to cross the large stratification (with N^2 up to 10^{-3} s^{-2} where Ri < 0.25) along T1 and T2 (Fig. 4a.3.1 to 4c.3.1, and Fig. A2.a.3.1 to A2.d.3.1, Appendix). This was not true (with Ri > 1) where there are more ε between [10^{-9},10^{-8}] W.kg^{-1} (e.g., at S20, S21 and S24) along T4 and T5 (Fig. A2.e.3.1 to A2.g.3.1, Appendix). Others mixing events within [10^{-9},10^{-6}] W.kg^{-1} were observed where $\overline{S^{2'}}$ is more relevant (up to 10^{-3} s^{-2}) than $S^{2''}$ or where there is low $S^{2''}$ shear (e.g., up to 0.4x10^{-3} s^{-2} at S21).~~

~~To better clarify which of the tidal vs mean vertical shear is dominating to explain the hotspots of mixing, we compare the contribution of the semi-diurnal (ε''_{MG}) and mean ($\bar{\varepsilon}'_{MG}$) baroclinic energy to the total baroclinic energy, by simply transforming the vertical shear into turbulent energy (Table A1, Appendix). On T1 and T2, the contribution of ε''_{MG} was found dominant (61.2 % at S6 and 65.94 % at S10) compared with that (38.8 % at S6 and 34.06 % at S10) of $\bar{\varepsilon}'_{MG}$ on the IT generation on the shelf-break. The same is true far from the shelf-break for some IN-ITs stations on T1 (e.g., at S12, S13 and S14) and on T4 (e.g., at S20 and S21). But this is not the case for other IN-ITs stations (e.g., at S7 and S11) where the contribution of ε''_{MG} suddenly drops, and for OUT-ITs stations (e.g., at S24) where the contribution (> 50 %) of $\bar{\varepsilon}'_{MG}$ dominates. However, the contribution of ε''_{MG} increases (from 51.85 % at S12 to 58.94 % at S14) along T1, while it decreases (from 59.13 % at S21 to 52.64 % at S20) along T4. The contribution to the baroclinic energy supports the hypothesis that mixing is dominated by ITs on the IT generation sites on the shelf-break, by mean circulation far IT fields, and both by ITs and background circulation away from the shelf-break.~~

Formatted: Not Highlight

Formatted: Not Highlight

Formatted: Not Highlight

Formatted: Not Highlight

Formatted: Not Highlight

Formatted: Not Highlight

Formatted: Not Highlight

Formatted: Font: Not Italic

3.2.4 IT ray tracing

An alternative approach to understanding the two primary processes driving the observed mixing is to examine the vertical profiles of the mean total currents (both along- and across-shore), with the spatial dimension along the transects of IT ray propagation. For this analysis, IT ray paths are computed for the M2 tidal frequency, with the rays for September illustrated along the ITs-IN transects (Aa, Ab, D, and E).

IT rays are generated at the critical slope, located between 32-104 km from the coast on the Amazon shelf-break (Fig. 8, and Figs. A6, A7, A22 and A23, Appendix). These rays propagate downward into the deep ocean, where they first reflect within a depth range of 1250-3900 m and at distances between 54-222 km. After bottom reflection and subsequent interaction with the pycnocline, the rays are expected to reflect seaward at the surface, typically at distances between 115-400 km. The curvature of the rays becomes more pronounced as they interact with the pycnocline, particularly between 20-207 m depth, defined by the upper (UTD) and lower (LTD) thermocline depths.

Along transects Aa and Ab (Fig. 8, and Figs. A6 and A22, Appendix), the total along-shore flow is stronger in the upper layer of 150 m, with velocities exceeding 80 cm s-1 (observed at S6, S7, S10, and S11). This flow becomes unstable between 150-185 km from the ray generation along transect Aa, and between 200-450 km and 500-1000 m depth along both transects Aa and Ab. In contrast, along transect E, the first 100 m depth reveals an opposing surface and subsurface along-shore flow at stations S20 and S21, with flow instability occurring between 120-500 m depth (Figs. A7 and A23, Appendix).

Tracking the IT rays along the transects (Fig. 8, and Figs. A6, A7, A22 and A23, Appendix), hotspots of mixing are identified where ray paths potentially interfere with each other or with the mean flow. They are observed at various depths, including the surface, between 70-180 m, and below 300 m along transects Aa (e.g., at S10, S12, S14) and Ab (e.g., at S6). Stronger mixing, ranging from [10-7 to 10-5] W kg-1, is observed near the ray generation site (e.g., at S5, S6, and S10), as well as along the ray paths (e.g., at S14) along transects Aa and Ab, compared to transect E.

These findings suggest that turbulent dissipation occurs along the IT ray paths, particularly where the rays interfere with one another and interact with the strong mean background circulation.

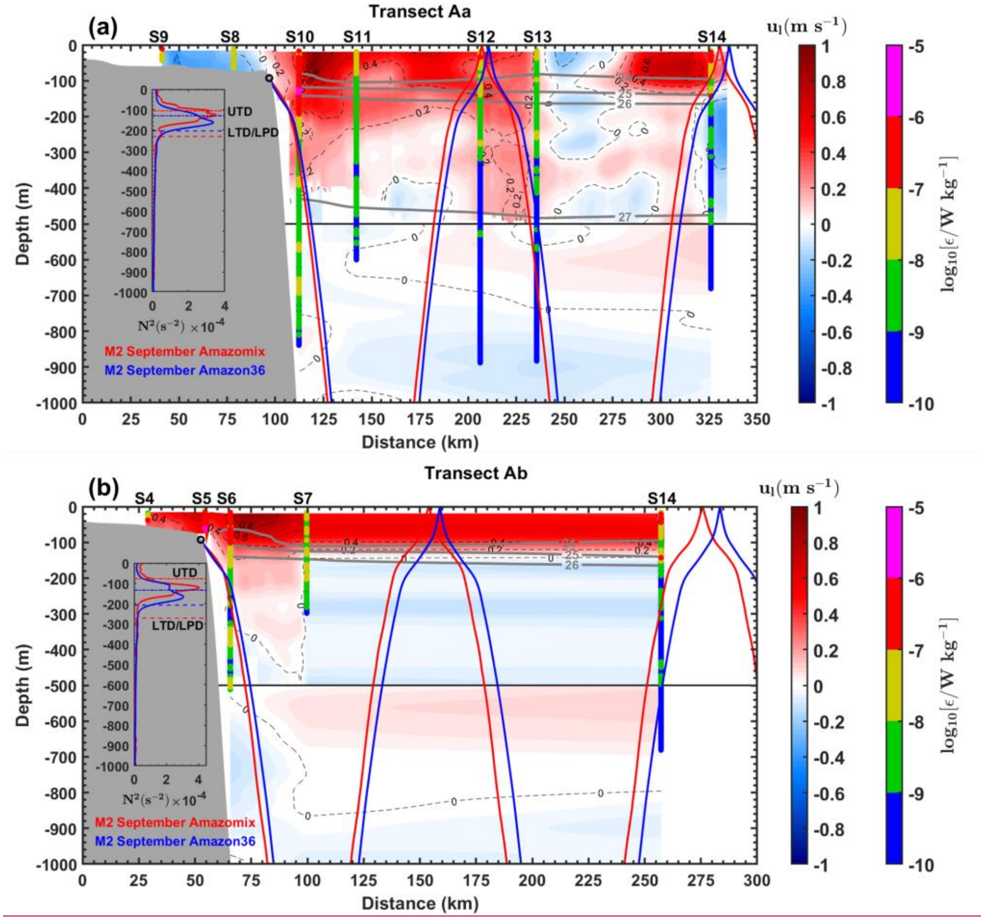

Figure 8: IT ray-tracing diagrams for the M2 tidal constituent along transects (a) Aa and (b) Ab. The calculations were performed using the mean buoyancy frequency squared (N2, in s-2) obtained from CTD-O2 data (ray in red) and NEMO-Amazon36 model data (ray in blue) for September. Grey areas represent local topography and black circles indicate the

Formatted: Right: 0,09 cm, Space After: 0,25 pt, Line spacing: Multiple 1,54 li *critical topography slope (ray generation sites). Panels (a) and (b) also show along the transects Aa and Ab: along-shore mean total currents (ul, in m s-1) from ADCP (Dashed black lines), potential density from CTD-O2 (grey contours), and dissipation rate profiles (ε, in W kg-1, on a logarithmic scale) from the VMP (vertical colored bars). Subpanels within each panel illustrate the N2 profiles from AMAZOMIX (red line) and the NEMO-Amazon36 model (blue line) used for ray-tracing calculations. Upper Thermocline Depth (UTD, dotted lines) and Lower Thermocline/Pycnocline Depth (LTD/LPD, dashed lines) are also indicated.*

Formatted: Font: Not Italic

~~Another way of looking at the two main processes that can explain the mixing measured is to look at the vertical profiles of the mean total (alongshore) currents, with the spatial dimension along the transect of IT rays propagation. IT ray paths are computed for the M2 tidal frequency and the rays for September are illustrated along the ITs-IN transects T1-T4 (Fig. 5a and 5b, and Fig. A3.a to A3.e, Appendix). IT rays are generated at the critical slope (between 32-104 km from the coast) on Amazon shelf-break, then propagate downward into the deep ocean where they reflect for the first time (within 1250-3900 m depth and at a distance between 54-222 km, not shown). After bottom reflection and eventual interaction with the pycnocline, IT ray paths were observed reflecting at the surface seaward at a distance of about 115-400 km (e.g., at T1-T4). The curvature of the IT rays is more pronounced when they reach the pycnocline depths delimited (between 93-207 m depth at T1-T4) by the upper (UTD) and lower (LTD) thermocline depth. Along T1 and T2 (Fig. 5a and 5b), alongshore flow towards northwest is found stronger at the surface with a maximum (negative) velocity up to 80 cm.s^{-1} (e.g., at S11) above 150 m depth. This flow becomes unstable beyond 150-450 m depth. A flow instability was also observed along T4 (Fig. A3.e, Appendix). Large ε are encountered where IT rays paths presumably interfere either between them or with the mean flow (Fig. 5a and 5b).~~

~~Tracking IT rays along the transects (Fig. 5a and 5b, and Fig. A3.a to A3.e, Appendix), ε are found larger (within [10^{-8},10^{-5}] W.kg^{-1}) in the rays generation (e.g., at S3, S5 and S10) and propagation (e.g., at S6 and S21). Some large ε are observed where IT rays radiated at the surface (e.g., at S12, S14 and S20) and below 300 m depth (at S14 along T1). These results indicate that turbulent dissipation occurred on the IT rays paths, and where rays interfere with each other and encounter the strong mean background circulation.~~

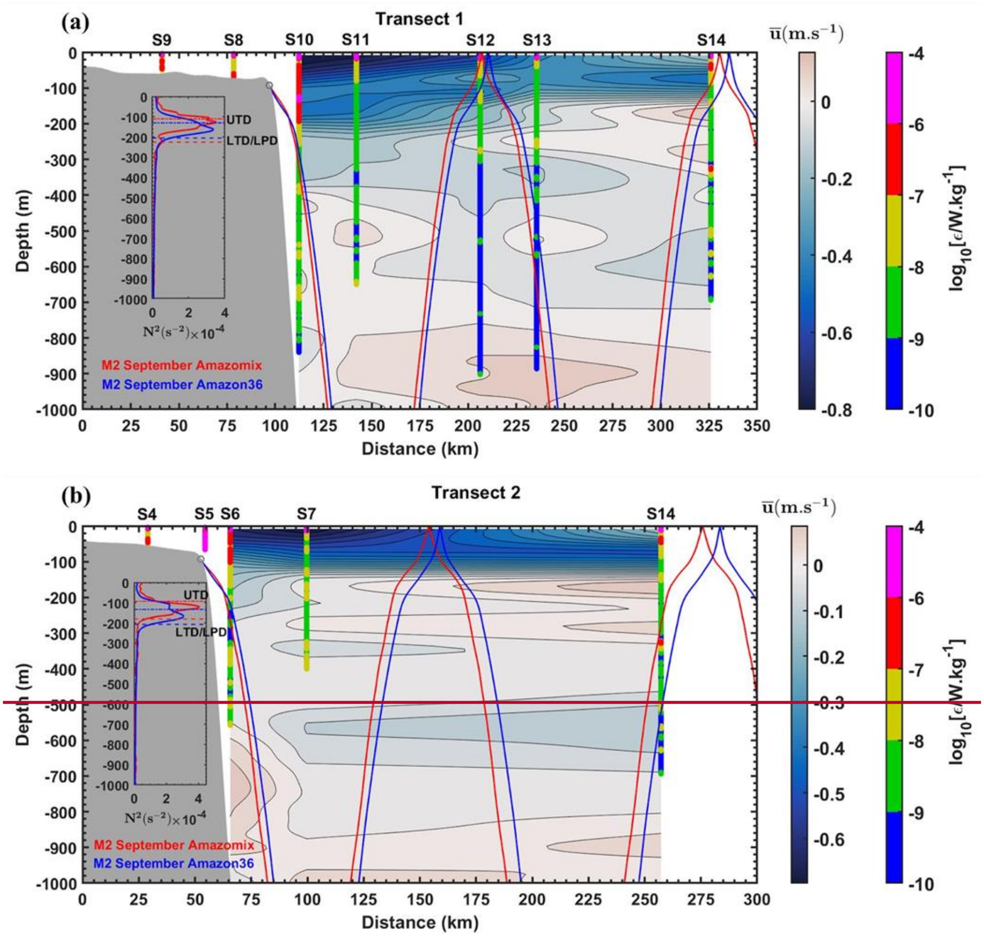

~~*Figure 5: Vertical sections showing: IT ray-tracing diagrams for the M2 tidal constituent assuming the mean (September) stratification (N^2 in s^{-2}, in overlaid panel) from AMAZOMIX CTD-O_2 (2021, in red line) and NEMO model (Amazon36, 2012-*~~

~~*2016, in blue line), along the transects (a) T1 and (b) T2. Overlaid on the panels the profiles of dissipation rates (ε in W.kg^{-1} on log scale, in coloured bars) from VMP, and the profiles of mean total (alongshore) current ($\bar{u}$ in m.s^{-1}, in background) for T1 and T2 from ADCP. UTD (in dotted lines) and LTD/LPD (in dashed lines) correspond to Upper and Lower Thermocline/Pycnocline Depth, respectively. Grey circles indicate the critical slope and grey areas represent local bathymetry.*~~

~~3.3 Vertical diffusivity and nutrients flux at the base of the mixed layer~~

~~The next steps of our study is dedicated to quantifying how much mixing could be responsible for nutrients uplift toward the euphotic layer, which may explains a boost in local primary production. Mixing coefficients were evaluated through vertical diffusivity (K_z). K_z is first analysed in the water column (Fig. A4, Appendix), and then at the base of MLD in Fig. 6c-e for T1 and T2 (and on Fig. A6.c and A6.d for T3 to T5, Appendix). For IN-ITs stations on T1-T4 (Fig. A4, Appendix), K_z is higher between [10^{-2}, 10^{-1}] m^2.s^{-1} in the mixed layers (e.g., at S10) and closer to the bottom layer. K_z is found smaller but still important below 200 m depth, with levels ranging between [10^{-4}, 10^{-3}] m^2.s^{-1}. For OUT-ITs stations on T5 (Fig. A4, Appendix), K_z remains stronger up to 10^{-4} m^2.s^{-1} below 200 m depth at S24, with two highest values exceeding 10^{-2} m^2.s^{-1} below XLD at S25. Finally, at the base of MLD, strong K_z is observed between [10^{-3}, 10^{-0}] m^2.s^{-1} on the Amazon shelf (e.g., at S5 and S9) and the generation sites (e.g., at S3, S6, and S10), as well as within [10^{-4}, 10^{-3}] m^2.s^{-1} along IT pathways. The question now is could it trigger a strong vertical flux of nutrients that may boost primary production? With simple consideration we calculate the vertical flux of nutrients (nitrate and phosphate) at the base of MLD. Nitrate flux is analyzed in Fig. 6a-b for T1 and T2 (and in Fig. A6.a and A6.b for T3 to T5, Appendix).~~

~~Nitrate fluxes at the base of MLD are higher within [10^{-2}, 10^{-0}] mmol N m^{-2}.s^{-1} between 30-95 m depth along T1-T3 (e.g., at S2, S3, S5-S7, and S9-S11), and smaller but still large within [10^{-3}, 10^{-2}] mmol N m^{-2}.s^{-1} around 60-120 m depth on T4 (e.g., at S19-S21). Other stations inside (e.g., S4, S12-S14) and outside (e.g., S24 and S25) of IT fields reveal nitrate fluxes even smaller approximately [10^{-5}, 10^{-3}] mmol N m^{-2}.s^{-1} at the base of MLD.~~

~~Also, phosphate fluxes (Fig. A5, Appendix) at the base of MLD are stronger between [10^{-3}, 10^{-1}] mmol P m^{-2}.s^{-1} around 30-95 m depth along T1-T3 (e.g., at S2, S3, S4, S5, S7 and S10), and smaller but still significant within [10^{-4}, 10^{-3}] mmol P m^{-2}.s^{-1} between 60-120 m depth on T4 (e.g., at S19-S21). Phosphate fluxes along T4 are still smaller about [10^{-6}, 10^{-4}] below the MLD and even exceeding 10^{-2} mmol P m^{-2}.s^{-1} above the MLD at S25. Finally, phosphate fluxes are essentially similar in shape as nitrate fluxes, which is relevant because they both depend mainly on K_z profiles (e.g., Fig. A6, Appendix). This indicates that significant vertical flux of nutrients was found where there was strong vertical diffusivity at the base of the mixed layers off the Amazon shelf.~~

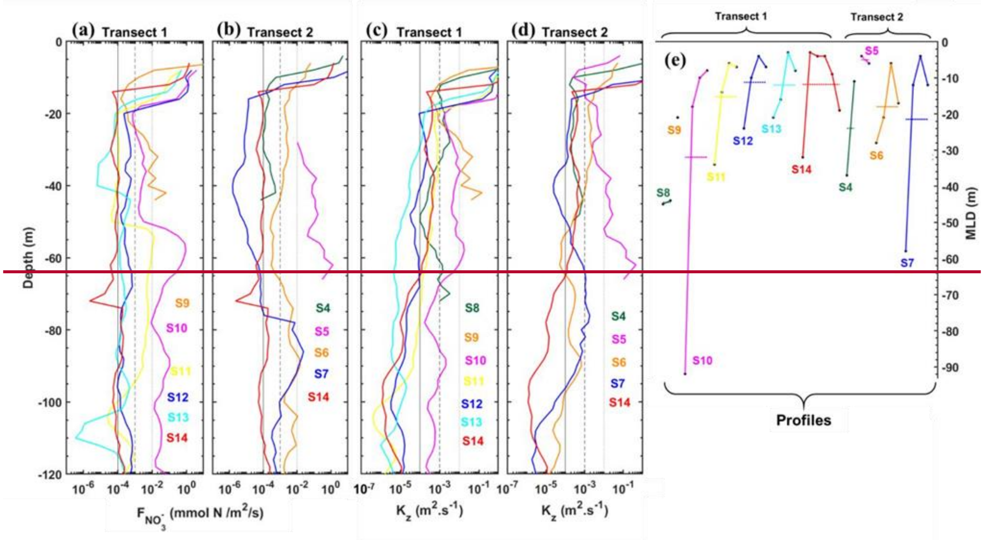

~~*Figure 6: (a)-(b) Vertical fluxes of nitrate (mmol N m^{-2}.s^{-1}) and (c)-(d) vertical diffusivity (in m^2.s^{-1}) at the base of MLD (defined at the MLD + 1m) during AMAZOMIX 2021 cruise for the transects/stations inside of the IT fields (a)-(c) T1 (S10-S14) and (b)-(d) T2 (S4-S7 and S14). Dashed and solid back lines are for comparison. (e) MLD (in m) for each CTD-O$_2$/LADCP (black dots), and average values (colored horizontal dashed lines) for each station. Colour is used to distinguish each station in each transect. Vertical flux of nitrate was null at S8 because of null nitrate concentration gradient.*~~

Formatted: Line spacing: Multiple 1,54 li

4 Discussion and Conclusion

The AMAZOMIX 2021 cruise provided, to the best of our knowledge, for the first time, direct measurements of turbulent dissipation using a velocity microstructure profiler (VMP) at multiple stations both inside and outside the influence of ITs. These measurements enabled the study of mixing processes at the Amazon Shelf break and the adjacent open ocean. To capture a full tidal cycle, data on turbulent dissipation rates, hydrography, and currents were collected alternately over 12 hours, with 4 to 5 profiles taken per station (see section 2). The locations of the 12-hour sampling stations were selected based on modeling results that provided realistic maps of IT generation and propagation (Fig. 1a; Tchilibou et al., 2022). Stations were located in the most energetic regions of IT, specifically at sites Aa, Ab, and D, covering stations S2 to S14, as identified in previous studies (Magalhaes et al., 2016; Tchilibou et al., 2022; Assene et al., 2024). Stations S19 to S21 were positioned in less energetic IT generation areas at site E, while stations S24 and S25 were located outside the influence of the IT fields (site G). Stations were distributed across different areas, including the shelf (e.g., S4, S9, and S19), the shelf-break (e.g., S3, S6, and S10), and the open ocean (e.g., S14, S24, and S20).

~~AMAZOMIX 2021 cruise delivered for the first time direct measurements of turbulent dissipation using a velocity microstructure profiler VMP over several stations in and out of the IT influence that allow to study mixing in the Amazon Shelf break and open ocean facing it. To catch a tidal cycle, the measurements of turbulent dissipation rate, hydrography and currents, and also nutrient concentrations were collected alternately during 12h with 4 to 5 profiles for each station (see section 2). The position of 12h stations were chosen using modeling results that provide realistic maps of ITs generation and propagation (Fig. 1a; Tchilibou et al., 2022). Stations within IT influence were localized on the most energetics IT generation regions in sites Aa, Ab and D (S6, S10 and S3) as referenced by previous studies (Magalhaes et al., 2016; Tchilibou et al., 2022; Assene et al., 2024) and along the IT propagation paths (S8-S9 and S11-S14 for site Ab). Also, a less energetic ITs site was sampled, in site F (at S20 located in the generation and S21 in the offshore). In addition, other stations were localized on the specific points (S5, S9 for sites Aa and Ab and S19 for site F) where IT beams may also climb the shelf-break just after generation. Finally, as for stations on the shelf-break, AMAZOMIX cruise also sampled regions out of the IT fields (S24) and in open ocean (S25).~~

Vertical Displacement, homogeneous layers

The results revealed that, over a semi-diurnal tidal cycle, relevant amplitudes of vertical displacements (up to 60 m in length) and pronounced step-like structures (up to 40 m thick) were observed along transects Aa and Ab. In contrast, smaller and thinner structures were identified along other transects, such as E. These differences are likely related to the propagation of ITs, which induce vertical displacements at tidal frequencies and promote mixing by creating homogeneous layers visible as step-like features in the density structure. The isopycnal displacements and step-like structures observed within the pycnocline are consistent with findings from other IT regions (e.g., Stansfield et al., 2001; Simpson and Sharples, 2012; Bordois, 2015; Koch-Larrouy et al., 2015; Zhao et al., 2016; Bouruet-Aubertot et al., 2018; Xu et al., 2020). Furthermore, IT propagation appears to have stronger energy along transects Aa and Ab compared to others, consistent with prior modeling studies (Tchilibou et al., 2022; Assene et al., 2024).

~~The results showed that over a semi-diurnal tidal cycle, both large (up to 60 m length) isopycnal displacements and strong (up to 40 m thick) step-like structures were found along the transects T1 and T2, whereas they are smaller and thinner on T3, T4 than T5. This is probably related to the propagation of ITs that produces vertical displacements at tidal frequency and~~

~~eventually mixing that creates homogeneous layers, identified on temperature and salinity structure as step-like features. We found stronger energy along T1 and T2, compared to T3 and T4, as previously described by modeling studies (Tchilibou et al., 2022; Assene et al., 2024). These step-like structures and isopycnal displacements in the pycnocline are also consistent with the observations over a tidal cycle in other IT regions (Stansfield et al., 2001; Simpson and Sharples, 2012; Bordois, 2015; Koch-Larrouy et al., 2015; Zhao et al., 2016; Bouruet-Aubertot et al., 2018; Xu et al., 2020).~~

Direct measurements of dissipation rate

Dissipation rates measured with the VMP ranged from between [10-10, 10-5] W kg-1 below the XLD, spanning from the continental shelf to the open ocean. The XLD was found to be considerably larger than the MLD at all stations, except at S8, S10, and S25. This is consistent with regions exhibiting strong subsurface shear, such as the equatorial ocean and western boundary current areas (Noh and Lee, 2008). The exception observed at other stations may reflect larger mixing events that were not captured by the VMP measurements.

The highest dissipation rates, within [10-6, 10-5] W kg-1, were observed primarily at generation sites Aa, Ab, and D (e.g., at stations S6, S10, and S3). Slightly lower but still substantial dissipation rates, ranging from 10-8 to 10-7 W kg-1, occurred a few kilometers (~40 km) from these generation sites (e.g., at S11 and S7), along IT pathways (e.g., at S12, S13, and S20), and even in regions farther from IT influence (e.g., at S24). Interestingly, dissipation rates were higher within [10-7, 10-6] W kg-1 in the open ocean, such as at station S14, located ~230 km from generation site Aa, as summarized in Fig. 9.

Similarly, the vertical eddy diffusivity coefficient, ranging from 10-3 to 10-1 m2 s-1, was highest at the shelf-break (at stations S3, S5, and S10), Away from the shelf-break, diffusivity values were lower but still substantial, within [10-4, 10^{-}3] m2 s-1 (e.g., at S2, S7, and S11).

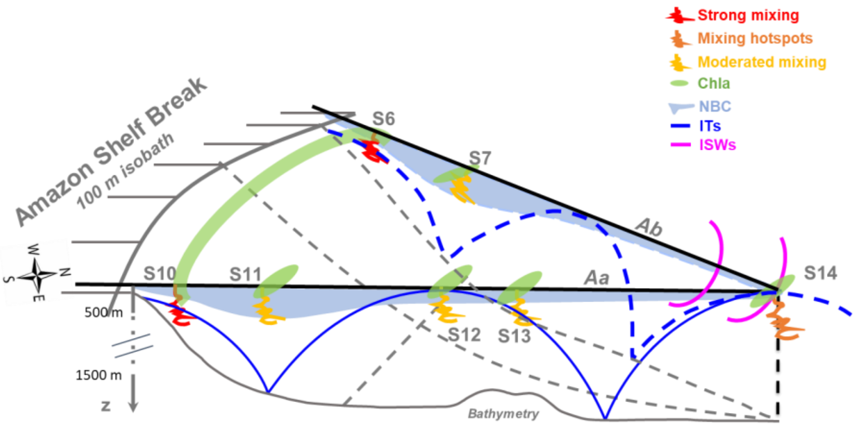

Figure 9: summary diagram illustrating the key processes driving mixing along the AMAZOMIX transects (e.g., Aa and Ab). At IT generation sites (e.g., S6 and S10; red zigzags), mixing rates are stronger, with ITs contributing around 65%, compared to mean circulation (NBC). Along IT pathways (e.g., S7 and S11; yellow zigzags), mixing decreases but remains notable, driven by nearly equal contributions from ITs and mean circulation. A key observation is the increased mixing ~ 230 km from two distinct IT generation sites at the shelf break. This hotspot at S14 (orange zigzags) coincides with the surfacing of IT rays (blue lines) from different sites, vanishing of the NBC (sky blue shaded areas) and the presence of ISWs (magenta lines), suggesting possible constructive interferences of IT rays may generate ISWs, amplifying mixing at S14. IT mixing observed close enough to the surface at these sites could influence the chlorophyll content (green shaded areas) off the Amazon shelf. ~~Dissipation rates, obtained with the VMP, were stronger within [10-6,10-4] W.kg-1 mainly on the generation sites Aa, Ab and D (at S6, S10 and S3) and were smaller but still large [10-9,10-7] W.kg-1 a few kilometers (~40 km) from these sites (at S2, S11 and S7), along the IT path (at S11-S13 and S20) and far IT fields (e.g., at S24). They were still higher between [10-8,10-6] W.kg-1 in the open ocean mainly ~225 km from generation site Ab (at S14), as resumed in Fig. 7.~~

Formatted: Font: Not Italic

Formatted: Not Superscript/ Subscript

Formatted: Not Superscript/ Subscript

Formatted: Not Superscript/ Subscript

Formatted: Not Superscript/ Subscript

Formatted: Not Superscript/ Subscript

Formatted: Not Superscript/ Subscript

Formatted: Not Superscript/ Subscript

Formatted: Not Superscript/ Subscript

Formatted: Not Superscript/ Subscript

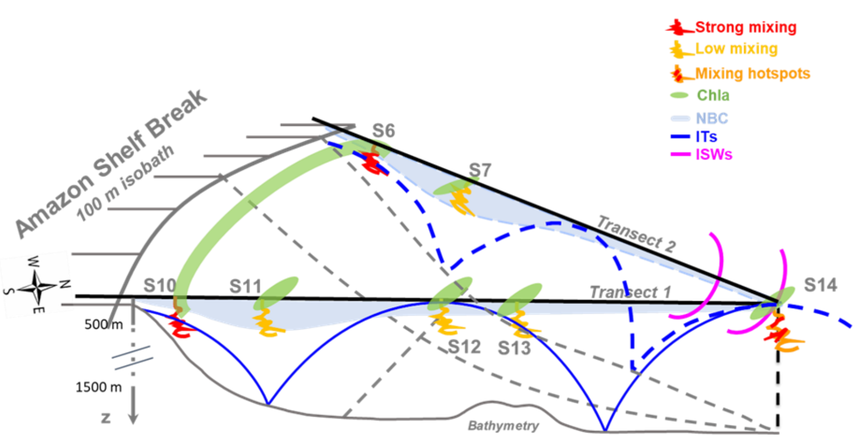

~~Figure 7: Summary diagram showing the processes that lead to mixing along the AMAZOMIX transects (e.g., along T1 and T2).~~

~~In comparison, in other regions, dissipation rates measured by similar VMP instrument are found between [10-7,10-5] W.kg-1 in the IT generation zone of Halmahera Sea, Indonesia (Koch-Larrouy et al., 2015; Bouruet-Aubertot et al., 2018), of Kaena Ridge, Hawaii (Klymak et al., 2008) and off the Changjiang Estuary (Yang et al. 2020). Whereas it is [10-10,10-8] W.kg-1 along the IT path in the Southern Ocean (Gille et al., 2012) and in Halmahera Sea (Bouruet-Aubertot et al., 2018). Direct estimates of dissipation far from IT influence are almost [10-11,10-10] W.kg-1 (Koch-Larrouy et al., 2015; Bouruet-Aubertot et al., 2018) or under the influence of geostrophic current (Takahashi and Hibiya, 2019).~~

~~Our study also found a very high dissipation rate for S3 and S5 of [10-6,10-4] W.kg-1 on the Amazon shelf , increasing near the bottom boundary layer. These findings compare well with values reaching 3x10-9 W.kg-1 within a kilometer of the seabed in the Southern Ocean (Sheen et al., 2013) and up to 10-6 W.kg-1 within a few meters from bottom topography off the Changjiang Estuary (Yang et al. 2020). This may indicate the presence of an active bottom boundary layer. Thus, kinetic energy of bottom flow was estimated using friction velocity, that was computed from total velocity averaged over the bottom-most 15 m for shallow stations. It showed bottom fiction energy stronger 9-22 J.m-2 at S3 and S5 mainly and lower (< 1 J.m-2) in the other stations (e.g., at S8) on shelf. These results are smaller but still important on the Amazon shelf and comparable to values (517 kJ.m-2) in the Drake Passage region (on the continental slope) of the Southern Ocean (Laurent et al., 2012). The bottom mixing at S3 and S5 can indirectly exert a control on pycnocline mixing on the Amazon shelf (Inall et al., 2021).~~

Formatted: Font: (Default) Times New Roman, 10 pt, Not Bold

Formatted: Font: Not Italic

Formatted: Not Superscript/ Subscript

Formatted: Not Superscript/ Subscript

Formatted: Not Superscript/ Subscript

Formatted: Not Superscript/ Subscript

Formatted: Not Superscript/ Subscript

Formatted: Not Superscript/ Subscript

Formatted: Not Superscript/ Subscript

Formatted: Not Superscript/ Subscript

Formatted: Not Superscript/ Subscript

Formatted: Not Superscript/ Subscript

Formatted: Not Superscript/ Subscript

Formatted: Not Superscript/ Subscript

Formatted: Not Superscript/ Subscript

Formatted: Not Superscript/ Subscript

Formatted: Not Superscript/ Subscript

Formatted: Not Superscript/ Subscript

Formatted: Not Superscript/ Subscript

Formatted: Not Superscript/ Subscript

Formatted: Not Superscript/ Subscript

In comparison, in other regions, dissipation rates measured by similar VMP instrument are found between [10-7, 10-5] W kg-1 in the IT generation zone of Halmahera Sea, Indonesia (Koch-Larrouy et al., 2015; Bouruet-Aubertot et al., 2018), of Kaena Ridge, Hawaii (Klymak et al., 2008) and off the Changjiang Estuary (Yang et al. 2020). Whereas it is [10-10,10-8] W.kg-1 along the IT path in the Southern Ocean (Gille et al., 2012) and in Halmahera Sea (Bouruet-Aubertot et al., 2018). Direct estimates of dissipation are almost [10-11, 10-10] W kg-1 far from IT influence (Koch-Larrouy et al., 2015; Bouruet-Aubertot et al., 2018) or under the influence of geostrophic current (Takahashi and Hibiya, 2019).

Our mixing coefficients are consistent with, the annual mean between [10-4, 10-3] m2 s-1 of Ffield and Gordon (1992) or Koch-Larrouy et al. (2007), and aligned with others previous studies using the microstructure data (e.g. Tian et al., 2009; Koch-Larrouy et al., 2015; Bouruet-Aubertot et al., 2018; Xu et al., 2020), or modeling results (e.g. Koch-Larrouy et al., 2007).

This crucial vertical eddy diffusivity close enough to the surface along the IT paths may play a role in modulating heat (e.g., Assene et al., 2024) and chlorophyll content (de Macedo et al., 2023; M'Hamdi et al., 2024; in preparation) observed off the Amazon shelf.

Our study also found the highest dissipation rates at stations S3 and S5 of [10-6,10-4] W kg-1 on the Amazon shelf , increasing near the bottom boundary layer. These findings compare well with values reaching up to 10-9 W kg-1 within a kilometer of the seabed in the Southern Ocean (Sheen et al., 2013) and up to 10-6 W kg-1 within a few meters from bottom topography off the Changjiang Estuary (Yang et al. 2020). This may indicate the presence of an active bottom boundary layer. Thus, kinetic energy of bottom flow was estimated using friction velocity, that was computed from total velocity averaged over the bottom-most 15 m for shallow stations. It showed bottom friction energy stronger between 16-35 J m-2 at S3 and S5 mainly and lower (< 3 J m-2) in the other stations on shelf (e.g., at S8). These results are smaller but still important on the Amazon shelf and comparable to values (517 kJ m-2) in the Drake Passage region (on the continental slope) of the Southern Ocean (Laurent et al., 2012). The bottom mixing at S3 and S5 can indirectly exert a control on pycnocline mixing on the Amazon shelf (Inall et al., 2021).

Enhanced surface mixing

The vertical eddy diffusivity coefficients were highest at the shelf break (e.g., at S3, S5, and S10), ranging from 10-3 to 10-0 m2 s-1. Away from the shelf break, diffusivity values were lower but remained substantial, within the range of 10-4 to 10-3 m2 s-1 (e.g., at S2, S7, and S11). These mixing coefficients align with values reported in other regions. For instance, vertical diffusivity falls within the range of 10-5 to 10-3 m2 s-1, as observed in the Luzon Strait (Tian et al., 2009), the Indonesian Sea (Koch-Larrouy et al., 2015; Bouruet-Aubertot et al., 2018), and the southern Yellow Sea (Xu et al., 2020).

Close to the surface, mixing coefficients remained significant, reaching up to 10-3 m2 s-1 between 100-200 m depth and up to 10-2 m2 s-1 above this layer at stations S6 and S10. These surface values are of the same order of magnitude as, but slightly higher than, those reported for the Halmahera Sea, Indonesia (Koch-Larrouy et al., 2015; Bouruet-Aubertot et al., 2018). In the open ocean, under the influence of ITs, mixing near the surface reached 10-4 m2 s-1 at S14.

This elevated vertical eddy diffusivity close enough to the surface along IT paths may play a critical role in modulating heat transfer (e.g., Assene et al., 2024) and chlorophyll distribution (see green shaded areas in Fig. 9) (de Macedo et al., 2023; M'Hamdi et al., in preparation) observed off the Amazon shelf, as documented in the Indonesian region (Nugroho et al. 2018; Koch-Larrouy et al., 2010; Sprintall et al., 2014; Zaron et al., 2023).

Contribution of Background circulation and ITs to mixing

Formatted: Font: Not Bold

Mean baroclinic current shear

Another important aspect addressed in this study was quantifying the contributions of different processes to the observed heterogeneous mixing.

First, the mean baroclinic current (BC) was considered as a proxy for the background circulation. The BC was predominantly structured into a northwestward surface flow and a southeastward subsurface flow along the IT pathways. The strong surface flow toward the northwest is associated with the North Brazil Current (NBC), which originates from the northeastern coast of Brazil (e.g., Bourlès et al., 1999) and propagates along the Amazon shelf-break (e.g., at stations S7, S10, S11, S14, and S24). Conversely, the southeastward subsurface flow observed at stations such as S7 and S11 might result from NBC instability or the presence of a countercurrent at depth (Dossa et al., 2024, in preparation). At site E, the flow reversal observed at S21 - characterized by a southeastward surface flow and a northwestward subsurface flow - was located inside of the outer path of the Amazon plume. This reversal could be related with the influence of AWL formed by continental inputs (Prestes et al., 2018).

Both baroclinic flows demonstrated a significant potential for shear instability, with vertical shear ranging from 10^{-5} to 10^{-3} s^{-2} off the Amazon shelf. The shear associated with the NBC was particularly pronounced around the pycnocline (between 40 and 200 m depth) at sites Aa, Ab, and G (e.g., at S6, S7, S10, S11, S14, and S24). At site E, the shear instability was stronger (> 2.5 x 10-4 s-2) at the base of the pycnocline (e.g., at S20), potentially associated with NBC retroflection near [5–6°N, 50°W] during the fall season (Didden and Schott, 1993). The higher BC shear observed at S21, where flow direction reversals occurred, could be associated with the presence of a subsurface cyclonic eddy (Dossa et al., 2024, in preparation).
~~Another important issue raised in this study was the quantification of the contribution of each process that could explain this heterogeneous mixing.~~

~~Firstly, we considered the mean baroclinic current (BC) as a proxy of the background circulation. BC was mainly structured in northwestward surface and southeastward subsurface flow. The strong surface flow (e.g., at S11) toward northwest is associated with NBC originating from the northeast coast of Brazil (e.g., Bourlès et al., 1999). The subsurface flow (e.g., at S11) toward southeast could be associated with the instability of the NBC in depth (Dossa et al., 2024; in preparation). Both baroclinic flows were unstable and produced vertical shear instabilities stronger >10-4 s-2 at 100-120 m for NBC and ~0.5 x 10-4 s-2 at 530-550 m for the subsurface flow at S7 and S11 mainly, while they were still larger (>10-4 s-2) above 80 m for NBC at S6, S12-S14.~~

~~Other large shear instability of the mean current > 2.5 x 10-4 s-2, located in NBC pattern at S20 could be associated with NBC retroflection around 5-6°N during fall near 50°W (Didden and Schott, 1993). Finally, BC shear was ~0.8 x 10-4 s-2 between 100-120 m at S21 and 40-60 m at S24 out the IT fields, and inside of the outer path of the Amazon plume. It is probably related to the AWL from the continental inputs (Prestes et al., 2018) at S21 and S24, or due to the possible presence of subsurface eddy at S21. This shows the potential of the mean flow to develop shear instability off the Amazon shelf.~~

ITs shear

Second, the baroclinic tidal current was extracted from the total baroclinic current, revealing significant semi-diurnal (M2) component signals around the pycnocline. These signals, characterized by higher tidal modes (3-5), were more pronounced at generation and propagation sites Aa and Ab (e.g., at S6, S10, and S14) compared to other sites. The tidal shear within the pycnocline layer (80-120 m) is consistent with the observed IT signal patterns and large vertical displacements. It was stronger, reaching up to 10^{-3} s^{-2}, near the generation sites Aa and Ab (at S6 and S10) and in the open ocean at S14. Further from the generation sites (e.g., at S7, S11, and S20), the IT shear was smaller but still notable (reaching up to 10-4 s-2). This highlights the significant role of ITs in driving mixing processes, particularly within the pycnocline, where strong vertical shears were observed near the shelf-break compared to regions far away. Outside the IT fields, such as at S24, the persistent high vertical shear near the bottom topography could be attributed to the active bottom boundary layer (Inall et al., 2021).

~~Second, regarding IT, the baroclinic tidal currents, were separated from the total baroclinic currents, and showed significant M2 semi-diurnal component signals, with high tidal modes 03-05 modes on the generations sites (S6 for Aa and S10 for Ab) and on the IT path coming from sites Ab in S14), with strong vertical shear instabilities associated to it. These high modes semi-diurnal baroclinic currents induced vertical tidal shears in the pycnocline layer (between 80-120 m). That was stronger between 1.5-2 x 10-3 s-2 in the generation areas (S6 and S10), still larger 1-1.5 x 10-3 s-2 a few kilometers from generation sites (S7 and S12) and smaller within 0.5-1 x 10-3 s-2 in the open ocean (e.g., at S20). Finally, for the stations out of the IT fields, IT shear was <10-3 s-2 at S24 in the water column, but higher than that close to the bottom topography probably due to the active bottom boundary layer (Inall et al., 2021).~~

Formatted: Not Superscript/ Subscript
Formatted: Not Superscript/ Subscript
Formatted: Not Superscript/ Subscript
Formatted: Not Superscript/ Subscript
Formatted: Not Superscript/ Subscript
Formatted: Not Superscript/ Subscript
Formatted: Not Superscript/ Subscript
Formatted: Not Superscript/ Subscript
Formatted: Not Superscript/ Subscript
Formatted: Not Superscript/ Subscript

Formatted: Not Superscript/ Subscript
Formatted: Not Superscript/ Subscript
Formatted: Not Superscript/ Subscript
Formatted: Not Superscript/ Subscript
Formatted: Not Superscript/ Subscript
Formatted: Not Superscript/ Subscript
Formatted: Not Superscript/ Subscript
Formatted: Not Superscript/ Subscript

IT/BC ratio

Both IT and BC shear contribute to mixing, with their relative dominance varying across sites. Near the generation sites on the shelf-break, IT shear dominated the IT/BC shear ratio, such as at S6 (61.4/38.6 %), S10 (65.8/34.2 %), and S21 (58.5/41.5 %). Along the IT paths, the contributions were nearly equal (~50/50 %) at locations farther from the generation sites (e.g., at S20, S7, S11, and S13), except at S14 in the open ocean, where IT shear remained dominant (58.5/41.5 %). These findings align with the presence of ITs at generation sites Aa, Ab, and E (Tchilibou et al., 2022; Assene et al., 2024) and the stronger energy associated with NBC cores, particularly at S7 and S11.

These results are consistent with previous studies that identified strong tidal shear near IT generation sites, such as the Halmahera Sea (Bouruet-Aubertot et al., 2018), the Changjiang Estuary (Yang et al., 2020), the northwest European continental shelf seas (Rippeth et al., 2005), and the southern Yellow Sea (Xu et al., 2020)..

The most relevant finding of this study was the relative increase in mixing within the pycnocline layer, observed at S14 in the open ocean, far from the IT generation sites.

~~Each of IT and BC shear contributes to mixing. The ratio changes from one site to another: in the vicinity of the ITs generation sites on the shelf-break, ITs dominated this ratio with ~65%/~35% for IT/BC respectively (for S10). Also, it was about ~60%/~40% at S14 where IT beams from Aa and Ab encounter and may interfere.~~

~~Whereas along the A path, where NBC was strong at S11-S12, it was ~50%/~50% and ~55%/~45% at S13. This relative diminution of IT influences compared to NBC may come from the fact that NBC was stronger at these stations.~~

~~Finally, for stations far from IT fields, BC dominated this ratio with ~49.6%/~50.4% at S24 due to both NBC and AWL.~~

~~These results are in good agreement with previous studies that showed strong tidal shear in the generation sites, such as in Halmahera Sea (Bouruet-Aubertot et al., 2018), off the Changjiang Estuary (Yang et al. 2020), in the northwest European continental shelf seas (Rippeth et al., 2005) or in the southern Yellow Sea (Xu et al., 2020).~~

~~The really new aspect raised in this study was the very large mixing found up to 225 km from generation sites, after the reflection beams in S14 (Fig. 4), induced by strong tidal shears between 1-1.5 x 10-3 s-2 located above (60-80 m) and within the pycnocline layer.~~

Formatted: Not Superscript/ Subscript

Discussion on the strong mixing at S14

Along the IT paths, elevated remote dissipation rates (within [10-7, 10-6] W kg-1) were identified ~ 230 km from the shelf-break at S14.

This region is well known for intense IT dissipation, as shown by a realistic model (Tchilibou et al., 2022; Assene et al., 2024), and for the highest occurrences of ISWs generated by ITs (Fig. 1a; de Macedo et al., 2023), with large-amplitude ISWs exceeding 100 m clearly visible in satellite records (Brandt et al., 2002).

At station S14, where relative mixing increases, IT rays surfacing from two distinct IT generation sites coincide with the appearance of ISWs and mark the location where the NBC vanishes.

This region of wave-wave interactions can lead to the constructive interference of IT rays, potentially facilitating the emergence of higher tidal modes (New & Pingree, 1992; Silva et al., 2015; Barbot et al., 2022; Solano et al., 2023). These higher modes, in turn, could enhance the generation of nonlinear ISWs (e.g., Jackson et al., 2012) and contribute to the elevated dissipation rates (Xie et al., 2013), as observed at this station.

Moreover, IT interactions with baroclinic eddies may also contribute to turbulent dissipation (Booth and Kamenkovich, 2008), particularly in this area of pronounced eddy activity. However, no repeated AMAZOMIX stations observed during a tidal period were enclosed by mesoscale eddy activity, except potentially around site E, where possible evidence of a subsurface eddy was detected at S21 (Dossa et al., 2024, in preparation).

Future studies are needed to unravel the intricate interplay among these processes. The data collected during the AMAZOMIX cruise will provide a guide for improving our understanding and advancing parameterizations for modeling studies.

~~Along IT paths, the higher remote dissipation rates (within [10-7, 10-6] W.kg-1) were found ~225 km from the shelf-break (S14). Indeed, S14 experiences stronger mixing than S12 and S13. This region has been described by realistic models as a region of strong dissipation of IT (Tchilibou et al., 2022; Assene et al. 2024). Also a recent satellite study, mapping ISWs generated from ITs using MODIS images, showed that this region is also the region of higher occurrences of ISWs (de Macedo et al., 2023). S14 is indeed localized where the ITs rays from Aa and Ab may intersect. It is also the region where the NBC vanishes. Such change in the wave guide as well as the wave-wave interferences may generate the higher modes found. These higher modes may in turn favor the generation of non-linear ISWs and higher dissipation rates found in this region. In addition, when ITs disintegrate into a package of ISWs events (Jackson et al., 2012) they can lead to enhancing turbulent mixing (Xie et al 2013).~~

~~It should be noted that ITs interactions with baroclinic eddies could also lead to the turbulent dissipation (Booth and Kamenkovich, 2008), in particular in this region of high eddy activities. However, no repeated AMAZOMIX stations investigated here over a tidal period were observed to be enclosed by mesoscale eddy activity off the Amazon shelf, except around S20-S21 where a possible subsurface eddy was detected.~~

~~Further study is necessary to better understand the complex interaction between all these processes, and AMAZOMIX data will serve as a guide for future understanding and parameterization for modeling study.~~

Formatted: Not Superscript/ Subscript

Formatted: Not Superscript/ Subscript

Formatted: Not Superscript/ Subscript

~~Role of mixing in nutrient fluxes off the Amazon shelf~~

Formatted: Font: Not Bold

~~One last important aspect that we investigate in this study, is the impact of mixing on nutrient fluxes at the base of MLD. Vertical fluxes of nitrate and phosphate were stronger around [10-2, 10 0] mmol N m-2.s-1 and [10-2, 10 0] mmol P m-2.s-1, respectively, mainly on the generation sites Ab and D (e.g., at S10 and S3; Figure 6) where the vertical diffusivity was stronger ([10-3, 10-1] m2.s-1). They were smaller but still large between [10-3, 10-2] mmol N m-2.s-1 and [10-4, 10-3] mmol P m-2.s-1 a few kilometers (~40 km) from these sites (at S11 and S7). The nitrate and phosphate fluxes were still smaller within [10-4, 10-3] mmol N m-2.s-1 and <10-4 mmol P m-2.s-1 along the IT path (at S12-S14 and S20) and far IT fields (e.g., at S24). Finally, they were even larger around [10-3, 10 0] mmol N m-2.s-1 and [10-3, 10 0] mmol P m-2.s-1 on the Amazon shelf (e.g., at S5) where the vertical diffusivity was stronger ([10-3, 10 0] m2.s-1).~~

Formatted ...

~~Such diffusivity is consistent with the estimates of Koch-Larrouy et al. (2015) in the Indonesian seas, that also measured an impact on nutrient fluxes and associated chlorophyll primary production (Zaron et al. 2023).~~

~~Tidal vertical diffusivity was also shown close enough to the surface to modify the heat content off the Amazon shelf (e.g., Assene et al. 2024). Due to the shallow euphotic zone in this region, the strong upward fluxes of nitrate and phosphate may contribute in the surface layer to the local chlorophyll bloom off the Amazon shelf. The significant impact of the latter was highlighted and shown: an increase in chlorophyll concentration (0.02-0.04 mg.m-3) using simple calculation, from glider and ocean color (M'Hamdi et al., 2024; in preparation), and from MODIS Terra sunglint images with and without ISWs events (de Macedo et al., 2023) off the Amazon shelf. The increase (1-2 orders of magnitude) in nutrient fluxes confirms the theory that mean supply of nutrients are often dominated by relevant IT mixing (Sharples and Zeldis, 2019; Kaneko et al., 2021; Yang et al., 2020). This finding implies that, in the AMAZOMIX region, ITs act as an important supplier of nutrient into the euphotic layer, able to maintain new primary production and to possibly impact the whole ecosystem.~~

Formatted: Not Superscript/ Subscript

Formatted: Font: 10 pt

Appendices

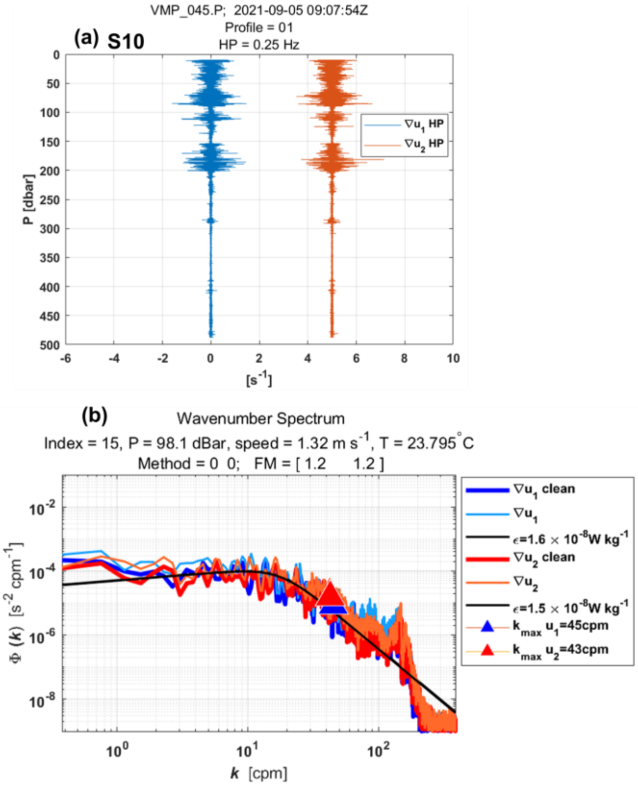

Figure A1: Example of wavenumber spectra from a dissipation structure segment recorded at station S10 at a pressure of 98.1 dBar. (a) Cleaned and high-pass filtered signals from shear probe 1 (blue) and shear probe 2 (red, offset by 5 s-1). (b) Wavenumber spectra for shear probes 1 and 2. Thick lines (blue for probe 1, red for probe 2) show shear spectra with coherent noise correction, while thin lines (sky blue for probe 1, orange for probe 2) show spectra without correction. Triangles mark the maximum wavenumber used for dissipation rate estimation. Black lines represent Nasmyth reference spectra for estimated dissipation rates of 1.6 x 10-8 W kg-1 (probe 1) and 1.5 x 10-8 W kg-1 (probe 2). Dissipation rate estimates for both shear probes at a pressure of 98.1 dBar yielded a figure of merit of 1.2.

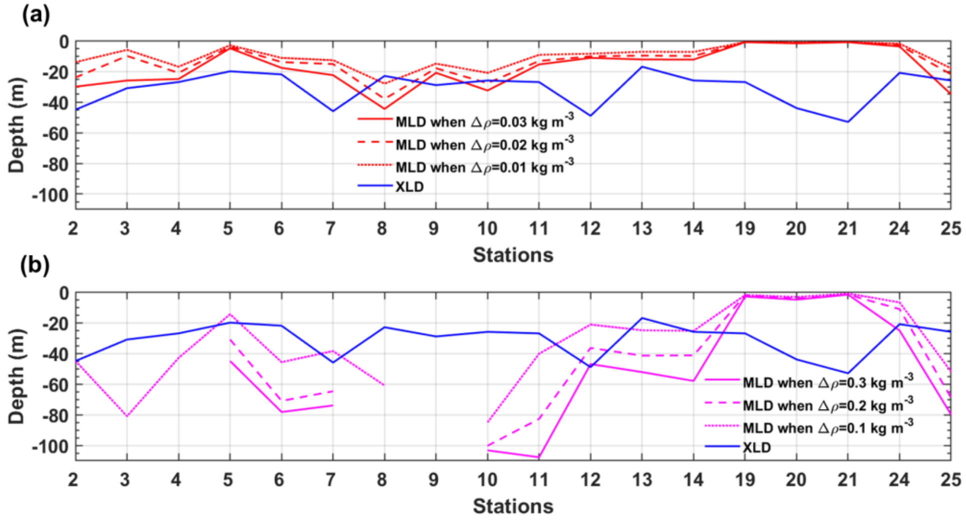

Figure A2: Comparison of Mixing Layer Depths (XLD, blue line) with Mixed Layer Depths (MLD) defined using (a) larger and (b) smaller density thresholds (Δ□). In panel (a), dotted, dashed, and solid red lines represent MLDs defined by Δ□ = 0.01, 0.02, 0.03 kg m-3, respectively. In panel (b), dotted, dashed, and solid magenta lines represent MLDs defined by Δ□ = 0.1, 0.2, 0.3 kg m-3, respectively.

Formatted: Font: Italic, Font color: Custom Color(RGB(17;17;17))

Formatted: Font: Italic, Font color: Custom Color(RGB(17;17;17))

Formatted: Font color: Custom Color(RGB(17;17;17)), Not Highlight

Formatted: Font color: Custom Color(RGB(17;17;17))

Formatted: Font: Italic, Font color: Custom Color(RGB(17;17;17))

Formatted: Font color: Custom Color(RGB(17;17;17))

Formatted: Font: Italic, Font color: Custom Color(RGB(17;17;17))

Formatted: Font: Italic, Font color: Custom Color(RGB(17;17;17)), Not Superscript/ Subscript

Formatted: Font: Italic, Font color: Custom Color(RGB(17;17;17))

Formatted: Font: Italic, Font color: Custom Color(RGB(17;17;17)), Not Superscript/ Subscript

Formatted: Font color: Custom Color(RGB(17;17;17))

Formatted: Font: Italic, Font color: Custom Color(RGB(17;17;17))

Formatted: Font: Italic, Font color: Custom Color(RGB(17;17;17)), Not Superscript/ Subscript

Formatted: Font: Italic, Font color: Custom Color(RGB(17;17;17))

Formatted: Font: Italic, Font color: Custom Color(RGB(17;17;17)), Not Superscript/ Subscript

Formatted: Font color: Custom Color(RGB(17;17;17))

Formatted: Font: Italic, Font color: Custom Color(RGB(17;17;17))

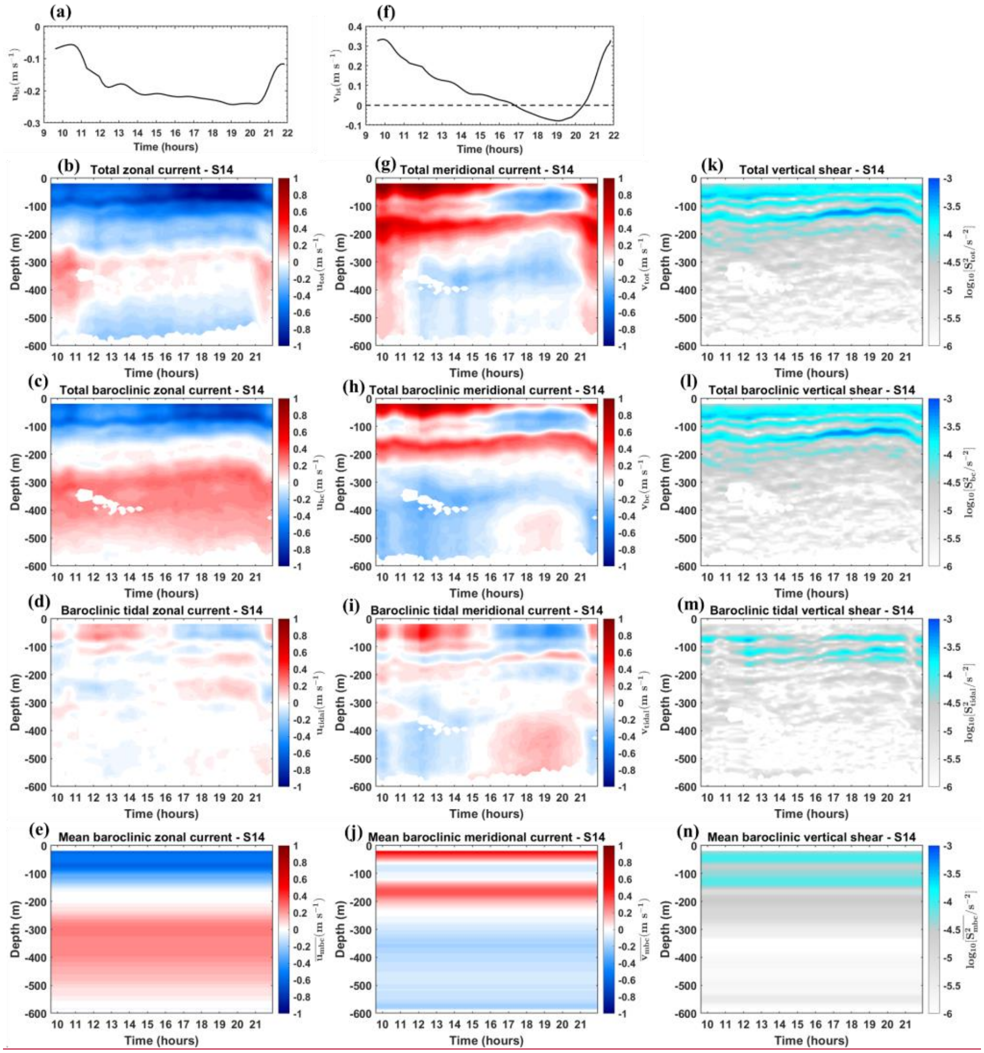
(a)
u_{bc} (m s^{-1})
Time (hours)
(f)
v_{bc} (m s^{-1})
Time (hours)
(b) Total zonal current - S14
(g) Total meridional current - S14
(k) Total vertical shear - S14
u_{tot} (m s^{-1})
v_{tot} (m s^{-1})
$\log_{10}[S^2_{tot}/s^{-2}]$
(c) Total baroclinic zonal current - S14
(h) Total baroclinic meridional current - S14
(l) Total baroclinic vertical shear - S14
u_{bc} (m s^{-1})
v_{bc} (m s^{-1})
$\log_{10}[S^2_{bc}/s^{-2}]$
(d) Baroclinic tidal zonal current - S14
(i) Baroclinic tidal meridional current - S14
(m) Baroclinic tidal vertical shear - S14
u_{tidal} (m s^{-1})
v_{tidal} (m s^{-1})
$\log_{10}[S^2_{tidal}/s^{-2}]$
(e) Mean baroclinic zonal current - S14
(j) Mean baroclinic meridional current - S14
(n) Mean baroclinic vertical shear - S14
$\overline{u_{mbc}}$ (m s^{-1})
$\overline{v_{mbc}}$ (m s^{-1})
$\log_{10}[\overline{S^2_{mbc}}/s^{-2}]$
Depth (m)
Time (hours)

Figure A3: For Station S14. zonal currents for (b) total, (a) barotropic, (c) total baroclinic, (d) semi-diurnal baroclinic tidal, and (e) mean baroclinic. Meridional currents for (g) total, (f) barotropic, (h) total baroclinic, (i) semi-diurnal baroclinic tidal, and (j) mean baroclinic. Vertical shear for (k) total, (l) total baroclinic, (m) semi-diurnal baroclinic tidal, and (n) mean baroclinic.

Formatted: Not Highlight

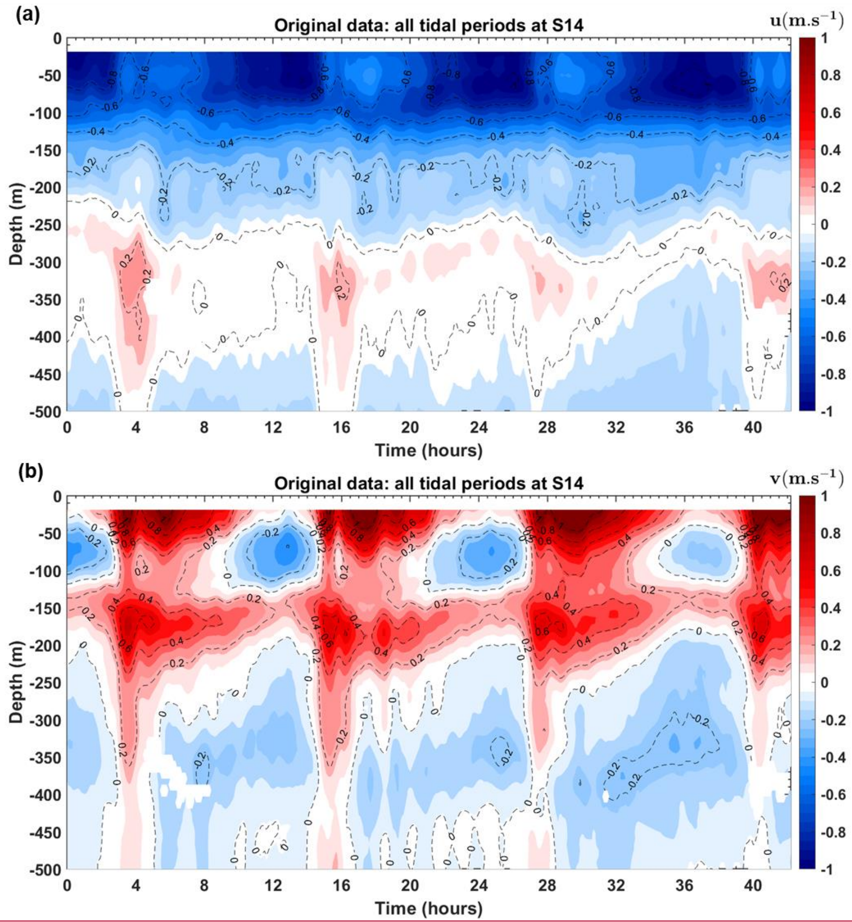

Figure A4: Time series of (a) total zonal and (b) meridional current from SADCP data at station S14. Time is scaled to start at t=0.

Formatted: Font: Italic, Font color: Custom Color(RGB(17;17;17))

Formatted: Font: Italic, Font color: Custom Color(RGB(17;17;17))

Formatted: Font color: Custom Color(RGB(17;17;17)), Not Highlight

Formatted: Font color: Custom Color(RGB(17;17;17))

Formatted: Font: Italic, Font color: Custom Color(RGB(17;17;17))

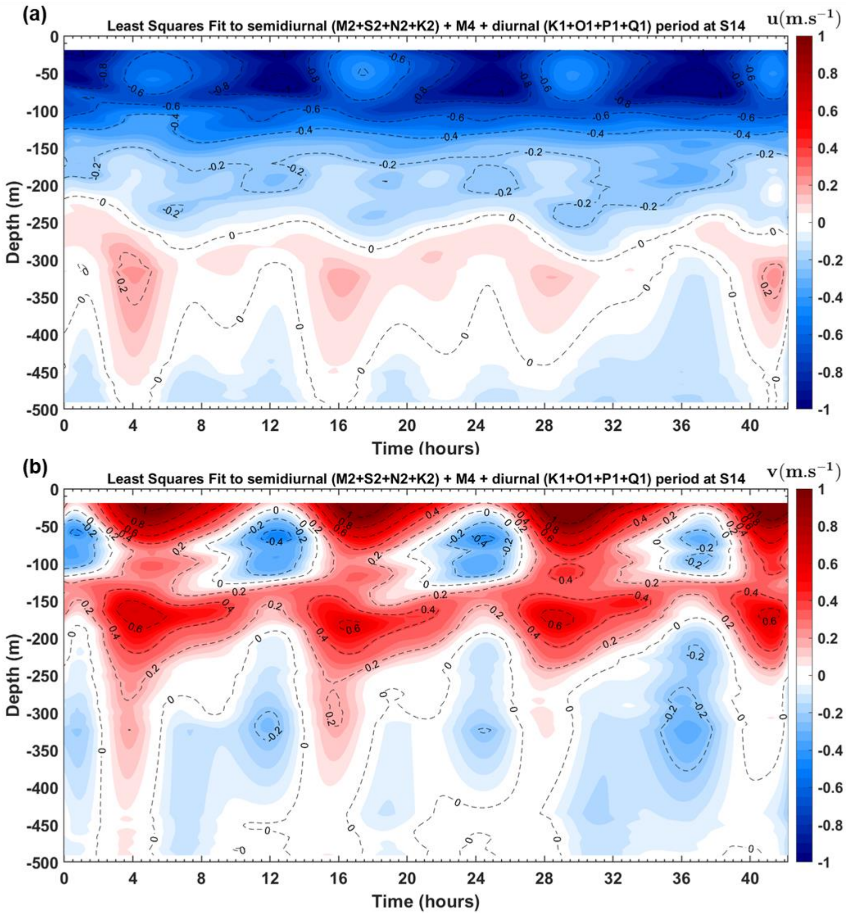

Figure A5: Least squares fit of sines and cosines to semidiurnal (M2+S2+N2+K2) + M4 + diurnal (K1+O1+P1+Q1) periods for total (a) zonal and (b) meridional current at station S14. Time is scaled to start at t=0.

Formatted: Font: (Default) Arial, 11 pt, Font color: Custom Color(RGB(70;70;70))

Formatted: Font: (Default) Arial, 11 pt, Not Italic, Font color: Custom Color(RGB(70;70;70)), Not Highlight

Formatted: Font: (Default) Arial, 11 pt, Font color: Custom Color(RGB(70;70;70))

Formatted: Font: (Default) Arial, 11 pt, Not Italic, Font color: Custom Color(RGB(70;70;70))

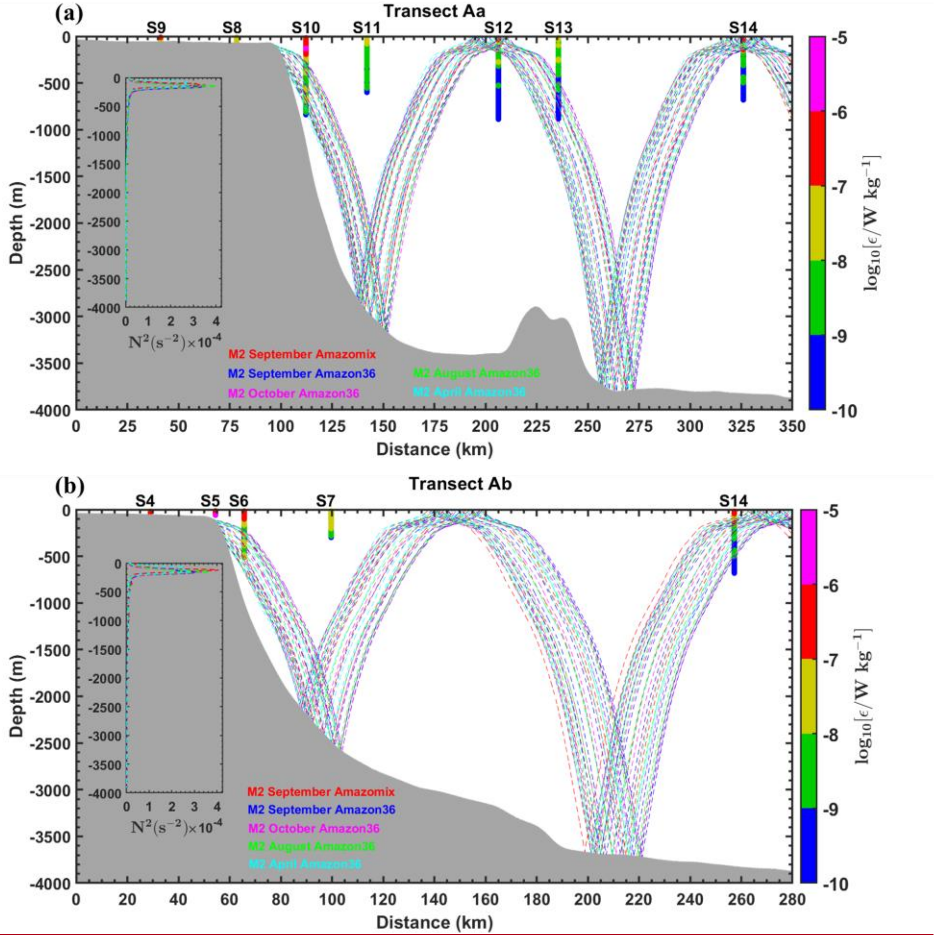

Figure A6: Sensitivity tests of M2 IT ray-tracing along the transects (a) Aa and (b) Ab, conducted by varying the location of the critical topography slope. The tests use mean buoyancy frequency squared (N2, in s-2) obtained from CTD-O2 data (September 2021) and NEMO-Amazon36 model data (2012-2016). Dashed colored lines represent IT beams calculated for

Formatted: Font: Not Italic, Not Highlight

Formatted: Font: Not Italic

Formatted: Font: Not Italic, Not Superscript/ Subscript

Formatted: Font: Not Italic

Formatted: Font: Not Italic, Not Superscript/ Subscript

Formatted: Font: Not Italic

Formatted: Font: Not Italic, Not Superscript/ Subscript

Formatted: Font: Not Italic

different seasons (April, August, October, and September) and for varying locations of the critical topography slope. Grey areas indicate local topography. Panels (a) and (b) also include dissipation rate profiles (ε, in W kg-1, shown as vertical colored bars on a logarithmic scale) from the VMP measurements. Subpanels within each panel illustrate the N2 profiles derived from AMAZOMIX and the NEMO-Amazon36 model, which were used in the ray-tracing calculations. For comparison, sensitivity tests using different N2 measurements from individual stations along the corresponding transect (e.g., at S10 and S14) revealed similar ray paths (not shown), consistent with the set of rays obtained using the mean N2.

Formatted: Font: Not Italic, Not Superscript/ Subscript

Formatted: Font: Not Italic

Formatted: Font: Not Italic, Not Superscript/ Subscript

Formatted: Font: Not Italic

Formatted: Font: Not Italic, Not Superscript/ Subscript

Formatted: Font: Not Italic

Formatted: Font: Not Italic, Not Superscript/ Subscript

Formatted: Font: Not Italic

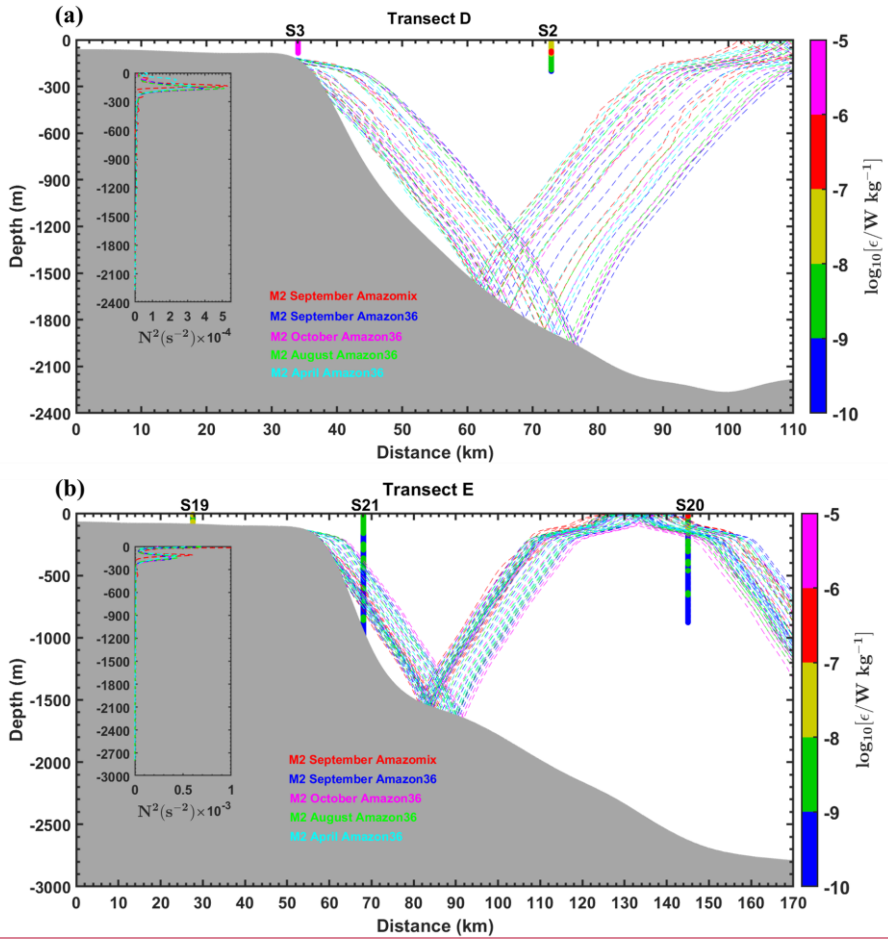

Figure A7: Panels are similar to Fig. A19 but for transects D and E.

Formatted: Font: Not Italic, Not Highlight

Formatted: Font: Not Italic

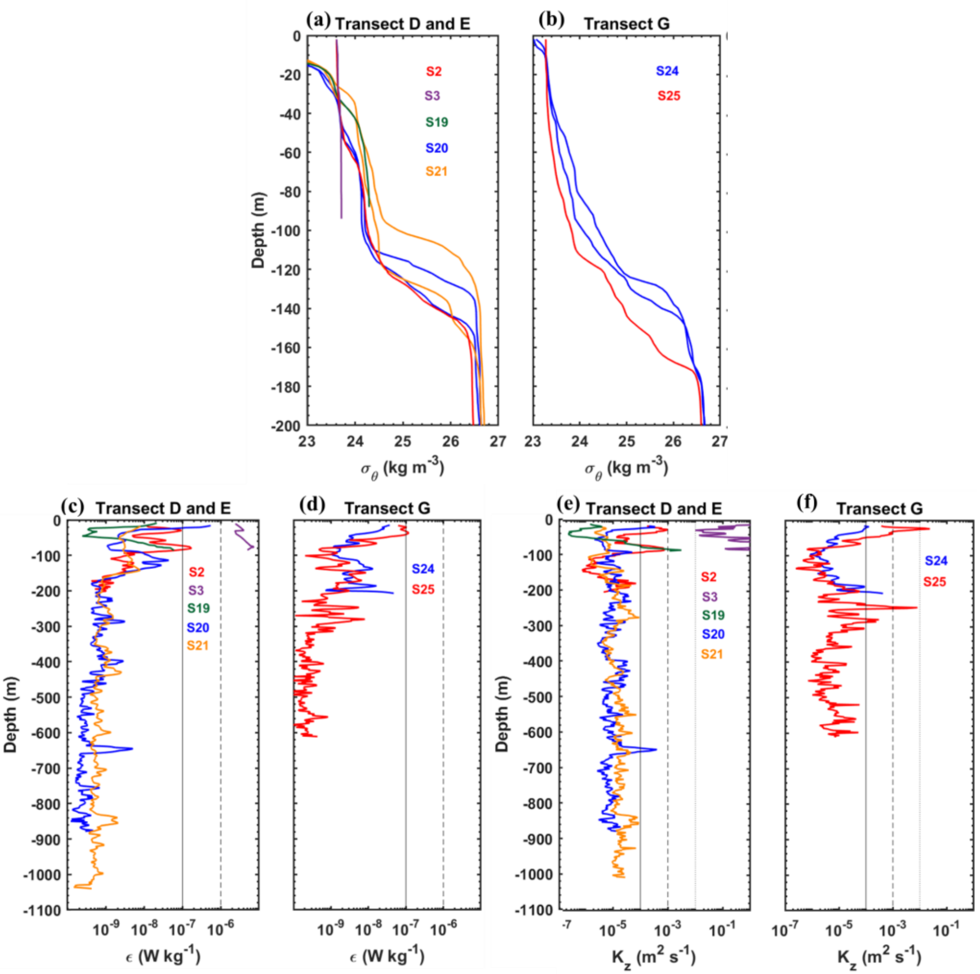

Formatted: Font: Bold, Italic

Formatted: Font: Bold, Italic

Figure A8: (a)-(b) Density profiles (σ_θ, kg m-3) obtained from CTD-O2 measurements during the AMAZOMIX 2021 cruise for stations (S2, S3, S19, S20, S21, S24, and S25) along transects D and E, and G, respectively. For long stations (S20, S21, and S25), two density profiles are shown to highlight step-like structures and isopycnal vertical displacements along the transects. The density values for station S3 range between 23.6 and 23.8 kg m-3. (c)-(d) Vertical dissipation profiles (ε, in W kg-1, on a logarithmic scale) from VMP and (e)-(f) vertical diffusivity profiles (Kz, in m2 s-1, on a logarithmic scale) for stations along transects D and E, and G, respectively. Distinct colors are used to represent each station within each transect. Dashed and solid black lines in panels (c) to (f) are included for comparison purposes.

Formatted: Font: Bold

Formatted: Font: Bold

Formatted: Font: Bold, Italic

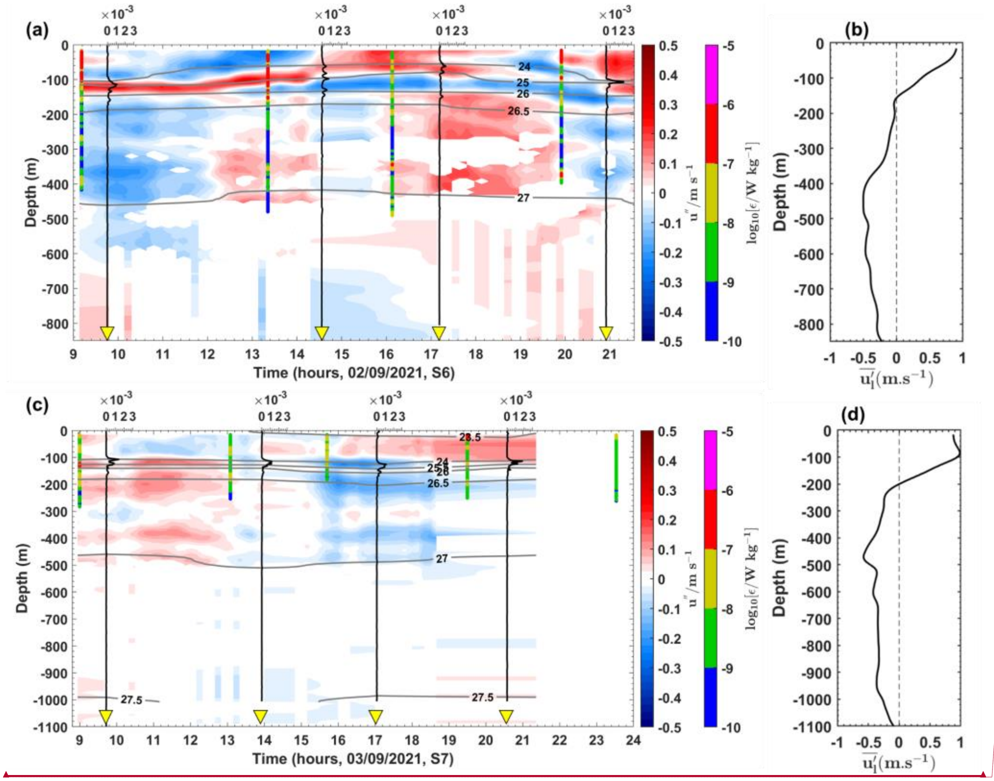

Formatted: Font: Bold, Italic

Formatted: Font: Bold, Italic

Figure A9: Semi-diurnal baroclinic zonal currents (u'', in m s-1) from the ADCP for stations (a) S6 and (c) S7. Panels (a) and (c) also display the buoyancy frequency squared (N2, in s-2) represented by vertical black lines, potential density represented by grey contours, and dissipation rate profiles (ε, in W kg-1, on a logarithmic scale) represented by vertical colored bars. Along-shore mean baroclinic currents ($\overline{u'}_l$, in m s-1) from the ADCP for stations (b) S6 and (d) S7.

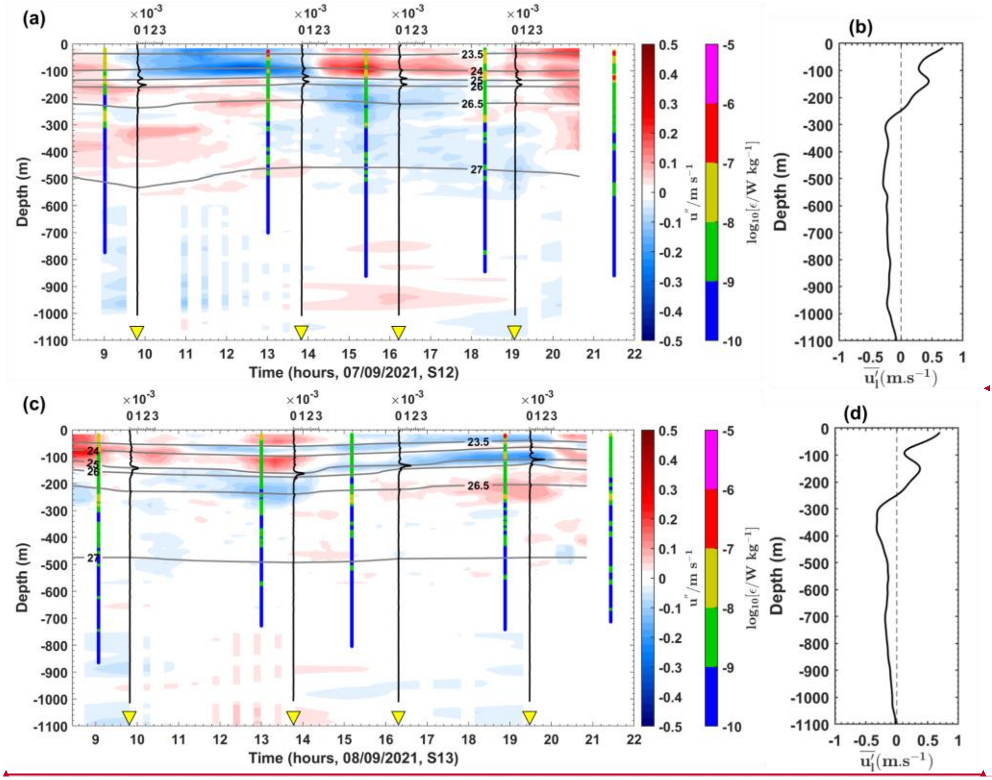

Formatted: Font: Bold, Italic

Formatted: Font: Bold, Italic

Formatted: Font: Bold, Italic

Formatted: Space After: 0,25 pt, Line spacing: Multiple 1,54 li

Formatted: Font: Bold, Italic

Figure A10: Panels are similar to Fig. A9 but for stations (a)-(b) S12 and (c)-(d) S13.

Formatted: Font: Bold

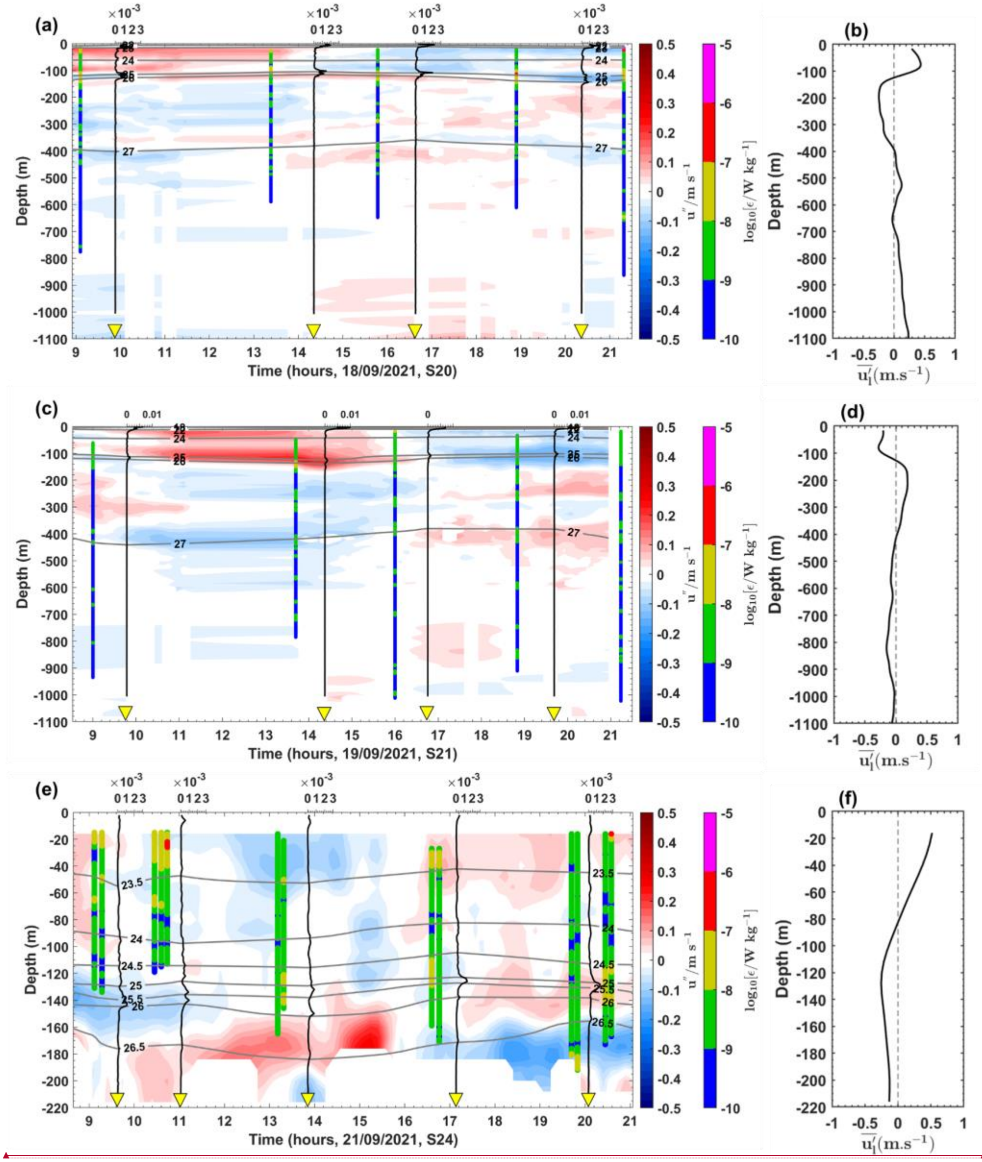

Formatted: Font: Not Italic

Formatted: Font: Not Italic

Figure A11: Panels are similar to Fig. A9 but for stations (a)-(b) S20, (c)-(d) S21, and (e)-(f) S24.

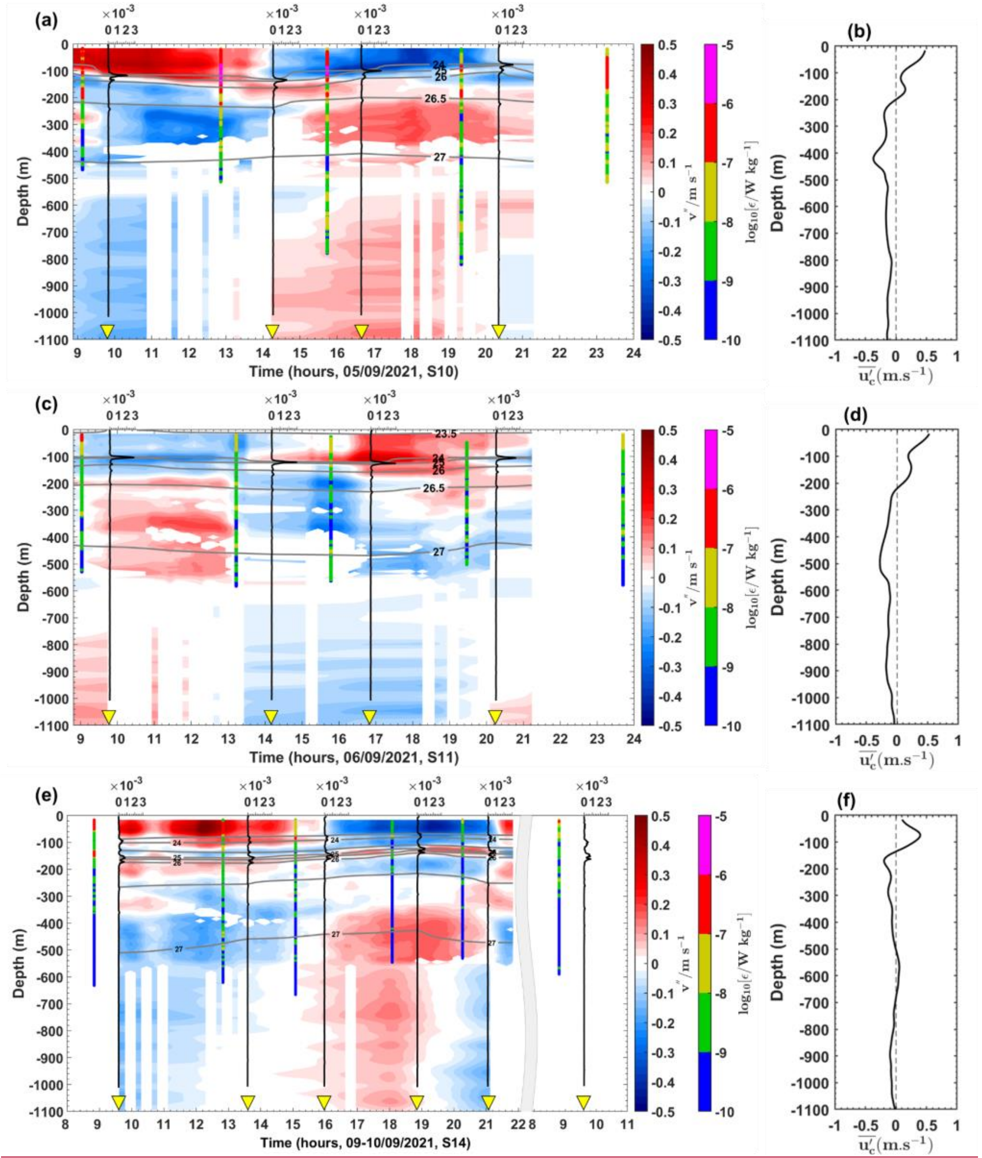
(a)
(b)
(c)
(d)
(e)
(f)
×10⁻³
0123
24
25
26
26.5
27
23.5
Depth (m)
Time (hours, 05/09/2021, S10)
Time (hours, 06/09/2021, S11)
Time (hours, 09-10/09/2021, S14)
v″/m s⁻¹
log₁₀[ε/W kg⁻¹]
u′c (m.s⁻¹)
0
-100
-200
-300
-400
-500
-600
-700
-800
-900
-1000
-1100
0.5
0.4
0.3
0.2
0.1
-0.1
-0.2
-0.3
-0.4
-0.5
-5
-6
-7
-8
-9
-10
-1
-0.5
0.5
1

Figure A12: Semi-diurnal baroclinic meridional currents (u'', in m s-1) from the ADCP for stations (a) S10, (c) S11, and (e) S14. Panels (a), (c), and (e) also display the buoyancy frequency squared (N2, in s-2) represented by vertical black lines, potential density represented by grey contours, and dissipation rate profiles (ε, in W kg-1, on a logarithmic scale) represented by vertical colored bars. Cross-shore mean baroclinic currents ($\overline{u'_c}$, in m s-1) from the ADCP for stations (b) S10, (d) S11, and (f) S14.

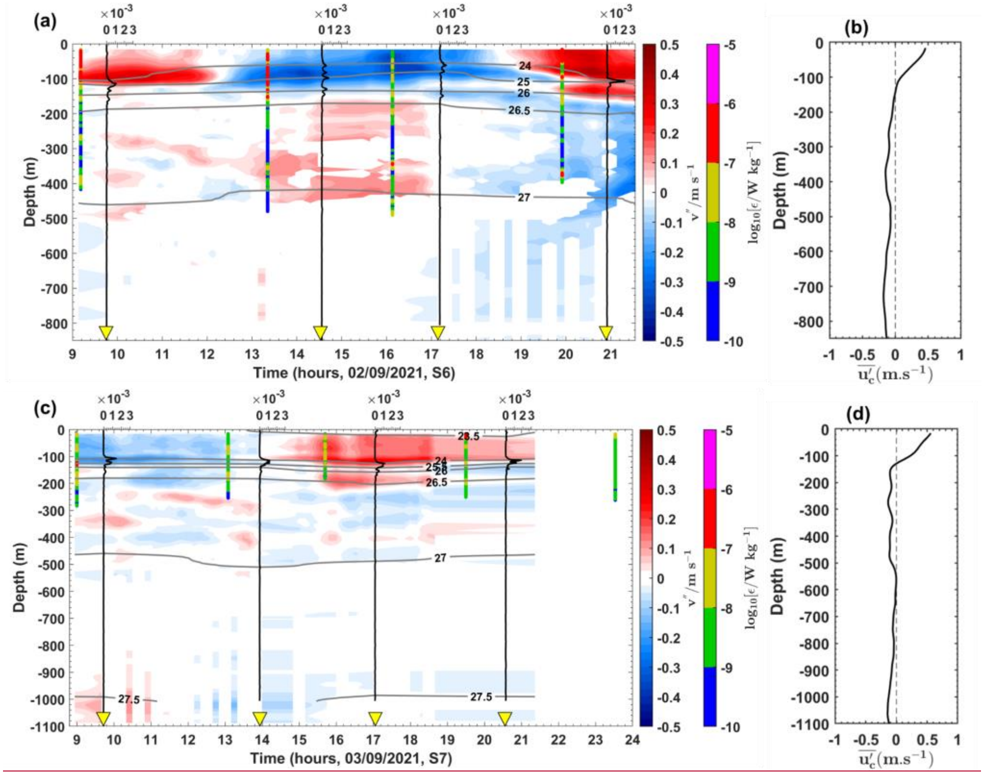

Figure A13: Panels are similar to Fig. A12 but for stations (a)-(b) S6 and (c)-(d) S7.

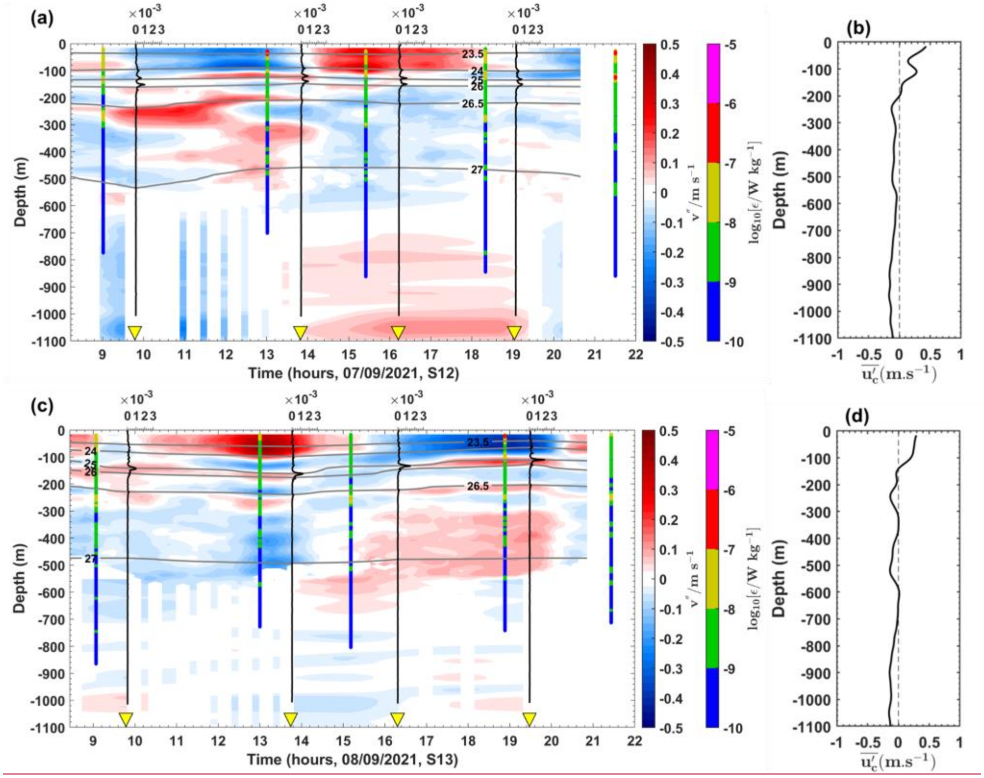

Figure A14: Panels are similar to Fig. A12 but for stations (a)-(b) S12 and (c)-(d) S13.

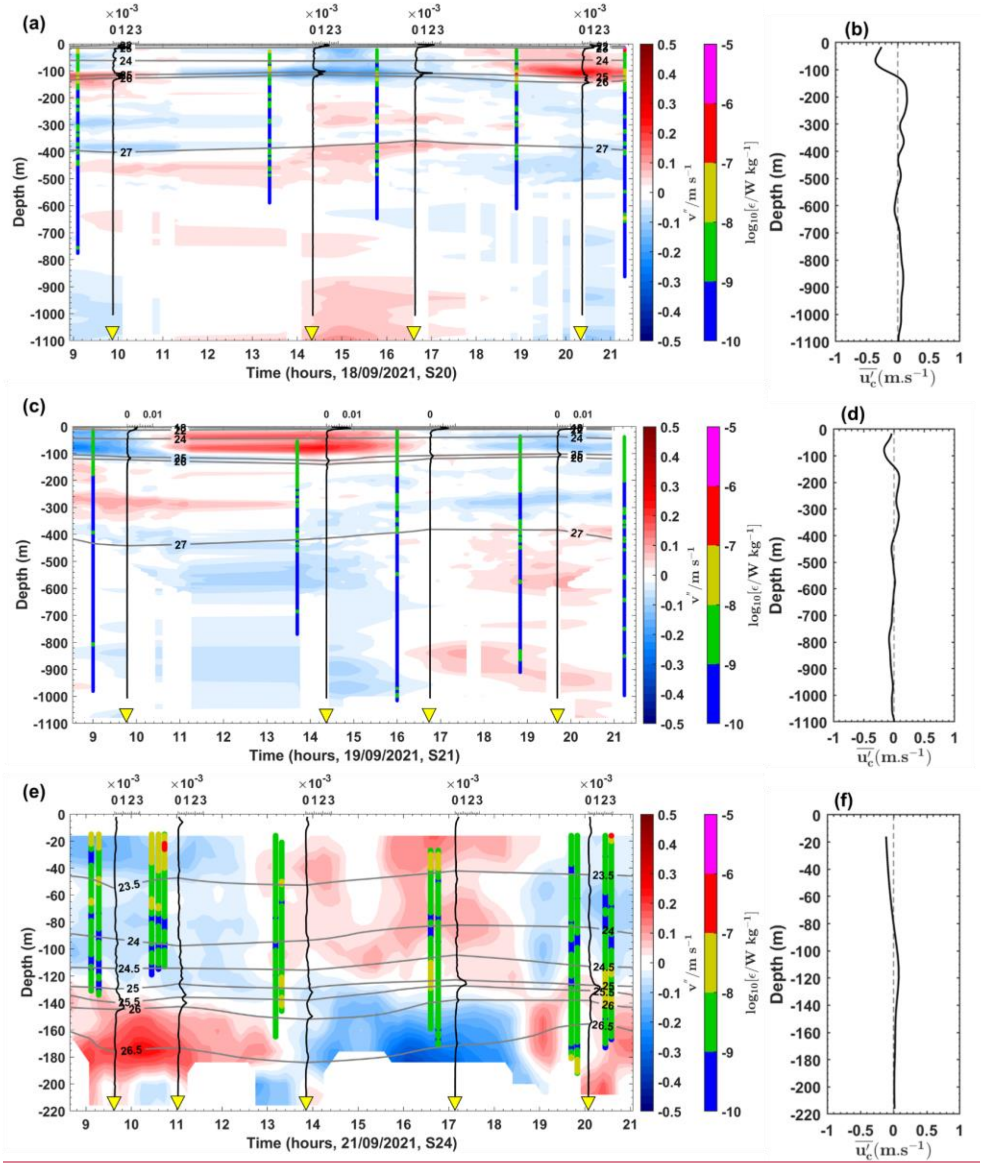
(a)
(b)
(c)
(d)
(e)
(f)
Depth (m)
Time (hours, 18/09/2021, S20)
Time (hours, 19/09/2021, S21)
Time (hours, 21/09/2021, S24)
$v''/\mathrm{m\,s^{-1}}$
$\log_{10}[\epsilon/\mathrm{W\,kg^{-1}}]$
$\overline{u'_c}(\mathrm{m.s^{-1}})$
$\times10^{-3}$
0123
0
0.01
23.5
24
24.5
25
25.5
26
26.5
27
0.5
0.4
0.3
0.2
0.1
0
-0.1
-0.2
-0.3
-0.4
-0.5
-5
-6
-7
-8
-9
-10

Figure A15: Panels are similar to Fig. A12 but for stations (a)-(b) S20, (c)-(d) S21, and (e)-(f) S24.

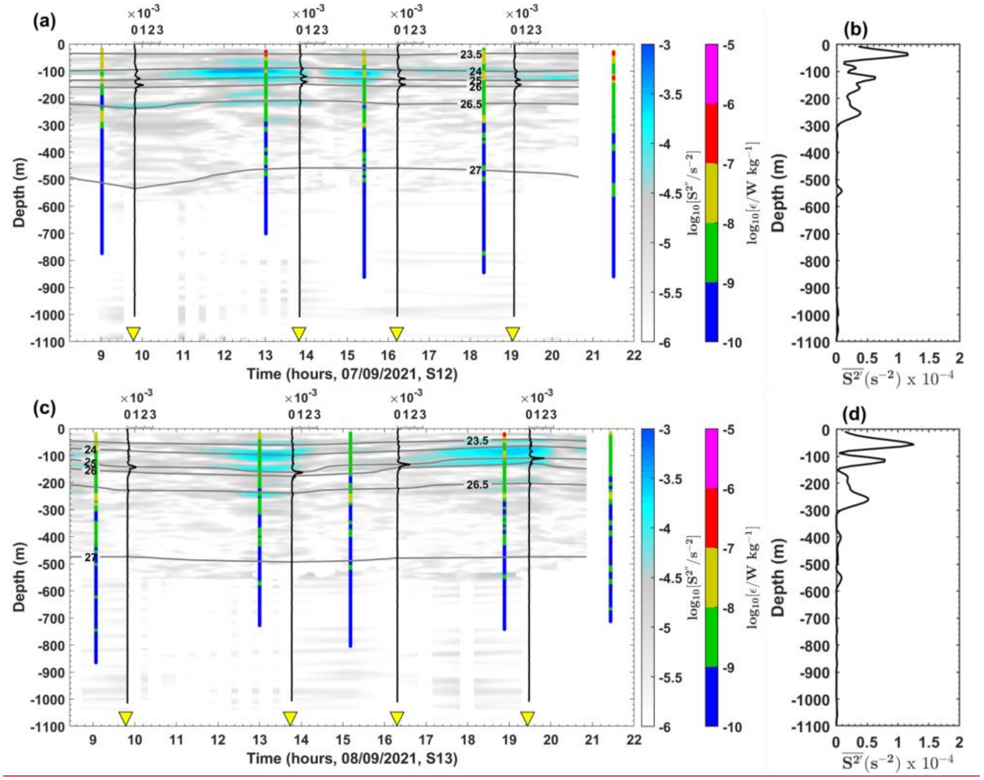

Figure A16: Semi-diurnal baroclinic vertical shear squared ($S^{2''}$, in m s-1, on a logarithmic scale) for stations (a) S6 and (c) S7. Panels (a) and (c) also display the buoyancy frequency squared (N2, in s-2) represented by vertical black lines, potential density represented by grey contours, and dissipation rate profiles (ε, in W kg-1, on a logarithmic scale) represented by vertical colored bars. Mean baroclinic vertical shear squared ($\overline{S^{2'}}$, in m s-1) for stations (b) S6 and (d) S7.

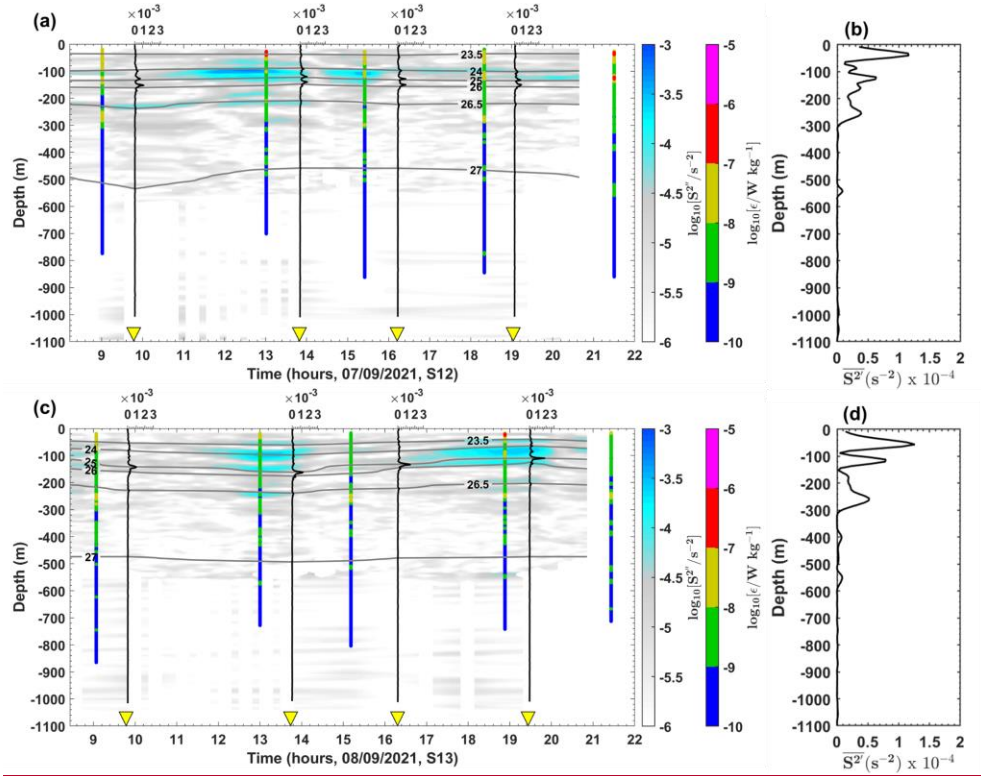

Figure A17: Panels are similar to Fig. A16 but for stations (a)-(b) S12 and (c)-(d) S13.

Formatted: Font: Italic

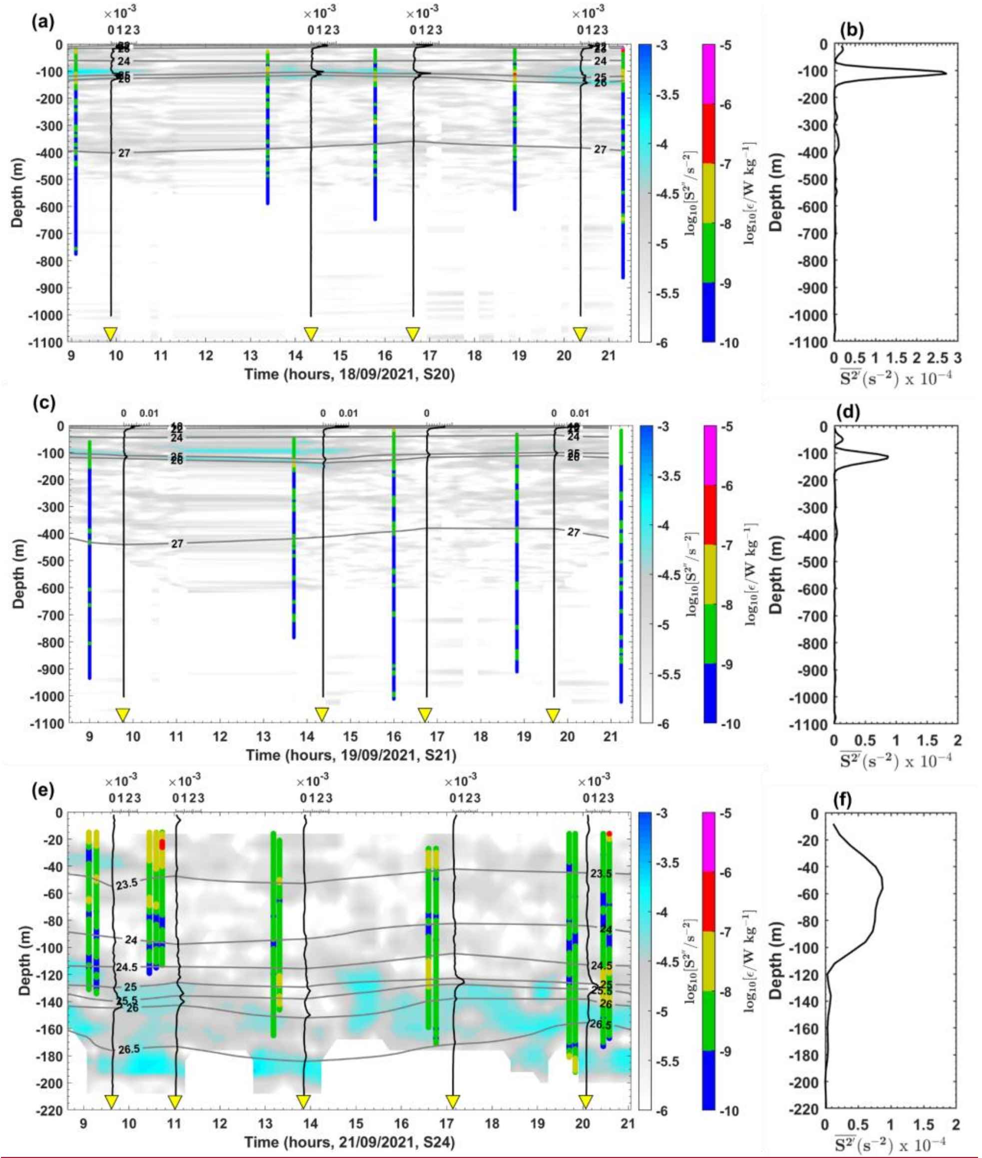
(a)
(b)
(c)
(d)
(e)
(f)
×10^-3
0123
0 0.01
Depth (m)
Time (hours, 18/09/2021, S20)
Time (hours, 19/09/2021, S21)
Time (hours, 21/09/2021, S24)
log10[S^2'/s^-2]
log10[ε/W kg^-1]
S^2' (s^-2) x 10^-4
23.5
24
24.5
25
25.5
26
26.5
27

Figure A18: Panels are similar to Fig. A16 but for stations (a)-(b) S20, (c)-(d) S21, and (e)-(f) S24.

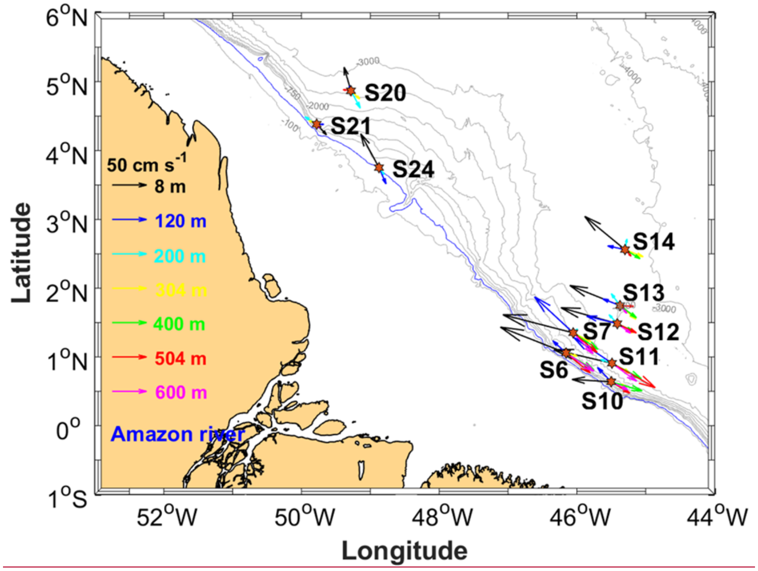

Figure A19: Map of mean baroclinic currents (vectors) at stations, with colored arrows representing currents at different depths. The blue line indicates the 200 m isobath.

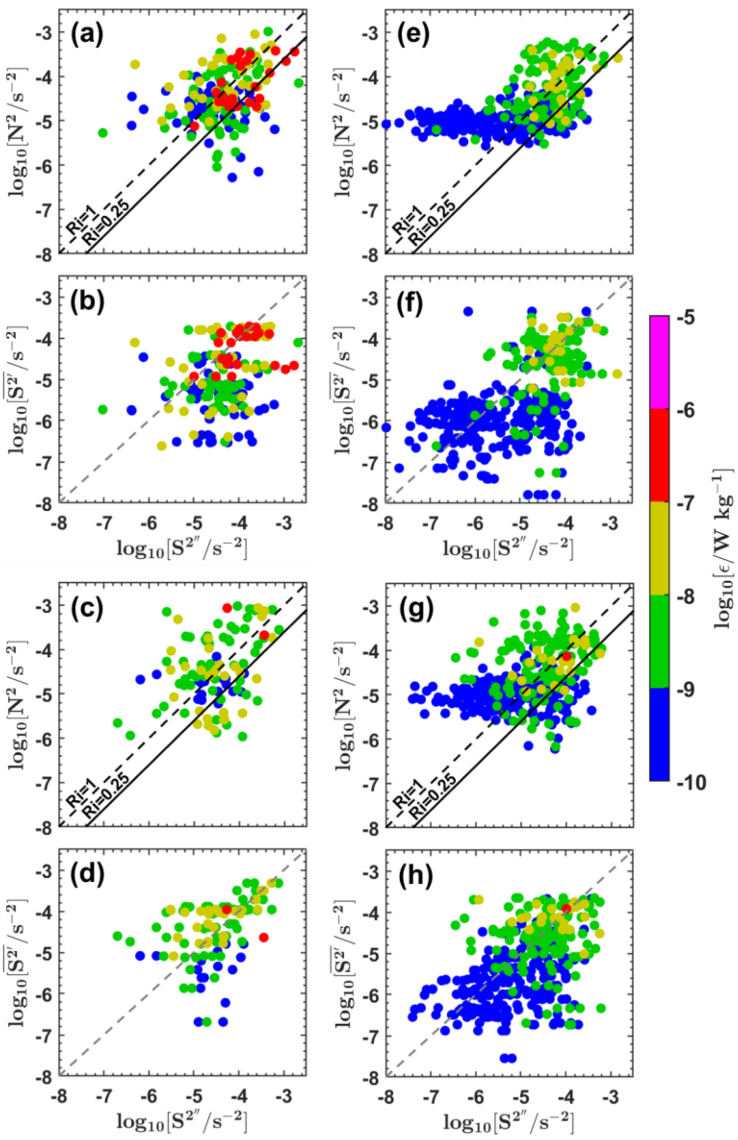
(a)
(b)
(c)
(d)
(e)
(f)
(g)
(h)
Ri=1
Ri=0.25
$\log_{10}[N^2/s^{-2}]$
$\log_{10}[\overline{S^{2'}}/s^{-2}]$
$\log_{10}[S^{2''}/s^{-2}]$
-3
-4
-5
-6
-7
-8
$\log_{10}[\epsilon/W\ kg^{-1}]$
-5
-6
-7
-8
-9
-10

Figure A20: Dissipation rates (ε, in W kg-1, on a logarithmic scale) below the XLD as a function of the buoyancy frequency squared (N2, in s-2, on a logarithmic scale) and semi-diurnal baroclinic vertical shear squared ($S^{2''}$, in m s-1, on a logarithmic scale) for stations (a) S6, (c) S7, (e) S12, and (g) S13. Dissipation rates (ε, in W kg-1, on a logarithmic scale) below the XLD as a function of mean baroclinic vertical shear squared ($\overline{S^{2'}}$, in m s-1, on a logarithmic scale) and semi-diurnal baroclinic vertical shear squared ($S^{2''}$, in m s-1, on a logarithmic scale) for stations (b) S6, (d) S7, (f) S12, and (h) S13. N2 was linearly interpolated into the depths of $S^{2''}$ to have same vertical scales. Panels (a), (c), (e), and (g) also display two solid black lines corresponding to Richardson number Ri = 0.25 and Ri = 1, respectively. Dashed grey lines in panels (b), (d), (f), and (h) are included for comparison purposes.

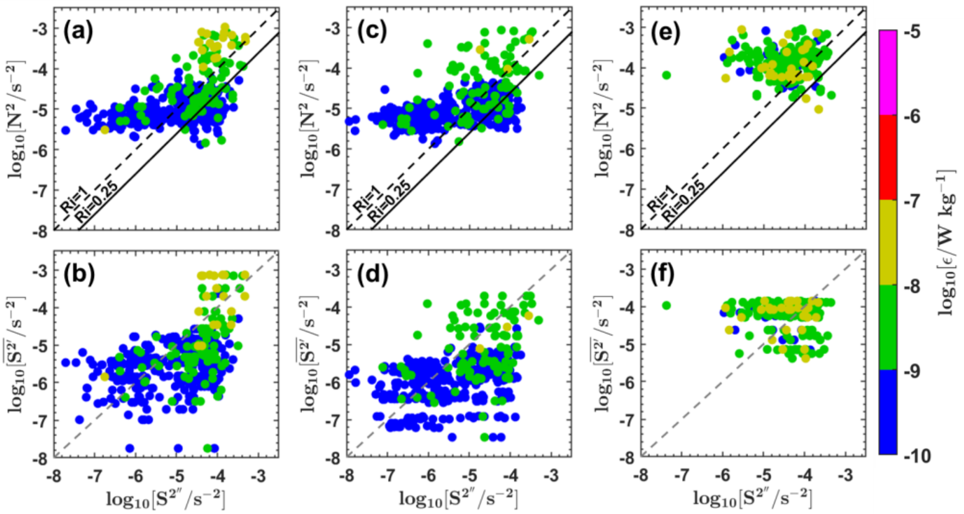

Figure A21: Panels are similar to Fig. A20 but for stations (a)-(b) S20, (c)-(d) S21, and (e)-(f) S24.

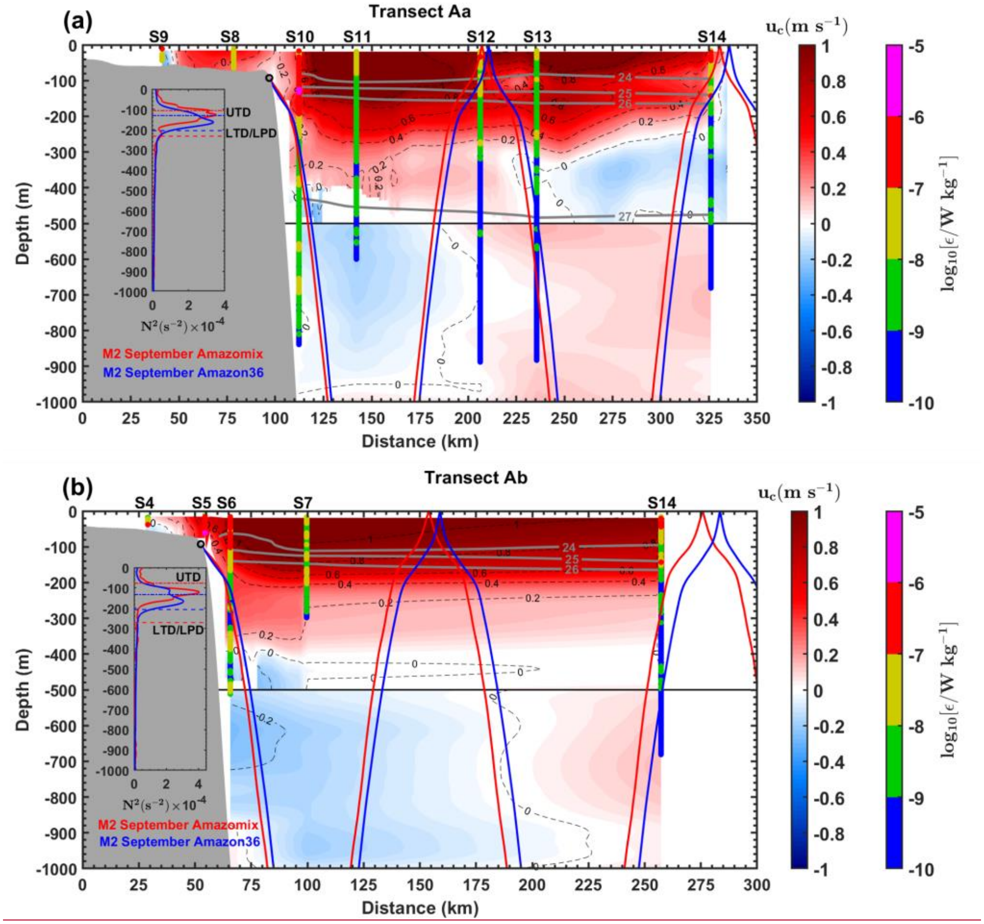

Figure A22: Panels are similar to Fig. 8 but for cross-shore mean total currents (u_c, in m s-1) from ADCP (Dashed black lines).

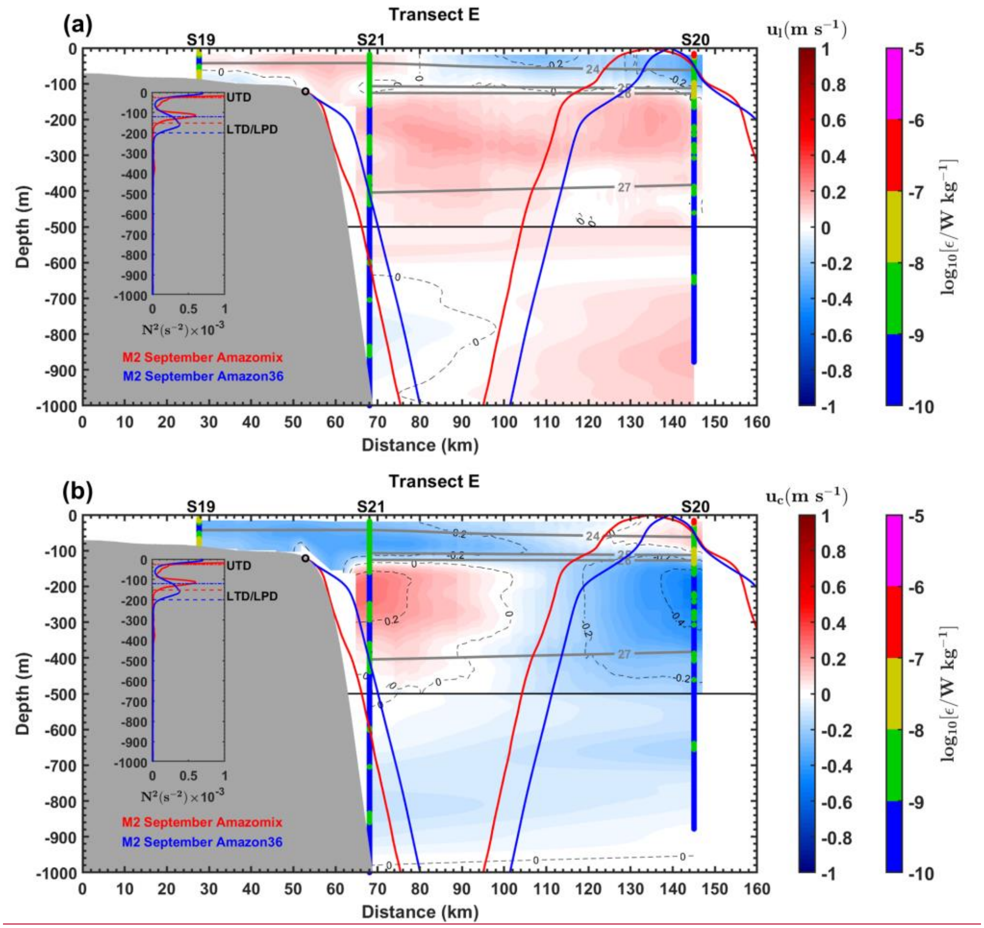

Figure A23: (a) Similar to Fig. 8 but for transect E. (b) Similar to Fig. A22 but for transect E.

Formatted: Font: Not Italic

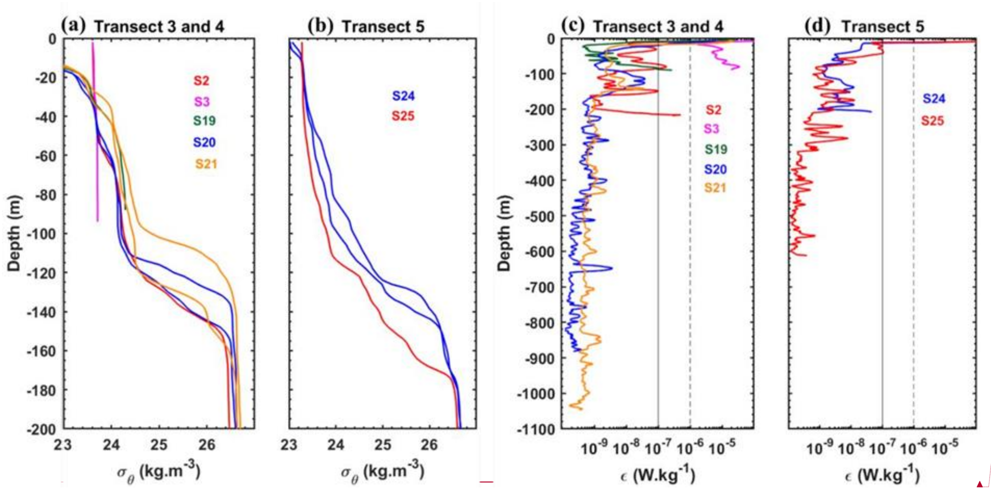

~~Figure A1: (a)-(b) Potential density profiles (in kg.m-3) from CTD-O2 and (c)-(d) vertical dissipation rates (ε in W.kg-1, on log scale) from VMP during the AMAZOMIX 2021 cruise for the transects/stations inside of the IT fields (a)-(c) T3 (S2 and S3) and T4 (S19-S21), and far from IT fields (b)-(d) T5 (S24 and S25). For long stations (S20 and S21), two density profiles are used to illustrate the isopycnal vertical displacements along the transects. The potential density at S3 varies between 23.6-23.72 kg.-3. Color of profiles is used to distinguish each station in each transect.~~

Formatted: Font: Not Bold

Formatted: Font: Not Italic

Formatted: Font: Not Italic, Not Superscript/ Subscript

Formatted: Font: Not Italic

Formatted: Font: Not Italic, Not Superscript/ Subscript

Formatted: Font: Not Italic

Formatted: Font: Not Italic, Not Superscript/ Subscript

Formatted: Font: Not Italic

Formatted: Font: Not Italic, Not Superscript/ Subscript

Formatted: Font: Not Italic

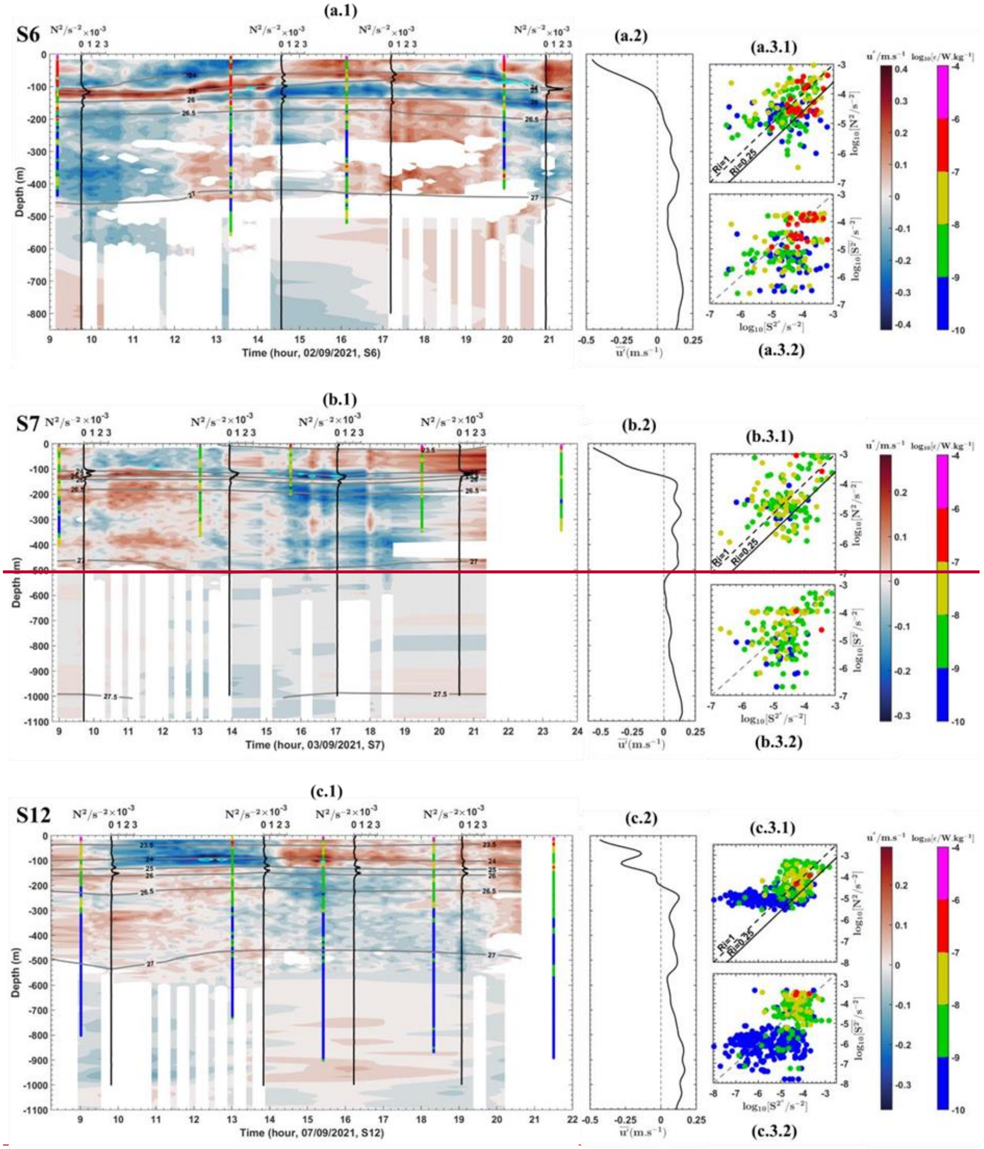
(a.1)
S6
$N^2/s^{-2} \times 10^{-3}$
0 1 2 3
Depth (m)
Time (hour, 02/09/2021, S6)
(a.2)
$\overline{u'}$(m.s^{-1})
(a.3.1)
(a.3.2)
Ri=1
Ri=0.25
$\log_{10}[N^2/s^{-2}]$
$\log_{10}[\overline{S^2}/s^{-2}]$
$\log_{10}[S^{2'}/s^{-2}]$
u' /m.s^{-1}
$\log_{10}[\epsilon$/W.kg$^{-1}]$
(b.1)
S7
Time (hour, 03/09/2021, S7)
(b.2)
(b.3.1)
(b.3.2)
(c.1)
S12
Time (hour, 07/09/2021, S12)
(c.2)
(c.3.1)
(c.3.2)
23.5
24
25
26
26.5
27
27.5

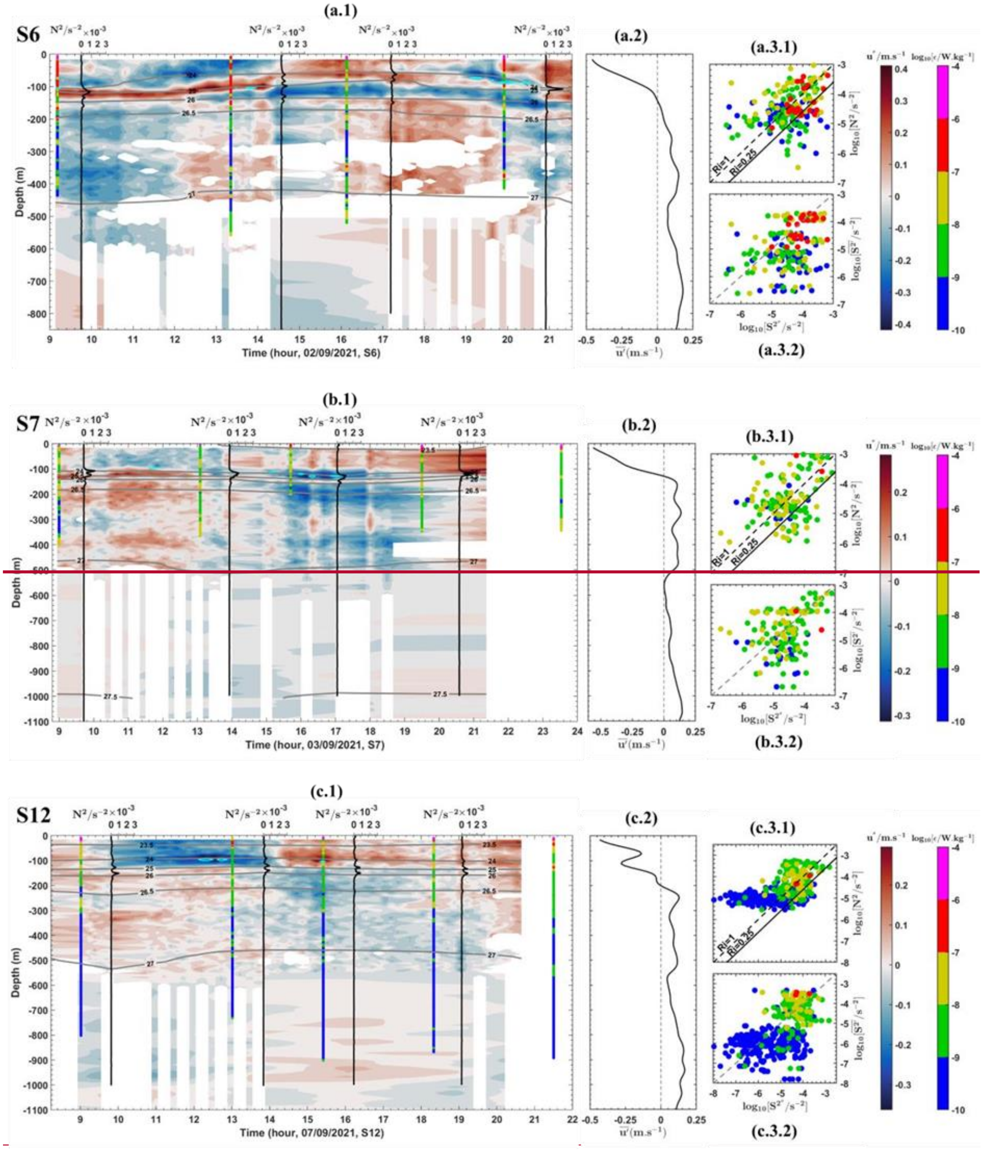
(a.1)
S6
N²/s⁻²×10⁻³
0 1 2 3
Depth (m)
Time (hour, 02/09/2021, S6)
(a.2)
u'(m.s⁻¹)
(a.3.1)
(a.3.2)
Ri=1
Ri=0.25
log₁₀[N²/s⁻²]
log₁₀[S²/s⁻²]
u'/m.s⁻¹
log₁₀[ε/W.kg⁻¹]
(b.1)
S7
N²/s⁻²×10⁻³
0 1 2 3
Depth (m)
Time (hour, 03/09/2021, S7)
(b.2)
u'(m.s⁻¹)
(b.3.1)
(b.3.2)
Ri=1
Ri=0.25
log₁₀[N²/s⁻²]
log₁₀[S²/s⁻²]
u'/m.s⁻¹
log₁₀[ε/W.kg⁻¹]
(c.1)
S12
N²/s⁻²×10⁻³
0 1 2 3
Depth (m)
Time (hour, 07/09/2021, S12)
(c.2)
u'(m.s⁻¹)
(c.3.1)
(c.3.2)
Ri=1
Ri=0.25
log₁₀[N²/s⁻²]
log₁₀[S²/s⁻²]
u'/m.s⁻¹
log₁₀[ε/W.kg⁻¹]

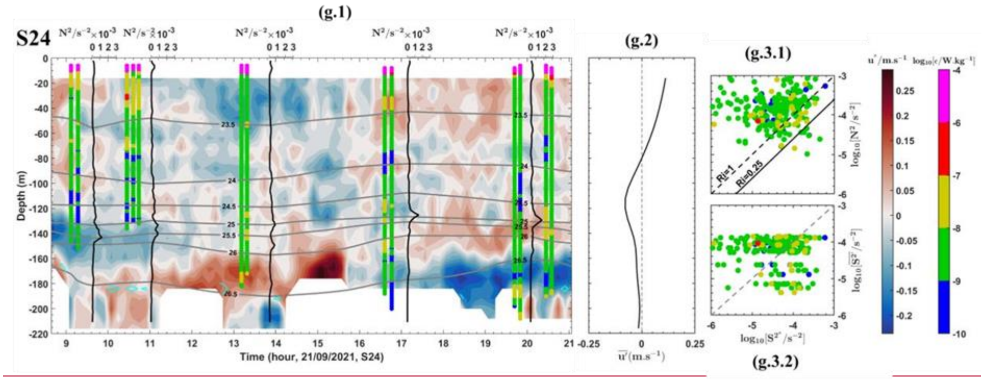

~~Figure A2: (1st column: a.1 to g.1) Semi-diurnal (□'' in m.s−1) baroclinic zonal currents from ADCP overlaid the semi-diurnal vertical shear squared (□2''in s-2 x10-3 with the following contours values: 1.4 at S6, 0.8 at S7, 1.1 at S12, 0.55 at S13, 0.5 at S20, 0.4 at S21 and 1.0 at S24, in cyan contours) from ADCP, the buoyancy frequency squared (N2 in s-2, in vertical black lines) and potential density (in grey contours background shift) from CTD-O2 and dissipation rates (ε in W.kg-1 on log scale, in coloured bars) profiles from VMP. (2nd column: a.2 to g.2) Baroclinic mean (alongshore current) velocity (□' in m.s−1) from ADCP. (3rd column: a.3.1 to g.3.1) ε as a function of □2'' and N2 overlaid Richardson number (with critical value Ri = 0.25 in solid black line and Ri=1 in dashed black line). (3rd column: a.3.2 to g.3.2) ε as function of mean vertical shear squared (□2' in s-2) and □2''overlaid dashed grey line for comparison. (first line, panels a) for S6, (second line, panels b) for S7, (third line, panels c) for S12, (fourth line, panels d) for S13, (fifth line, panels e) for S20, (sixth line, panels f) for S21 and (seventh line, panels g) for S24. N2 was linearly interpolated into the depths of □2'' to have same vertical scales.~~

Formatted ...

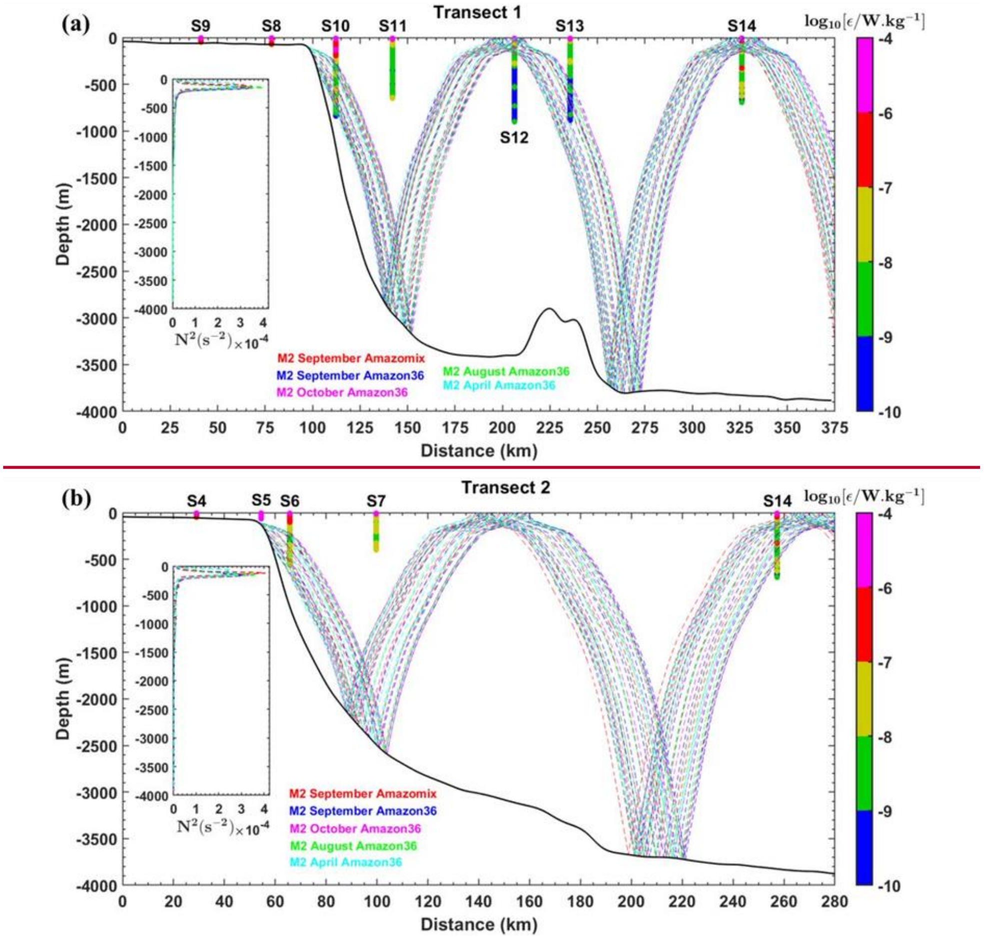
(a)
Transect 1
S9
S8
S10
S11
S12
S13
S14
log₁₀[ε/W.kg⁻¹]
-4
-6
-7
-8
-9
-10
Depth (m)
Distance (km)
0
-500
-1000
-1500
-2000
-2500
-3000
-3500
-4000
0
25
50
75
100
125
150
175
200
225
250
275
300
325
350
375
N²(s⁻²)×10⁻⁴
0 1 2 3 4
M2 September Amazomix
M2 September Amazon36
M2 October Amazon36
M2 August Amazon36
M2 April Amazon36
(b)
Transect 2
S4
S5
S6
S7
S14
0
20
40
60
80
100
120
140
160
180
200
220
240
260
280

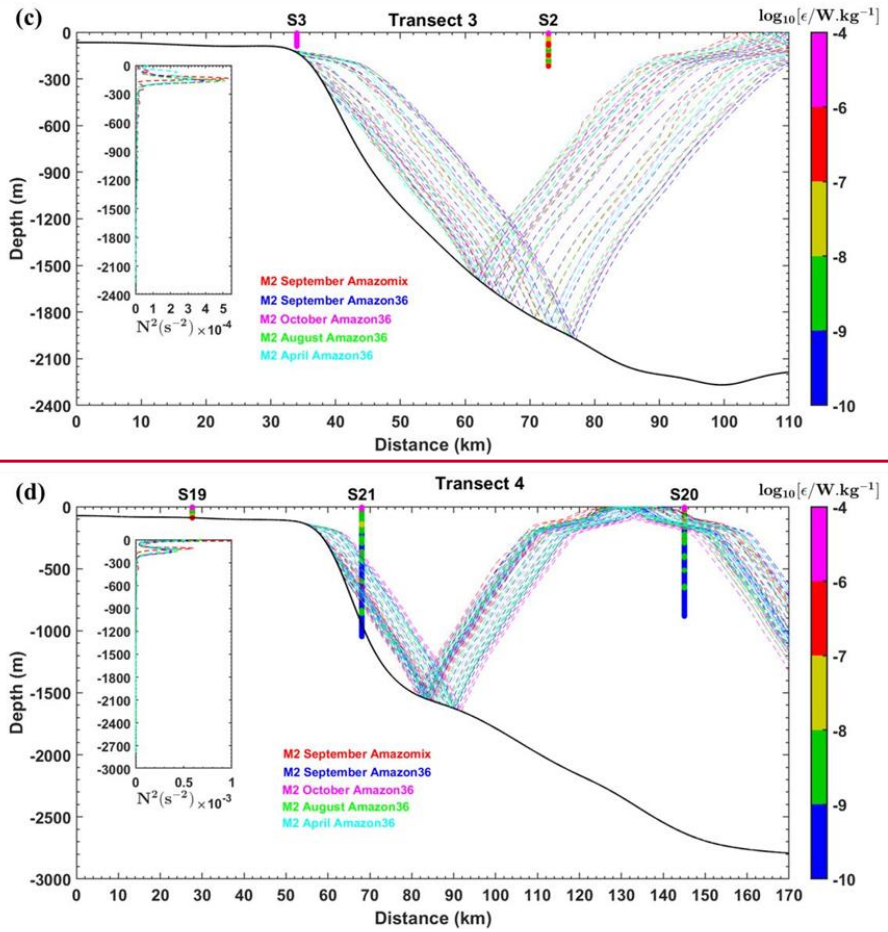
(c)
Transect 3
S3
S2
$\log_{10}[\epsilon/\mathrm{W.kg^{-1}}]$
-4
-6
-7
-8
-9
-10
Depth (m)
Distance (km)
0
-300
-600
-900
-1200
-1500
-1800
-2100
-2400
0 10 20 30 40 50 60 70 80 90 100 110
$\mathrm{N^2(s^{-2})} \times 10^{-4}$
0 1 2 3 4 5
M2 September Amazomix
M2 September Amazon36
M2 October Amazon36
M2 August Amazon36
M2 April Amazon36
(d)
Transect 4
S19
S21
S20
$\log_{10}[\epsilon/\mathrm{W.kg^{-1}}]$
-4
-6
-7
-8
-9
-10
Depth (m)
Distance (km)
0
-500
-1000
-1500
-2000
-2500
-3000
0 10 20 30 40 50 60 70 80 90 100 110 120 130 140 150 160 170
0 -300 -600 -900 -1200 -1500 -1800 -2100 -2400 -2700 -3000
$\mathrm{N^2(s^{-2})} \times 10^{-3}$
0 0.5 1
M2 September Amazomix
M2 September Amazon36
M2 October Amazon36
M2 August Amazon36
M2 April Amazon36

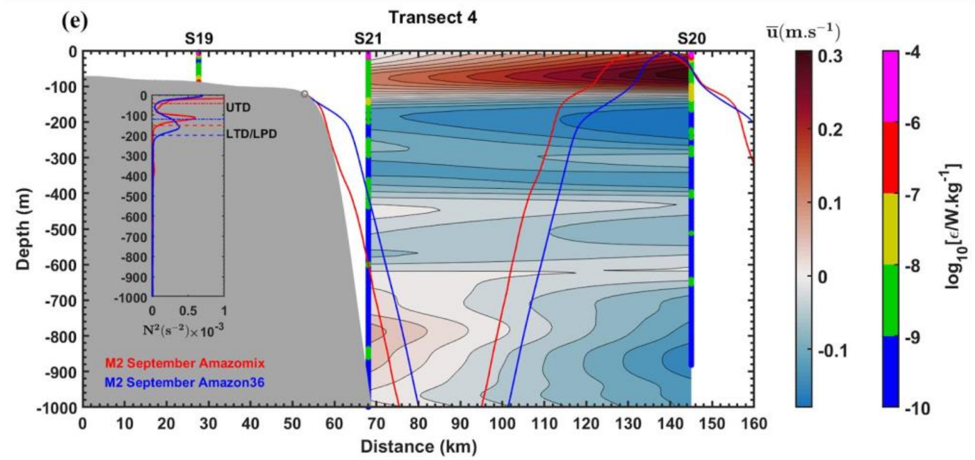

~~Figure A3: (a)-(d) Sensibility tests of IT ray tracing by varying the location of the critical topography in each month. Ray tracing for the M2 tidal constituent assuming the mean stratification (N2 in s-2, in overlaid Figure in each panel) from AMAZOMIX CTD-O2 (of September 2021) and NEMO model (Amazon36 of September, October, August and April, 2012-2016), along the transects (a) T1, (b) T2, (c) T3 and (d) T4. Overlaid on the panels the profiles of dissipation rates (ε in W.kg1 in log scale, in coloured bars) from VMP. Solid black lines represent local bathymetry. Dashed colour lines are used to distinguish IT beam months in each transect. (e) Zoom in the upper layer of 1000 m at T4 showing IT ray tracing for September and the profiles of dissipation rates overlaid profiles of mean total (alongshore) current (ū in m.s−1, in background) from ADCP. UTD (in dotted lines) and LTD/LPD (in dashed lines) correspond to Upper and Lower Thermocline/Pycnocline Depth, respectively. In the panel (e), grey circles indicate the critical slope and grey areas represent local bathymetry.~~

Formatted: Font: Not Italic

Formatted: Font: Not Italic

Formatted: Font: Not Italic

Formatted: Font: Not Italic, Not Superscript/ Subscript

Formatted: Font: Not Italic

Formatted: Font: Not Italic, Not Superscript/ Subscript

Formatted: Font: Not Italic

Formatted: Font: Not Italic, Not Superscript/ Subscript

Formatted: Font: Not Italic

Formatted: Font: Not Italic

Formatted: Font: Not Italic, Not Superscript/ Subscript

Formatted: Font: Not Italic

Formatted: Font: Not Italic

Formatted: Font: Not Italic, Not Superscript/ Subscript

Formatted: Font: Not Italic

Formatted: Font: Not Bold

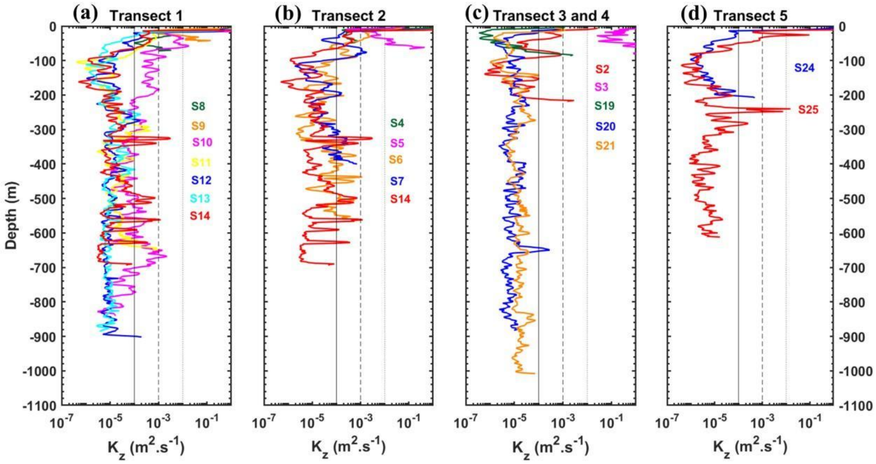

~~Figure A4: Vertical diffusivity (in m2.s-1) during AMAZOMIX 2021 cruise for the transects/stations inside of the IT fields (a) T1 (S8-S14), (b) T2 (S4-S7 and S14), and (c) T3 (S2 and S3) and T4 (S19-S21), and far from IT fields (d) T5 (S24 and S25).~~

~~Colour is used to distinguish each station in each transect. Dashed and solid back lines are for comparison.~~

Formatted: Font: Not Italic

Formatted: Font: Not Italic

Formatted: Font: Not Italic, Not Superscript/ Subscript

Formatted: Font: Not Italic

Formatted: Font: Not Italic, Not Superscript/ Subscript

Formatted: Font: Not Italic

Formatted: Font: Not Italic

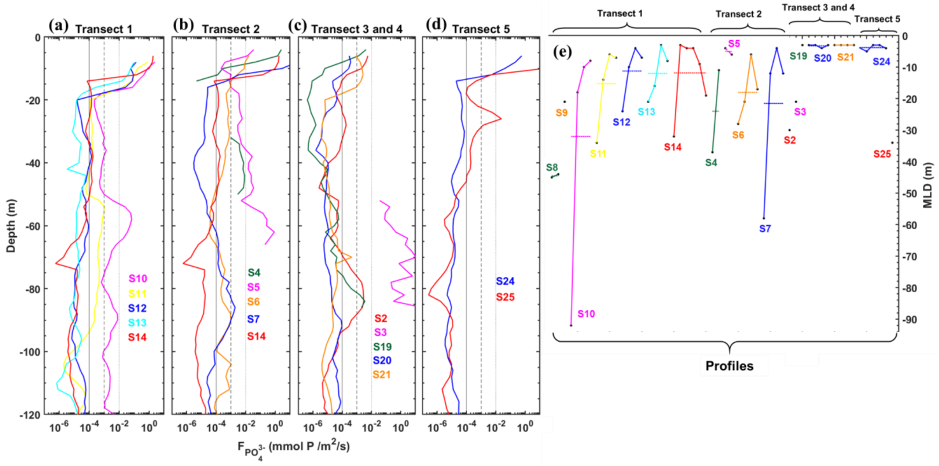

~~Figure A5: Vertical fluxes of phosphate (in mmol P m-2 s-1) at the base of MLD (defined at the MLD + 1m) during AMAZOMIX 2021 cruise for the transects/stations inside of the IT fields (a) T1 (S10-S14), (b) T2 (S4-S7 and S14), and (c) T3 (S2 and S3) and T4 (S19-S21), and far from IT fields (d) T5 (S24 and S25). Dashed and solid back lines are for comparison. (e) MLD (in~~

~~m) for each CTD-O2 profile (black dots) with average values (horizontal dashed lines) for each station. Colour is used to distinguish each station in each transect. S9 was missing from the phosphate data and the vertical flux of phosphate was null at S8 because of null phosphate concentration gradient in Fig. A5.a.~~

Formatted: Font: Not Italic

Formatted: Font: Not Italic, Not Superscript/ Subscript

Formatted: Font: Not Italic

Formatted: Font: Not Italic, Not Superscript/ Subscript

Formatted: Font: Not Italic

Formatted: Font: Not Italic

Formatted: Font: 10 pt, Not Italic, Not Superscript/ Subscript

Formatted: Font: Not Italic

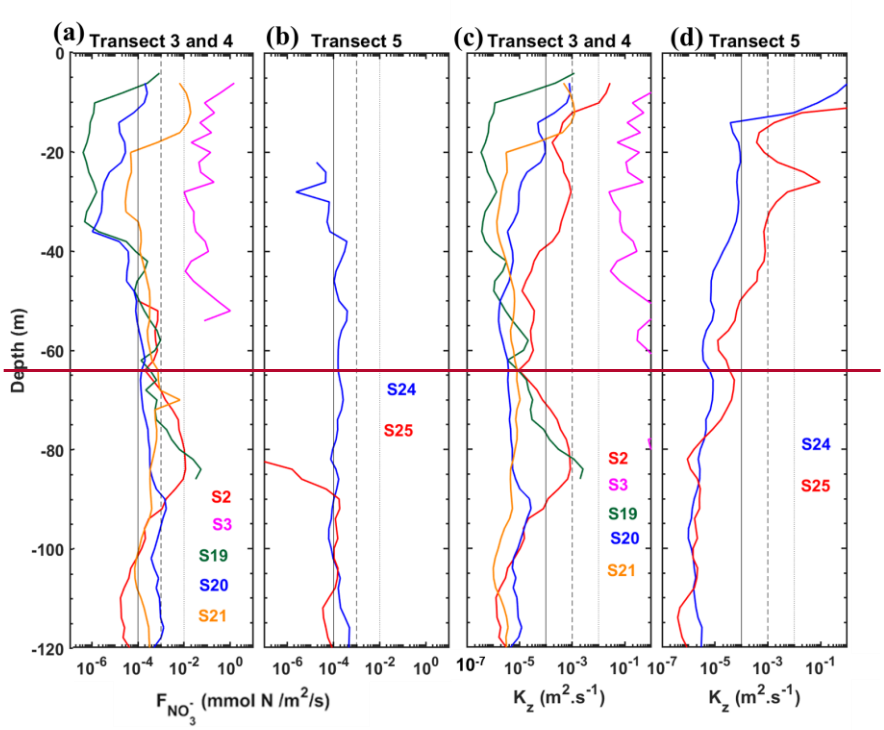

~~Figure A6: (a)-(b) Vertical fluxes of nitrate (in mmol N m-2.s-1) and (c)-(d) vertical diffusivity (in m2.s-1) at the base of MLD (defined at the MLD + 1m, see Figure A5.e) during AMAZOMIX 2021 cruise for the transects/stations inside of the IT fields (a)-(c) T3 (S2 and S3) and T4 (S19-S21), and far from the IT fields (b)-(d) T5 (S24 and S25). Dashed and solid back lines are for comparison. Colour is used to distinguish each station in each transect.~~

Table A1: miXing Layer Depth (XLD), Bottom layer-integrated flow Kinetic Energy (BKE), Contribution *(mean and standard deviation)* of the semi-diurnal (CSBS~~E~~) and mean baroclinic (CMBS~~E~~) shear~~energy~~ to total baroclinic shear~~energy~~ at AMAZOMIX stations. BKE was absent at stations with density stratification until the end of the profile.

Formatted: Font: Not Bold

Formatted: Font: Not Italic

Formatted: Font: Not Italic, Not Superscript/ Subscript

Formatted: Font: Not Italic

Formatted: Font: Not Italic, Not Superscript/ Subscript

Formatted: Font: Not Italic

Formatted: Font: 10 pt, Not Italic, Not Superscript/ Subscript

Formatted: Font: Not Italic

Formatted: Font: 10 pt, Not Italic, Not Superscript/ Subscript

Formatted: Font: Not Italic

Formatted: Font: Not Italic

Formatted: Font: Not Bold

Formatted: Font: Not Bold

Formatted: Font: Not Italic

Formatted: Font: Not Bold, Not Italic

Formatted: Font: Not Italic

Formatted: Font: Not Italic

N° Stations	XLD (m)	BKE (J.m-2)	CSBS (mean ± SD) (%)	CMBS (mean ± SD) (%)
S2	45	-	-	-
S3	31	35.4	-	-
S4	27	-	-	-
S5	20	16.6	-	-
S6	22	-	61.4 ± 5.3	38.6 ± 5.3
S7	46	-	47.5 ± 2.8	52.5 ± 2.8
S8	23	1.1	-	-
S9	29	2.6	-	-
S10	26	-	65.8 ± 0.7	34.2 ± 0.7
S11	27	-	48.2 ± 5.0	51.8 ± 5.0
S12	49	-	54.3 ± 3.1	48.7 ± 3.1
S13	17	-	55.4 ± 5.1	44.6 ± 5.1
S14	26	-	58.5 ± 1.5	41.5 ± 1.5
S19	27	0.6	-	-
S20	44	-	52.1 ± 3.8	47.9 ± 3.8
S21	53	-	58.5 ± 3.2	41. 5 ± 3.2
S24	21	0.2	49.1 ± 2.8	50.9 ± 2.8
S25	26	-	-	-

SD = Standard Deviation.

~~N° Stations~~	~~XLD (m)~~	~~BKE (J.m^{-2})~~	~~CSBES (%)~~	~~CMBSE (%)~~
~~S2~~	~~45 16~~	~~- -~~	-	-
~~S3~~	~~31 16~~	~~35.44 22.94~~	-	-
~~S4~~	~~27 12~~	~~- -~~	-	-
~~S5~~	~~20 8~~	~~16.63 9.52~~	-	-
~~S6~~	~~22 18~~	~~- -~~	~~61.442~~	~~38.568~~
~~S7~~	~~46 44~~	~~- -~~	~~478.4638~~	~~521.5462~~

~~**S8**~~	~~23 22~~	~~1.12 0.45~~	-	-
~~**S9**~~	~~29 14~~	~~2.64 1.32~~	-	-
~~**S10**~~	~~26 22~~	~~- -~~	~~65.8294~~	~~34.1806~~
~~**S11**~~	~~27 18~~	~~- -~~	~~48.107~~	~~51.893~~
~~**S12**~~	~~49 18~~	~~- -~~	~~541.3285~~	~~458.6815~~
~~**S13**~~	~~17 18~~	~~- -~~	~~556.4303~~	~~443.597~~
~~**S14**~~	~~26 14~~	~~- -~~	~~58.5094~~	~~41.5006~~
~~**S19**~~	~~27 24~~	~~0.56 0.56~~	-	-
~~**S20**~~	~~44 36~~	~~- -~~	~~52.1164~~	~~47.8936~~
~~**S21**~~	~~53 36~~	~~- -~~	~~589.5513~~	~~410.4587~~
~~**S24**~~	~~21 14~~	~~0.22 0.18~~	~~49.0559~~	~~50.9541~~
~~**S25**~~	~~26 12~~	~~- -~~	-	-

Data availability

The AMAZOMIX data can be downloaded directly on the SEANOE site: https://www.seanoe.org/data/00860/97235/. The NEMOv3.6 model outputs are available upon request by contacting the corresponding author.

Authors contributions

AKL: funding acquisition. FK and AKL, with assistance from JM: conceptualization and methodology. FK, with assistance from PR, AB, EC and AKL: data pre-processing. Formal analysis: FK with interactions from all co-authors. Preparation of the manuscript: FK with contributions from all co-authors. This work is a contribution to the LMI TAPIOCA (www.tapioca.ird.fr).

Competing interests

The authors declare that they have no conflict of interest.

Acknowledgments

The authors would like to thank the "Flotte Océanographique Française" and the officers and crew of the R/V Antea for their contribution to the success of the operations aboard the R/V ANTEA, as well as, all the scientists involved in data and water samples collection, for their valuable support during and after the AMAZOMIX cruise. We acknowledge the Brazilian

Formatted: Left, Indent: Left: 0,5 cm, Line spacing: Multiple 1,08 li

Formatted: Left, Indent: Left: 0,6 cm, Line spacing: Multiple 1,08 li

Formatted: Left, Indent: Left: 0,5 cm, Line spacing: Multiple 1,08 li

Formatted: Left, Indent: Left: 0,6 cm, Line spacing: Multiple 1,08 li

Formatted: Left, Indent: Left: 0,5 cm, Line spacing: Multiple 1,08 li

Formatted: Left, Indent: Left: 0,85 cm, Line spacing: Multiple 1,08 li

Formatted: Left, Indent: Left: 0,5 cm, Line spacing: Multiple 1,08 li

Formatted: Left, Indent: Left: 0,85 cm, Line spacing: Multiple 1,08 li

Formatted: Left, Indent: Left: 0,5 cm, Line spacing: Multiple 1,08 li

Formatted: Left, Indent: Left: 0,85 cm, Line spacing: Multiple 1,08 li

Formatted ...

Formatted ...

Formatted ...

Formatted ...

Formatted ...

Formatted ...

Formatted ...

Formatted ...

Formatted ...

Formatted ...

Formatted ...

Formatted ...

Formatted ...

Formatted ...

authorities for authorising the survey. The authors acknowledge Rockland company for their instrument and their support during the cruise and during the analysis of the VMP data, the National french parc of instrument (DT-INSU) for their instrument during the cruise and support in data analysis, as well as, the US-IMAGO from IRD for its help during the cruise and for biogeochemical data analysis.

Financial support

This work is a part of the project “AMAZOMIX”, funded multiple agencies : the “Flotte Océanographique Française” that funded the 40 days at sea of the R/V Antea, the Institut de Recherche pour le Développement (IRD), via among other the LMI TAPIOCA, the CNES, within the framework of the APR TOSCA MIAMAZ TOSCA project (PIs Ariane Koch-Larrouy, Vincent Vantrepotte, and Isabelle Dadou), the LEGOS and the program international Franco-Brazileiro GUYAMAZON (call Nº 005/2017). It is also part of the PhD Thesis of Fabius Kouogang, funded by the Coordenação de Aperfeiçoamento de Pessoal de Nível Superior (CAPES), under the co-advisement of Ariane Koch-Larrouy and Moacyr Araujo.

References

Araujo, M., Noriega, C., Hounsou-gbo, G. A., Veleda, D., Araujo, J., Bruto, L., Feitosa, F., Flores-Montes, M., Lefèvre, N., Melo, P., Otsuka, A., Travassos, K., Schwamborn, R., and Neumann-Leitão, S.: A Synoptic Assessment of the Amazon River-Ocean Continuum during Boreal Autumn: From Physics to Plankton Communities and Carbon Flux, Front. Microbiol., 8:1358, https://doi.org/10.3389/fmicb.2017.01358, 2017.

Assene, F., Koch-Larrouy, A., Dadou, I., Tchilibou, M., Morvan, G., Chanut, J., Costa da Silva, A., Vantrepotte, V., Allain, D., and Tran, T.-K.: Internal tides off the Amazon shelf – Part 1: The importance of the structuring of ocean temperature during two contrasted seasons, Ocean Sci., 20, 43–67, https://doi.org/10.5194/os-20-43-2024, 2024.

Assuncao, R. V., Silva, A. C., Roy, A., Bourlès, B., Silva, C. A. H. S., Ternon, J.-F., Araujo, M., and Bertrand, A.: 3D characterisation of the thermohaline structure in the southwestern tropical Atlantic derived from functional data analysis of in situ profiles, Progress in Oceanography, 187, pp.102399, https://doi.org/10.1016/j.pocean.2020.102399. hal02984588, 2020.

Barbot, S., Lyard, F., Tchilibou, M., and Carrere, L.: Background stratification impacts on internal tide generation and abyssal propagation in the western equatorial Atlantic and the Bay of Biscay, Ocean Sci., 17, 1563–1583, https://doi.org/10.5194/os-17-1563-2021 , 2021.

Barnier, B., Reynaud, T., Beckmann, A., Böning, C., Molines, J.-M., Barnard, S., and Jia, Y.: On the seasonal variability and eddies in the North Brazil Current: insights from model intercomparison experiments, Prog. Oceanogr., 48, 195–230, https://doi.org/10.1016/S0079-6611(01)00005-2, 2001.

Bertrand, A., de Saint Leger, E., and Koch-Larrouy, A.: AMAZOMIX 2021 cruise, RV Antea, https://doi.org/10.17600/18001364, 2021.

Booth, J. and Kamenkovich, I.: Isolating the role of mesoscale eddies in mixing of a passive tracer in an eddy resolving model, J. Geophys. Res., 113, C05021, https://doi.org/10.1029/2007JC004510, 2008.

Bordois, L.: Internal tide modeling : Hydraulic & Topographic controls, Ph.D. thesis, Université Toulouse III Paul-Sabatier, 195 pp., tel-01281760, version 1., https://theses.hal.science/tel-01281760, 2015.

Bourlès, B., Gouriou, Y., and Chuchla, R.: On the circulation in the upper layer of the western equatorial Atlantic, Journal of Geophysical Research, 104, 21151-21170, https://doi.org/10.1029/1999JC900058, 1999.

Bouruet-Aubertot, P., Cuypers, Y., Ferron, B., Dausse, D., Ménage, O., Atmadipoera, A. S., and Jaya, I.: Contrasted turbulence intensities in the Indonesian Throughflow: a challenge for parameterizing energy dissipation rate, Ocean Dynamics, 68, 779–800, https://doi.org/10.1007/s10236-018-1159-3, 2018.

Brainerd, K., and Gregg M. C.: Surface mixed and mixing layer depths, Deep Sea Res., 42(9), 1521–1543, https://doi.org/10.1016/0967-0637(95)00068-H, 1995.

Cisewski, B., Strass, V. H., Losch, M., and Prandke, H.: Mixed layer analysis of a mesoscale eddy in the Antarctic Polar Front Zone, J. Geophys. Res., 113, C05017, https://doi.org/10.1029/2007JC004372, 2008.

Coles, V. J., Brooks, M. T., Hopkins, J., Stukel, M. R., Yager, P. L., and Hood, R. R.: The pathways and properties of the Amazon River Plume in the tropical North Atlantic Ocean, Journal of Geophysical Research, 118, 6894-6913, https://doi.org/10.1002/2013JC008981, 2013.

Didden, N. and Schott, F.: Eddies in the North Brazil Current retroflection region observed by Geosat altimetry, J. Geophys. Res., 98, 20121, https://doi.org/10.1029/93JC01184, 1993.

de Boyer Montégut, C., Madec G., Fischer A. S., Lazar A., and Iudicone D.: Mixed layer depth over the global ocean: An examination of profile data and a profile-based climatology, J. Geophys. Res., 109, C12003, https://doi.org/10.1029/2006JC004051, 2004.

de Macedo, C. R., Koch-Larrouy, A., da Silva, J. C. B., Magalhães, J. M., Lentini, C. A. D., Tran, T. K., Rosa, M. C. B., and Vantrepotte, V.: Spatial and temporal variability in mode-1 and mode-2 internal solitary waves from MODIS-Terra sun glint off the Amazon shelf, Ocean Sci., 19, 1357–1374, https://doi.org/10.5194/os-19-1357-202, 2023.

Dossa, N., da Silva, A. C., Koch-Larrouy, A., and Kouogang, F.: Near-surface western boundary circulation off the Amazon Plume from AMAZOMIX data, in preparation, 2024.

Fer, I., Dengler, M., Holtermann, P. et al.: ATOMIX benchmark datasets for dissipation rate measurements using shear probes, Sci Data, 11, 518, https://doi.org/10.1038/s41597-024-03323-y, 2024.

Gerkema, T., and Zimmerman, J. T. F.: An Introduction to Internal Waves, 207 pp, 2008

Geyer, W. R.: Tide-induced mixing in the Amazon Frontal Zone, J. Geophys. Res., 100, 2341, https://doi.org/10.1029/94JC02543, 1995.

Gille, S.T., Ledwell, J., Naveira-Garabato, A., Speer, K., Balwada, D., Brearley, A., Girton, J.B., Griesel, A., Ferrari, R., Klocker, A., LaCasce, J., Lazarevich, P., Mackay, N., Meredith, M.P., Messias, M.-J., Owens, B., Sallée, J.-B., Sheen, K., Shuckburgh, E., Smeed, D. A., St. Laurent, L.C., Toole, J.M., Watson, A.J., Wienders, N., and Zajaczkovski, U.: The diapycnal and isopycnal mixing experiment: a first assessment, CLIVARExchanges, 17(1), 46–48, https://nora.nerc.ac.uk/id/eprint/18245, 2012.

Gregg, M., Sanford, T., and Winkel, D.: Reduced mixing from the breaking of internal waves in equatorial waters, Nature, 422, 513–515, https://doi.org/10.1038/nature01507, 2003.

Huang, P.-Q., Cen, X.-R., Lu, Y.-Z., Guo, S.-X., and Zhou, S.-Q.: Global distribution of the oceanic bottom mixed layer thickness, Geophysical Research Letters, 46, 1547–1554, https://doi.org/10.1029/2018GL081159, (2019).

Huthnance, J. M.: Circulation, exchange and water masses at the ocean margin: the role of physical processes at the shelf edge, Progress in Oceanography, 35, 353–431, https://doi.org/10.1016/0079-6611(95)80003-C, 1995.

Inall, M. E., Toberman, M., Polton, J. A., Palmer, M. R., Green, J. A. M., and Rippeth, T. P.: Shelf Seas Baroclinic Energy Loss: Pycnocline Mixing and Bottom Boundary Layer Dissipation, Journal of Geophysical Research: Oceans, 126(8):2020JC016528, https://doi.org/10.1029/2020JC016528, 2021.

Ivey, G. N., Bluteau, C. E., Gayen, B., Jones, N. L., and Sohail, T.: Roles of Shear and Convection in Driving Mixing in the Ocean, Geophysical Research Letters, 48(3), e2020GL089455, https://doi.org/10.1029/2020GL089455, 2021.

Jackson, C. R., da Silva, J. C. B., and Jeans, G.: The generation of nonlinear internal waves, Oceanography, 25(2):108–123, https://doi.org/10.5670/oceanog.2012.46, 2012.

Johns, W. E., Lee, T. N., Beardsley, R. C., Candela, J., Limeburner, R., and Castro Filho, B. M. : Annual Cycle and Variability of the North Brazil Current, Journal of Physical Oceanography, 28(1), 103-128, https://doi.org/10.1175/15200485(1998)028%3C0103:acavot%3E2.0.co;2, 1998.

Kaneko, H., Yasuda, I., Itoh, S., and Ito, S.-I.: Vertical turbulent nitrate flux from direct measurements in the western subarctic and subtropical gyres of the North Pacific, J. Oceanogr., 77, 29–44, https://doi.org/10.1007/s10872-020-00576-0, 2021.

Koch-Larrouy, A., Atmadipoera, A., van Beek, P., Madec, G., Aucan, J., Lyard, F., Grelet, J., and Souhaut, M.: Estimates of tidal mixing in the Indonesian archipelago from multidisciplinary INDOMIX in-situ data, Deep Sea Research Part I: Oceanographic Research Papers, 106, pp.136-153, https://doi.org/10.1016/j.dsr.2015.09.007, 2015.

Koch-Larrouy, A., Lengaigne, M., Terray, P., Madec, G., and Masson, S.: Tidal mixing in the Indonesian Seas and its effect on the tropical climate system, Clim. Dynam., 34, 891–904, https://doi.org/10.1007/s00382-009-0642-4, 2010.

Koch-Larrouy, A., Kerhervé, D., and Kouogang, F.: Evidence of overturns from AMAZOMIX off the Amazon shelf along internal tides paths, in preparation, 2024.

Klymak, J. M., Pinkel, R., and Rainville, L.: Direct breaking of the internal tide near topography: Kaena ridge, hawaii, J. Phys. Oceanogr., 38 (2), 380–399, https://doi.org/10.1175/2007JPO3728.1, 2008.

Kunze, E.: The internal-wave-driven meridional overturning circulation, J. Phys. Oceanogr., 47, 2673–2689, https://doi.org/10.1175/JPO-D-16-0142.1, 2017.

Le Bars, M., Lacaze, L., Le Dizes, S., Le Gal, P., and Rieutord, M.: Tidal instability in stellar and planetary binary systems, Physics of the Earth and Planetary Interiors, 178, 48-55, https://doi.org/10.1016/j.pepi.2009.07.005, 2010.

Lozovatsky, I. D., Roget, E., Fernando, H. J. S., Figueroa, M., and Shapovalov, S.: Sheared turbulence in a weakly stratified upper ocean, Deep Sea Res. Part I, 53, 387–407, https://doi.org/10.1016/j.dsr.2005.10.002, 2006.

Lueck, R., Fer, I., Bluteau, C., Dengler, M., Holtermann, P., Inoue, R., LeBoyer, A., Nicholson, S., Schulz, K., and Stevens, C.L: Best practices recommendations for estimating dissipation rates from shear probes, Frontiers in Marine Science, https://doi.org/10.3389/fmars.2024.1334327, 2024.

MacKinnon, J. A., and Gregg, M. C.: Mixing on the Late-Summer New England Shelf-Solibores, Shear, and Stratification, Journal of Physical Oceanography, 33, 1476-1492, https://doi.org/10.1175/1520-

0485(2003)033<1476:MOTLNE>2.0.CO;2, 2003.

Madec, G., Bourdallé-Badie, R., Chanut, J., Clementi, E., Cow-ard, A., Ethé, C., Iovino, D., Lea, D., Lévy, C., Lo-vato, T., Martin, N., Masson, S., Mocavero, S., Rousset,C., Storkey, D., Vancoppenolle, M., Müeller, S., Nurser, G., Bell, M., and Samson, G.: NEMO ocean engine, Zenodo, https://doi.org/10.5281/zenodo.3878122, 2019.

Magalhaes, J. M., da Silva, J. C. B., Buijsman, M. C., and Garcia, C. A. E.: Effect of the North Equatorial Counter Current on the generation and propagation of internal solitary waves off the Amazon shelf (SAR observations), Ocean Sci., 12, 243–255, https://doi.org/10.5194/os-12-243-2016, 2016.

M'hamdi, A., Koch-Larrouy, A., Bosse, A., de Macedo, C., Vantrepotte, V., Dadou, I., da Silva, A. C., and Kouogang, F.: Internal tides imprints on chlorophyll in mesoscale intrathermocline lenses detected from ocean color and from in-situ glider data off the Amazon shelf, Ocean Sci., (in preparation), 2024.

Miles, J. W.: On the stability of heterogeneous shear flows, Journal of Fluid Mechanics, 10(4):496-508, https://doi.org/10.1017/S0022112061000305, 1961.

Muacho, S., da Silva, J. C. B., Brotas, V., Oliveira, P. B., and Magalhaes, J. M.: Chlorophyll enhancement in the central region of the Bay of Biscay as a result of internal tidal wave interaction, Journal of Marine Systems, 136, 22–30, https://doi.org/10.1016/j.jmarsys.2014.03.016, 2014.

Munk, W., and Wunsch, C.: Abyssal recipes II: Energetics of tidal and wind mixing. Deep Sea Research, Part I: Oceanographic Research Papers, 45, 1977–2010, https://doi.org/10.1016/S0967-0637(98)00070-3, 1998.

Nasmyth, P. W.: Oceanic turbulence, Ph.D. thesis, University of British Columbia, 71 pp, https://doi.org/10.14288/1.0084817, 1970.

Neto, A. V. N., and da Silva, A. C.: Seawater temperature changes associated with the North Brazil current dynamics, Ocean Dynamics, 64, 13–27, https://doi.org/10.1007/s10236-013-0667-4, 2014.

New, A. L., and Pingree, R. D.: Local Generation Of Internal Soliton Packets In The Central Bay Of Biscay, Deep-Sea Research Part A-Oceanographic Research Papers, 39 (9A), 1521 - 1534, https://doi.org/10.1016/0198-0149(92)90045-U, 1992.

New, A., and da Silva, J.: Remote-sensing evidence for the local generation of internal soliton packets in the central Bay of Biscay, Deep Sea Research Part I: Oceanographic Research Papers, 49, 915–934, https://doi.org/10.1016/S09670637(01)00082-6, 2002.

Noh, Y., Lee, WS.: Mixed and mixing layer depths simulated by an OGCM, J. Oceanogr., 64, 217–225, https://doi.org/10.1007/s10872-008-0017-1, 2008.

Nugroho, D., Koch-Larrouy, A., Gaspar, P., Lyard, F., Reffray, G., and Tranchant, B.: Modelling explicit tides in the Indonesian seas: An important process for surface sea water properties, Mar. Pollut. Bull., 131, 7–18, https://doi.org/10.1016/j.marpolbul.2017.06.033, 2018.

Osborn, T. R.: Estimates of the local rate of vertical diffusion from dissipation measurements, J. Phys. Oceanogr, 10, 83–89, https://doi.org/10.1175/1520-0485(1980)010<0083:EOTLRO>2.0.CO;2, 1980.

Prestes, Y. O., Silva, A. C., and Jeandel, C.: Amazon water lenses and the influence of the North Brazil Current on the continental shelf, Continental Shelf Research, 160, 36-48, https://doi.org/10.1016/j.csr.2018.04.002, 2018.

Rainville, L., and Pinkel, R.: Propagation of Low-Mode Internal Waves through the Ocean, Journal of Physical Oceanography, 36:1220, 2006, https://doi.org/10.1175/JPO2889.1, 2006.

Ray, R. D., and Susanto, R. D.: Tidal mixing signatures in the Indonesian seas from high resolution sea surface temperature data. Geophys, Res. Lett, 43, 8115–8123, https://doi.org/10.1002/2016GL069485, 2016.

Rippeth, T. P., Palmer, M. R., Simpson, J. H., Fisher, N. R., and Sharples, J.: Thermocline mixing in summer stratified continental shelf sea, Geophys. Res. Lett, 32 (5), L05602, https://doi.org/10.1029/2004GL022104, 2005.

Ruault, V., Jouanno, J., Durand, F., Chanut, J., and Benshila, R.: Role of the Tide on the Structure of the Amazon Plume: A Numerical Modeling Approach, J. Geophys. Res.-Oceans, 125, e2019JC015495, https://doi.org/10.1029/2019JC015495, 2020.

Sharples, J., and Zeldis, J. R.: Variability of internal tide energy, mixing and nitrate fluxes in response to changes in stratification on the northeast New Zealand continental shelf. New Zeal, J. Mar. Fresh, 55: 94 - 111, https://doi.org/10.1080/00288330.2019.1705357, 2019.

Sheen, K.L., Brearley, J. A., Naveira Garabato, A.C., Waterman, S., Smeed, D. A. , Ledwell, J.R., Meredith, M.P. , St. Laurent, L., Thurnherr, A.M., Toole, J.M., Watson, A. J.: Rates and mechanisms of turbulent dissipation and mixing in the Southern Ocean: Results from the Diapycnal and Isopycnal Mixing Experiment in the Southern Ocean (DIMES), J. Geophys. Res. Oceans, 118, 2774–2792, https://doi.org/10.1002/jgrc.20217, 2013.

Simpson, J. H., and Sharples, J.: Introduction to the physical and biological oceanography of shelf seas, Cambridge University Press, pp. 1-24, https://doi.org/10.1038/250404a0, 2012.

Silva, J. D., Buijsman, M. C., and Magalhaes, J.: Internal waves on the upstream side of a large sill of the Mascarene Ridge: a comprehensive view of their generation mechanisms and evolution, Deep Sea Research Part I: Oceanographic Research Papers, 99, 87-104, https://doi.org/10.1016/j.dsr.2015.01.002, 2015.

Solano, M. S., Buijsman, M. C., Shriver, J. F., Magalhaes, J., da Silva, J., Jackson, C., Arbic, B. K., and Barkan, R.: Nonlinear internal tidesin a realistically forced global oceansimulation, Journal of GeophysicalResearch: Oceans, 128, https://doi.org/10.1029/2023JC019913, 2023.

Sprintall, J., Gordon, A. L., Koch-Larrouy, A., Lee, T., Potemra,J. T., Pujiana, K., and Wijffels, S.: The Indonesian Seas and their impact on the Coupled Ocean Climate System, Nat. Geosci., 7, 487–492, https://doi.org/10.1038/NGEO2188, 2014.

Stansfield, K., Garrett, C., Dewey, R.: The probability distribution of the Thorpe displacement within overturns in Juan de Fuca Strait, J. Phys. Oceanogr, 31, 3421–3434, https://doi.org/10.1175/1520-0485(2001)031<3421:TPDOTT>2.0.CO;2, 2001.

St. Laurent, L. C., Garabato, A.N., Ledwell, J.R., Thurnherr, A.M., Toole, J.M., and Watson, A. J.: Turbulence and diapycnal mixing in Drake Passage, Journal of Physical Oceanography, 42, 2143-2152, https://doi.org/10.1175/JPO-D-12-027.1, 2012.

Sutherland, G., Reverdin, G., Marié, L., and Ward, B.: Mixed and mixing layer depths in the ocean surface boundary layer under conditions of diurnal stratification, Geophys. Res. Lett, 41, 8469–8476, https://doi.org/10.1002/2014GL061939, 2014.

Takahashi, A., and Hibiya, T.: Assessment of finescale parameterizations of deep ocean mixing in the presence of geostrophic current shear: Results of microstructure measurements in the Antarctic Circumpolar Current region, Journal of Geophysical Research: Oceans, 124, 135–153, https://doi.org/10.1029/2018JC014030, 2019.

Tchilibou, M., Koch-Larrouy, A., Barbot, S., Lyard, F., Morel, Y., Jouanno, J., and Morrow, R.: Internal tides off the Amazon shelf during two contrasted seasons: Interactions with background circulation and SSH imprints, Ocean Science Discussions, 14, 1283–1301, https://doi.org/10.5194/os-18-1591-2022, 2022.

Thorpe S. A.: Turbulence in the ocean pycnocline. In: An Introduction to Ocean Turbulence, Cambridge University Press, 116-157, 2007.

Thorpe, S. A.: Models of energy loss from internal waves breaking in the ocean, Journal of Fluid Mechanics, 836, 72–116, https://doi.org/10.1017/jfm.2017.780, 2018.

Varona, H. L., Veleda, D., Silva, M., Cintra, M., and Araujo, M.: Amazon River plume influence on Western Tropical Atlantic dynamic variability, Dynamics of Atmospheres and Oceans, 85, pp.1-15, https://doi.org/10.1016/j.dynatmoce.2018.10.002, 2018.

Wang, Y.-H., Dai, C.-F., and Chen, Y.-Y.: Physical and ecological processes of internal waves on an isolated reef ecosystem in the South China Sea, Geophysical Research Letters, 34(18), https://doi.org/10.1029/2007gl030658, 2007.

Whalen, C. B., Talley, L. D., and MacKinnon, J. A.: Spatial and temporal variability of global ocean mixing inferred from Argo profiles, Geophys. Res. Lett, 39:L18612, https://doi.org/10.1029/2012GL053196, 2012.

Xie, X. H., Cuypers, Y., Bouruet-Aubertot, P., Ferron, B., Pichon, A., Lourenço, A., and Cortes, N.: Large-amplitude internal tides, solitary waves, and turbulence in the central Bay of Biscay, Geophysical Research Letters, 40(11), 2748–2754, https://doi.org/10.1002/grl.50533, 2013.

Xu, P., Yang, W., Zhu, B., Wei, H., Zhao, L., and Nie, H.: Turbulent mixing and vertical nitrate flux induced by the semidiurnal internal tides in the southern Yellow Sea, Continental Shelf Research, 208, 104240, https://doi.org/10.1016/j.csr.2020.104240, 2020.

Yang, W., Wei, H., Zhao, L., and Zhang, J.: Turbulence and vertical nitrate flux adjacent to the Changjiang Estuary during fall, Journal of Marine Systems, 212: 103427, https://doi.org/10.1016/j.jmarsys.2020.103427, 2020.

Zaron, E. D., Capuano, T. A., and Koch-Larrouy, A.: Fortnightly variability of Chl a in the Indonesian seas, Ocean Sci., 19, 43–55, https://doi.org/10.5194/os-19-43-2023, 2023.

Zhao, Z., Alford, M. H., Girton, J. B., Rainville, L., and Simmons, H. L.: Global Observations of Open-Ocean Mode-1 M2 Internal Tides, J. Phys. Oceanogr., 46, 1657–1684, https://doi.org/10.1175/JPO-D-15-0105.1, 2016

Zhao, Z., Alford, M. H., and Girton, J.B.: Mapping low-mode internal tides from multisatellite altimetry, Oceanography, 776 25(2):42–51,https://doi.org/10.5670/oceanog.2012.40, 2012.